Dissertation

submitted to the

Combined Faculty of Mathematics, Engineering and Natural Sciences

of Heidelberg University, Germany

for the degree of

Doctor of Natural Sciences

Put forward by

Nils-Holger Rehbehn

born in: Kiel, Germany

Oral examination: 22.11.2023

Measurement of highly charged Ca and Xe ions and their sensitivity to a hypothetical fifth force beyond the Standard Model

Referees: Prof. Dr. José R. Crespo López-Urrutia
PD Dr. Wolfgang Quint

Measurement of highly charged Ca and Xe ions and their sensitivity to a hypothetical fifth force beyond the Standard Model

It is evident that the current Standard Model of particle physics fails to decode the enigma of dark matter. Amongst dark matter candidates, a promising contender is a hypothetical fifth-force coupling between atom constituents, which is key to establishing a New Physics (NP) model. To prove its existence, isotope shifts are investigated with the King plot method to detect its coupling effect between neutrons and electrons in an atom. Although this effect is weak, it may be resolved with quantum logic spectroscopy of highly charged ions, which offers high precision measurements of isotope shifts, but this method requires ground-state transitions.

In this thesis, I measured ground-state transitions in isotope-rich elements, Ca and Xe, using an electron beam ion trap. Furthermore, I theoretically investigated these transitions in their sensitivity to a hypothetical fifth-force, using the generalized King plot method. My results predicted an improvement of sensitivity by at least four orders of magnitude, compared to previous King plot analyses. This sensitivity would constrain the NP parameter space more stringently than prior imposed restrictions.

This work lays the theoretical foundation of searching for a fifth force and, ultimately, validating an NP model better suited to decipher our universe's mysteries.

Messung von hochgeladenen Ca- und Xe-Ionen und ihre Empfindlichkeit auf eine hypothetische fünfte Kraft jenseits des Standardmodells

Es ist offensichtlich, dass das derzeitige Standardmodell der Teilchenphysik nicht in der Lage ist, das Rätsel der Dunklen Materie zu lösen. Ein vielversprechender Kandidat unter den Kandidaten für die dunkle Materie ist eine hypothetische Kopplung der fünften Kraft zwischen den Bestandteilen des Atoms, die der Schlüssel zum Aufbau eines Neuen-Physik-Modells (NP) ist. Um ihre Existenz zu beweisen, werden Isotopenverschiebungen mit der King-Plot-Methode untersucht, um ihren Kopplungseffekt zwischen Neutronen und Elektronen in einem Atom nachzuweisen. Obwohl dieser Effekt schwach ist, könnte er durch Quantenlogik-Spektroskopie an hochgeladenen Ionen aufgelöst werden, was hochpräzise Messungen von Isotopenverschiebungen ermöglicht, jedoch erfordert diese Methode Grundzustandsübergänge.

In dieser Arbeit habe ich Grundzustandsübergänge in isotopenreichen Elementen, Ca und Xe, mit einer Elektronenstrahl-Ionenfalle gemessen. Darüber hinaus habe ich diese Übergänge theoretisch auf ihre Sensitivität gegenüber einer hypothetischen fünften Kraft mit Hilfe der verallgemeinerten King-Plot-Methode untersucht. Meine Ergebnisse sagten eine Verbesserung der Sensitivität um mindestens vier Größenordnungen im Vergleich zu früheren King-Plot-Analysen voraus. Diese Sensitivität würde den NP-Parameterraum strenger einschränken als die bisherigen Einschränkungen.

Diese Arbeit legt die theoretische Grundlage für die Suche nach einer fünften Kraft und letztendlich für die Validierung eines NP-Modells, das besser in der Lage ist, die Geheimnisse unseres Universums zu entschlüsseln.

Contents

Acronyms

CRM collision radiative modelling

DM dark matter

EBIT electron beam ion trap

EUV extreme ultraviolet

FS field shift

GKP generalized King plot

HCI Highly charged ions

HD-EBIT Heidelberg-EBIT

IR infrared

IS isotope shift

KP King plot

LLPs long-lived particles

MS mass shift

NL non-linearity

NmGKP no-mass generalized King plot

NmKP no-mass King plot

NMS normal mass-shift

NP New Physics

ODR orthogonal distance regression

QED quantum electro dynamics

QFS quadratic field-shift

QLS quantum logic spectroscopy

QMS quadratic mass-shift

SI International System of Units

SM Standard Model of particle physics

SMS special mass-shift

TPC time projection chamber

UHV ultra-high-vacuum

ULDM Ultra-light dark matter

WIMP weakly-interacting massive particle

Chapter 1

Motivation

1.1 Standard model of particles physics

The universe is incredibly vast and contains everything ever to exist, ranging from subatomic particles to enormous structures formed by millions of galaxies. Revolutionized by Einstein, general relativity describes how heavy masses bend space-time and in return its effects onto other objects. Quantum physics, on the other end, describes smallest interactions of the smallest particles. Currently, the most successful model for the most elementary parts of the universe is the Standard Model of particle physics (SM) [1]. Its constituents are shown in Fig. 1.1. It has made correct predictions of particles, e.g. top quark [2] and tau-neutrino [3], before they were experimentally found, thus validating the theory. Finally, with the discovery of the Higgs-boson [4, 5, 6] this model has reached its completeness. While the Higgs-boson explains the mass of particles, the SM still fails to explain gravity on a quantum level, as gravitons remain purely theoretical. Moreover, there are several observed phenomena which cannot be explained by the SM alone.

An example of this is the rotational curve of galaxies [8], where the outer parts rotate faster than expected of them for their size. While some suggest that this is due to invisible masses in form of dark matter (DM) within galaxies, the reason remains unclear [9]. Another unsolved mystery is the existence of neutrino oscillations and their implied masses [10]. However, only upper limits, rather than absolute values, have been reported. It has also been suggested that neutrinos are their own antiparticles, which, if true, would lead to a lepton number violation [11, 12], which is forbidden in the SM. Furthermore, the SM cannot explain the vast disparity between matter and antimatter, which is known as baryon-asymmetry. Bertone and Hooper [13] offers a comprehensive review on the shortcomings of the SM.

It is evident that the SM alone is insufficient to explain the aforementioned phenomena. A New Physics (NP) model beyond the SM is thus needed to address

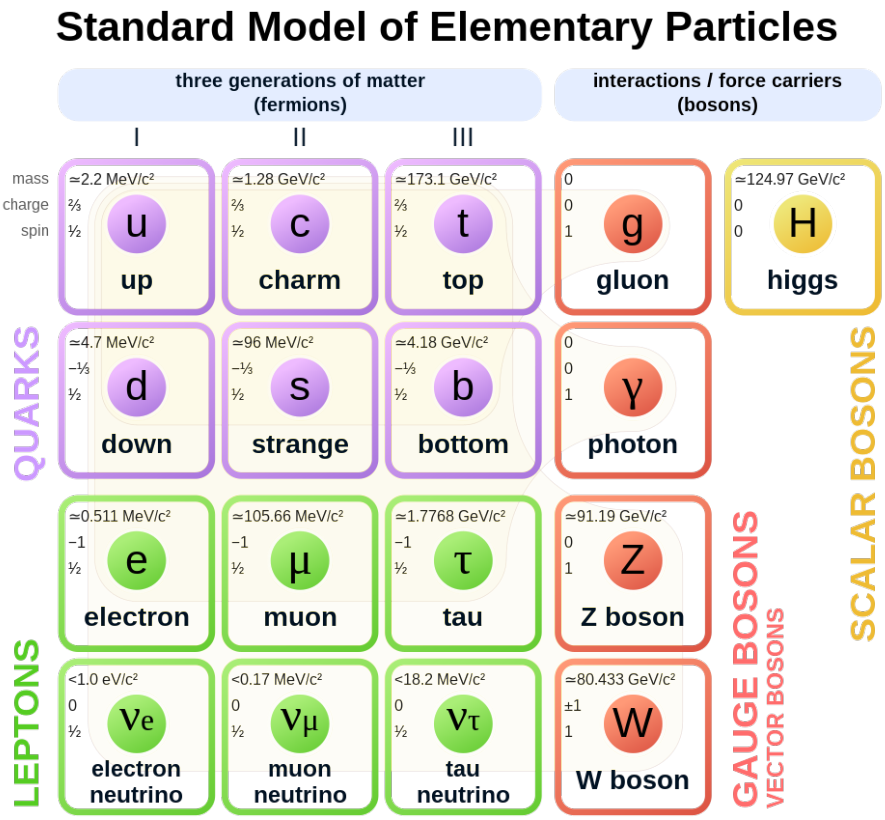

Figure 1.1: Standard Model of particle physics [7]. Different combinations of quarks describe leptons (three quarks) and bosons (quark-antiquark pair).

this, by either expanding the current theory, or providing SM constituents in its own predictions.

1.2 Search for a new physics model

DM is elusive and consists of a wide variety of potential candidates, as depicted in Fig. 1.2. To find DM, a wide selection of these candidates [14] need to be covered. Currently, there are numerous ongoing efforts to find distinct proof of a NP model.

One of the most prominent experiments, which also helped find the Higgs-boson [5, 6], is the ATLAS detector at the Large Hadron Collider (LHC) at CERN [15], where particles produced by proton-proton collisions are investigated. Until now, no exception to the SM were observed. However, a limitation of the experiment is the short measurement time, which overlooks long-lived particles (LLPs) predicted by multiple DM models [16]. Hence, efforts to employ new detectors are currently undergoing to include these LLPs by extending the duration of measurements.

The XENON1T experiment [17] and its successor XENONnT [18] focus on directly detecting interactions of weakly-interacting massive particle (WIMP) with liquid Xe. For this purpose, a time projection chamber (TPC) is filled with multiple tons of liquid Xe, which then allows the reconstruction of the origin of any freed electron. The setup also contains photo-multiplier tubes (PMTs) to detect faint light, which arise from de-excitation processes. This combination allows the identification of the event particle, e.g. a WIMP or simply a neutrino.

The Karlsruhe Tritium Neutrino (KATRIN) experiment [19] has been deployed to investigate neutrino masses. By measuring the minuscule shift in the energy spectrum of electrons in beta-decays, it infers the mass of the electron-antineutrino. The most recent measurement yielded an upper limit of an electron-neutrino mass of $m_\nu < 0.8\,\mathrm{eV}$ [20].

Neutrinoless double-beta decay [21] is investigated with e.g. the EXO-200 (Enriched Xenon Observatory 200) [22]. Similar to XENON1t, a smaller TPC tank is filled with liquid Xe, which is enriched with about 80% of the isotope ^{136}Xe, which has a half-life of about $2 \times 10^{21}\,\mathrm{yr}$ [23] until it decays via a double-beta decay. Using the TPC, as well as momentum and energy conservation, it can be inferred if a neutrino was involved in the decay or not. The current limit on the half-life for a possible neutrinoless double-beta decay has been found to be $T_{1/2} > 1.8 \times 10^{25}\,\mathrm{yr}$ [24].

Ultra-light dark matter (ULDM) candidates have potential effects on, e.g., a variation of the fine-structure constant α [25]. It was suggested that α changes either with time, locally, or both [26]. In either case, data obtained from distant quasars [27] seem to confirm it, however the statistical uncertainty is high. To overcome this limitation, optical atomic clocks are used to achieve best resolution by precisely measuring the energy ratio of two transitions with different dependencies on α, which would change accordingly. [28]

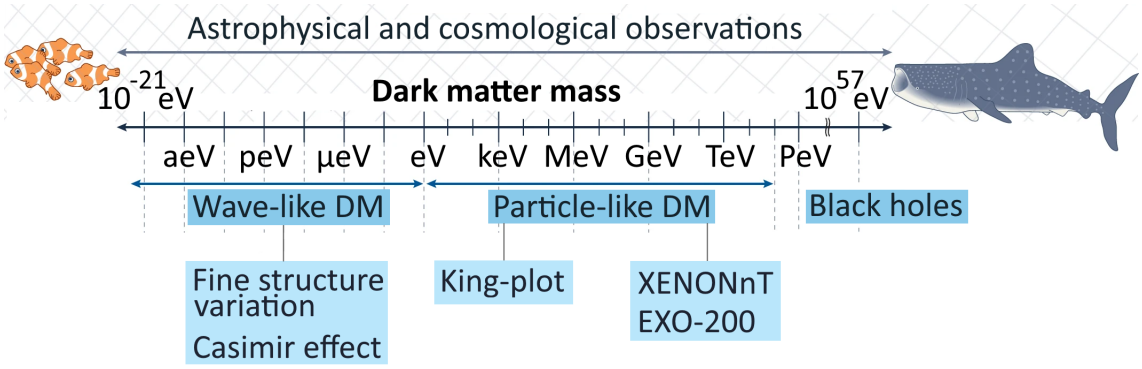

Figure 1.2: Mass range of potential DM candidates, scaling from ultralight to massive. As described in Ref. [14] (paraphrased): we are looking for a fish in the ocean, we only know that it is in the ocean, but we do not know its size, so we need to deploy all kinds of nets to have the best possible chance to catch it. Adapted from Ref. [14].

1.2.1 A fifth force

ULDM and WIMPs are intensively studied in the search for proof of a NP model to explain the effects of DM. In addition to these candidates, researchers have also probed the possibility of a small ranging force within atoms - a fifth force [29]. While there is no such proof of such a force yet, it might be able to explain the anomaly seen in ^{8}Be and ^{12}C. In these experiments, a nuclear excitation is resonantly produced, which decays by the release of a high energy-photon on rare occasions. Subsequently, this energy can also lead to the production of an electron-positron pair. An observation of their opening angle revealed an unexpected deviation, which may be attributed to a new boson of about 17 MeV, known as X17 [30, 31, 32]. A boson of this size could also explain the anomalous magnetic moment of the muon [33].

This fifth force is difficult to detect directly. In an atom, for example, its expected weak coupling could be easily overshadowed by other more prominent effects. Electron-proton interactions are dominated by the electromagnetic force, and neutron-proton interactions are dominated by the nuclear forces. This narrows it down to the possible interaction between electrons and neutrons, which would have no expected interaction on the atomic scale.

Isotopes are therefore ideal candidates to investigate this interaction, because they contain the same charged components, but vary in the number of neutrons. Comparing a transition in two isotopes could show a difference caused by the fifth force. However, the different number of neutrons also cause a shift due to a change in the physical properties of the nucleus. While the nuclear mass is fairly well-studied, other parameters and their influence on the electronic structure remain to be fully elucidated [34]. These influences can, in principle, be calculated theoretically, but even with the advances made in quantum electro dynamics (QED) and improved

numerical calculations, theoretical models still only hold accuracy of a few percentages in systems with more than a few electrons [35]. This uncertainty becomes greater with the complexity of the atom. The so-called King plot (KP) method [36] has recently reemerged as an appropriate approach to overcome this. Though its original purpose was to extract isotope shift (IS) parameters using graphical analysis, recent reevaluation has discovered its potential to find effects beyond the SM [37, 38, 39]. The rationale of using KP is based on the linearity of different isotope-pairs by shifts caused by the first-order SM. If a fifth force would be present, a deviation from this linearity should be detected. However, a limitation of the KP is that it only accounts for the first-order shifts of the SM. With higher measurement precision, more nuclear SM effects would become visible, which would also result in a deviation. Extending the KP into higher dimensions would allow compensation for these higher-order SM effects. This is known as a generalized King plot (GKP) [37, 39]. Each dimension requires another isotope-pair to remain a determined system, resulting in the need to perform these GKPs on elements with many available isotopes. The SM effects will be discussed in greater detail in chapter 2.3.4 and the GKP presented in chapter 2.3.5.

This method has gained a lot of interest over the last couple of years, with IS studies done in Ca [40], Yb [41, 42], Sr [43] and Cd [44]. However, no evidence for a fifth force has been found yet. This calls for more measurement precision, as well as transitions with higher sensitivity to a fifth force.

1.3 Highly charged ions

Highly charged ions (HCI) and plasmas are most prevalent in the universe yet rare on Earth. As such, research in this field is confined to specialized laboratory experiments or astrophysical observations, which heavily limits relevant data acquisition. This limitation can be especially observed in the NIST database [45] on the number of transition listed for each element and each charge state. The highest number of listed transitions are in neutral, singly or doubly charged states. This number drops rapidly with higher charge states, which results in mostly unknown systems named collectively as the *spectral desert*, as visualized in Fig 1.3. This decline can be attributed to the historical lack of widely available methods for measuring these systems. The first production of HCIs was done with electron beam ion sources (EBIS), but their setup was designed for accelerators. To study HCIs more closely, an electron beam ion trap (EBIT) was developed, which contained a central trap to perform in-EBIT spectroscopy [46, 47, 48]. The rising interest and availability of affordable EBITs, such as the Heidelberg Compact EBIT (HC EBIT) [49], will lead to an increased accumulation of transitions, thus mitigating the issue of the spectral

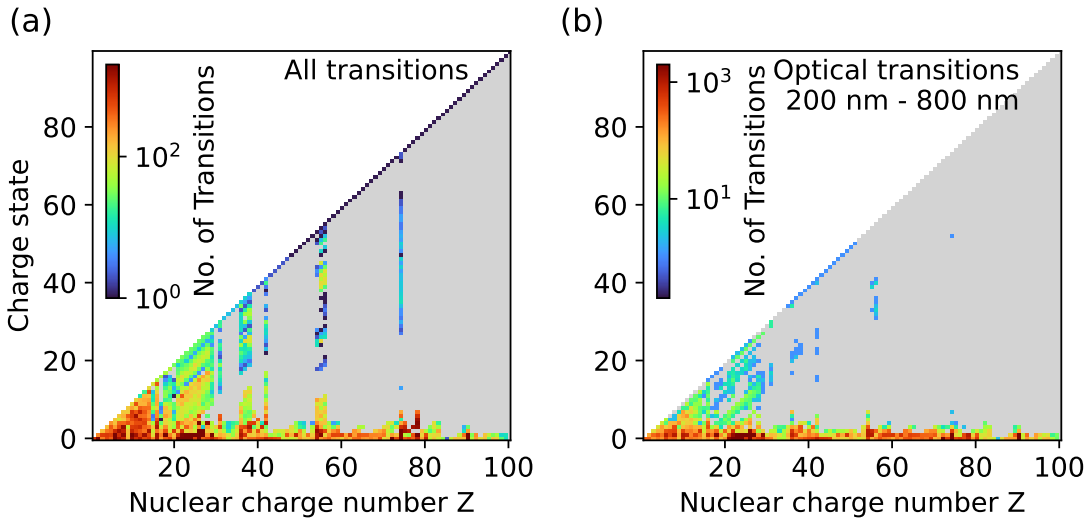

Figure 1.3: Spectral desert from NIST database [45] showing each element by their nuclear charge number Z and different charge states, where (a) pertains to for all entries in the database, and (b) pertains to optical transitions in the database.

desert. In addition to learning more about HCIs in general, other scientific fields can also benefit from this research.

Firstly, the development of fusion power generators can benefit from research in multiple disciplines, one of which being HCI research. Despite being highly funded, progress on fusion generators is slow, with its development currently spanning over six decades [50]. This is because of various interdisciplinary and unanticipated effects present in the reactors. The first ever energy gain with fusion was achieved at the end of 2022 with lasers at National Ignition Facility (NIF) [51], however, this setup was not designed as a power generator for commercial use, for which bigger designs will be needed instead. The biggest fusion generators are of the tokamak and the stellarator design. Here, plasma physics research forms the basis. While tokamaks are simple in design, plasma confinement and stability are an issue. These issues are countered in the stellarator design by employing specific, asymmetrical coils [52, 53]. This design, however, has a reduced plasma temperature needed for the fusion process. Another detrimental effect on the fusion plasmas are plasma-wall interactions, which release nano- and micrometer sized particles into the system. Research on these dusty plasmas is therefore highly relevant [54]. Furthermore, naturally present HCIs in plasmas can be used as a probe for internal parameters such as the ion and electron temperature, ion confinement, and plasma transport; as reviewed in Ref. [55]. Collectively, research in these fields may lead to clean energy development.

Secondly, the field of astrophysics also benefits from HCI research. A recent example is the Fe^{16+} 3C/3D ratio, which is used in X-Ray astronomy to acquire data

on the temperature of the astrophysical system. However, theory and experiment have been highly inconsistent with each other for decades, until a breakthrough was made in the method of in-lab measurements. In this breakthrough, the electron beam used to produce the HCIs was turned off repeatedly for the measurement. This approach avoided the effects of electron impact excitation, and thus led to consistent results on the ratio generated by photo excitation alone, which are the dominant cause in astrophysical systems [56].

Lastly, the field of metrology also benefits from data on HCIs. Atomic clocks form the frontline of metrology [57] and are increasingly precise. The most famous clock is the Cs-clock, which is used as the definition of the International System of Units (SI) second, shown as a level scheme in Fig. 1.4. This clock's precision is sufficient for GPS and other standard technologies, as it only loses one second every 300 million years. However, this clock transition is limited to about 10^{-16} fractional uncertainty, which reduces the precision of some scientific reports when converted to the SI second [58]. Higher precision can be achieved using current clocks in different elements [59, 60], which are able to reach a relative uncertainty on the order of 10^{-18}.

A new definition of the SI second is eventually required, for which the HCIs are of high relevance. The advantages of HCIs over neutral or singly charged ions are long known and confirmed [62, 48]. They have a greatly reduced susceptibility to external perturbations, which inhibit systematic shifts caused by the electric and magnetic fields of the trapping method as well as potential background radiation effects on the energy levels of the ion. Hence, this makes them ideal candidates to achieve highest precision. It is important to consider that most clocks fall within the optical spectrum because they take advantage of the higher frequency and stability of the optical transitions compared to microwave transitions, e.g. of the Cs-clock. However, exploration in this spectral range is particularly scarce, which results in an even larger spectral desert, as shown in Fig. 1.3 (b). Currently, relative precision up to 10^{-16} on HCI clocks [63, 64] was achieved with the quantum logic spectroscopy method, which will be discussed in more detail in the following chapter.

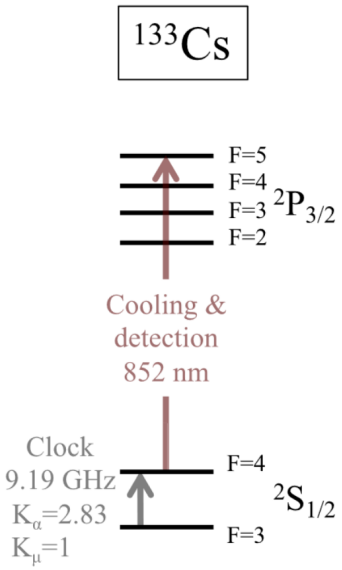

Figure 1.4: Cs-clock transitions. The narrow clock transition is between hyperfine levels of $2S_{1/2}$, and the cooling is performed via a faster transition. From Ref. [61].

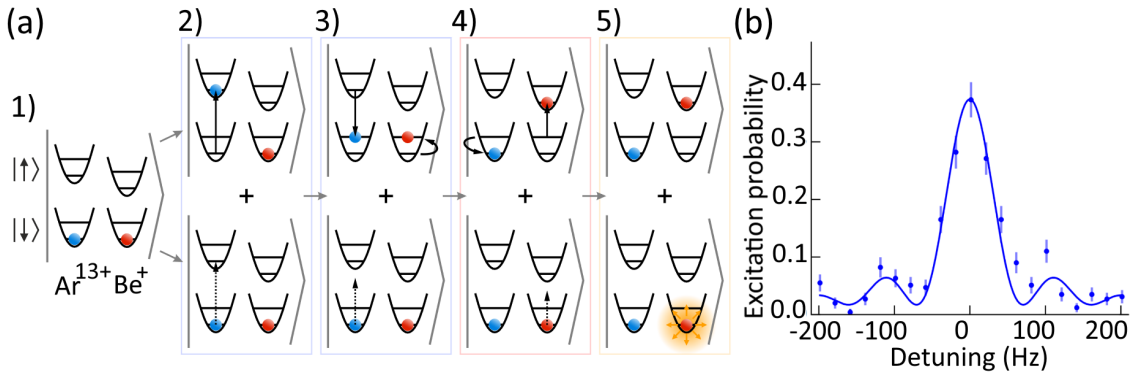

Figure 1.5: (a) Scheme of the QLS in an example of Ar^{13+}. Lines in the wells refer to motional modes, while the upper well refers to an excited, electronic level. Refer to text for detailed explanation. Taken from Ref. [68]. (b) Measurement of the excitation probability for different detuning of the probing-laser. From Ref. [63].

1.4 Quantum logic spectroscopy

Typical atomic clocks require two transitions, the narrow transition of interest and a faster transition that can be used to cool the ion down to a few milli-Kelvin. Both of them are shown in Fig. 1.4 for the Cs-clock. In HCIs, the choice of transitions within one ion becomes increasingly rare as the atomic level structure shifts to higher energies with the charge state. To overcome this lack of a cooling transition, the quantum logic spectroscopy (QLS) method [65, 66] contains a second trapped ion of known properties in the trap together with the ion of interest, called the spectroscopy ion. This second ion is known as the logic ion and is chosen based on the charge-mass ratio relative to the spectroscopy ion, and a structure which easily controls the system. Such ions can be e.g., Be^+ [63] or Mg^+ [60]. Due to their charges, both ions are electromagnetically coupled to each other, resulting in sympathetic cooling, where the motion control of the extra ion will be induced onto the spectroscopy ion. A difference in charge and mass between the logic and spectroscopy ion can make typical sympathetic cooling difficult for certain directions of motion. To overcome this, an algorithmic cooling method [67] was developed, with which any pairing of ions can be controlled, regardless of the charge to mass ratio between the two ions. The measurement procedure scheme of the QLS method is shown in Fig. 1.5 (a) [68]. From left to right: 1) the system is prepared. Both spectroscopy and logic ions are motionless in the trap and in the electric ground-state. 2) An adjustable laser probes the transition. The laser can be detuned in its frequency relative to the transition frequency, and the probability of electronic excitation varies depending on the offset. The top row of Fig. 1.5 (a) shows the case where the spectroscopy ion is electronically excited, while the bottom row shows the case where no excitation happens. 3) In the case of a successful excitation, a second laser pulse will then electronically de-excite the spectroscopy ion. This pulse is based on the energy of the adjustable, first laser

pulse, however, its energy is slightly reduced by the energy of a motional-mode (red-sideband pulse). This will give the two coupled ions an axial motion within the trap. If no excitation occurs in the first place, this red-sideband pulse would not change the system, as its reduced energy would be either too low to excite the ion electronically, or too high to affect the system in any motional way. 4) In the next step, another red-sideband pulse is applied to the known transition of the logic ion in order to stop the motion in the system again and excite the logic-ion. This, again, has no effect on the ground-state system, where no excitement of the spectroscopy ion has occurred before. 5) The final step is to use the Doppler cooling laser on the logic ion, which will only result in fluorescence from ground-state excitation. This light or no-light signal will then be observed and give the QLS method its *logic* part. These steps are then repeated multiple times to extract the excitation probability and from it the transition energy at the position of the highest probability. This is shown in Fig. 1.5 (b) [63]. The downside of this method is that it only works on ground-state transitions as the state has to be clearly defined, which is not the case if the electron can decay further in the energy level.

The QLS method has been used on Al^+ [66], proving the concept of this method, and more recently on Ar^{13+} [63, 64], highlighting a successful cooling and measurement of an HCI. Their uncertainty for the central position of the 441 nm transition was determined to be of 100 mHz. This is still limited by the 17 Hz natural linewidth of the transition. The uncertainty for a measuring time of τ is expected to be $10\,\mathrm{Hz}/\sqrt{\tau}$ [F1], which allows it to reach the 100 mHz uncertainty within a few hours of measurement. With its cooling and measurement method, the QLS method is of high interest for the search for DM with clocks, IS studies and KPs.

1.5 Elements and isotopes for King plot analysis

The number of isotopes play an important role in the KP method. Three isotopes are required for the principle KP in order to investigate a deviation from a conjunctional linearity. An increased number of isotopes leads to additional data points, which will not only improve the chance to observe a deviation, but also allowing the expansion of the KP into higher dimensions to compensate for higher-order SM contributions. However, hyperfine structure would further complicate the search for a fifth force, which is why only isotopes with an even number of neutrons and protons are eligible, as they do not have a nuclear spin and thus do not induce a hyperfine shift.

There are two ways to overcome higher-order SM contributions. The first is to utilize elements with a large number of stable, even isotopes and to span the GKP into the highest dimensions. The second option is to take elements with

weaker higher-order SM effects, which is typically the case in lighter elements. This effectively reduces the number of effects that need compensation.

1.5.1 Calcium

For light elements, calcium (Z = 20) is the best candidate, as it has five stable isotopes without nuclear spin. This isotope number with its fairly low mass number of 40 to 48 is unmatched by any other element.

Calcium was first isolated in 1808 and first observed as HCIs in the sun's corona. In modern technology it is mainly used as a seal in batteries and as plaster material. Its occurrence in bones and other organic materials makes it of high interest in biology. The ^{41}Ca isotope is also used to determine the dates of objects in the solar system with its half-life of 100 000 yr.

In nuclear physics, calcium is interesting due to its double-magic numbering of Z = 20, as well as N = 20 or N = 28 for the isotopes ^{40}Ca and ^{48}Ca, which results in a spherical nucleus [69]. Furthermore, ^{48}Ca isotope is of interest for the investigation the neutrinoless double-beta decay [70].

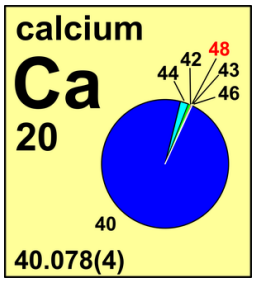

Figure 1.6: Overview of all the stable isotopes in calcium from Ref. [71].

Table 1.1: List of stable even isotopes in calcium with their abundances and masses from Ref. [72] and radii from Ref. [73].

A	Abundance	Mass (eV/c^2)	Radius (fm)
40	96.941(156)%	39.9625909(2)	3.4776(19)
42	0.647(23)%	41.958618(1)	3.5081(21)
44	2.086(110)%	43.955482(2)	3.5179(21)
46	0.004(3)%	45.95369(2)	3.4953(20)
48	0.187(21)%	47.9525229(6)	3.4771(20)

An overview of the stable calcium isotopes is shown in Fig. 1.6 and the ones without nuclear spin are listed in Tab. 1.1. Their abundances, masses and radii are included from Refs. [72, 73].

On one hand, relative mass uncertainties are at least on the order of $\mathcal{O}(10^{-7})$. On the other hand, the radii are the least known with relative uncertainties of $\mathcal{O}(10^{-4})$. While the masses can be precisely obtained by measuring the cyclotron frequency [74], the radius requires more involved methods. These typically include scattering experiments and IS measurements [75], which do not have a comparable precision. As the latter is a major part of this work, it will be discussed in detail in chapter 2.3.1.

1.5.2 Xenon

The elements with the most stable isotopes without nuclear spin are tin ($Z = 50$) and xenon ($Z = 54$), which both have seven. Xenon contains slightly more neutrons and thus is expected to be slightly more affected by a hypothetical fifth force than tin for similar transitions.

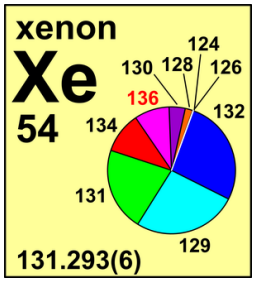

Figure 1.7: Overview of all the stable isotopes in xenon from Ref. [76].

Table 1.2: List of stable even isotopes in xenon with their abundances and masses from Ref. [72] and radii from Ref. [73].

A	Abundance	Mass (eV/c^2)	Radius (fm)
124	0.095(5)%	123.90589(1)	4.7661(55)
126	0.089(3)%	125.90430(3)	4.7722(52)
128	1.910(13)%	127.903531(7)	4.7774(50)
130	4.071(22)%	129.90350935(6)	4.7818(49)
132	26.909(55)%	131.90415509(4)	4.7859(48)
134	10.436(35)%	133.90539303(6)	4.7899(47)
136	8.857(72)%	135.90721448(5)	4.7964(47)

Xenon is one of the six naturally occurring noble gases. Discovered in 1898, it is the second rarest noble gas on earth and can be extracted from air. It is commonly used in the flash-bulb for photography, lamps in sunbeds, food processing and cars. As introduced in chapter 1.2, xenon is also very popular in the search for an NP model. Research interest is based on either its isotope ^{136}Xe in regards of its potential neutrinoless double-beta decay [22], or in the search of direct dark-matter particle interactions with liquid Xe [18], where its heavy mass increases the cross section and the chance of an interaction by its density.

All stable isotopes are depicted for their natural abundances in a pie-chart in Fig. 1.7 and the ones relevant for the KP method, i.e. without nuclear spin, are listed in Tab. 1.2.

1.6 Purpose of research

Observations unexplained by the SM push the agenda of an NP model. The properties of the constituents of such a model remain unknown, thus inspiring searches across a wide range of possible parameters. While ULDM and WIMP candidates are already extensively studied, the recently improved KP method allows us to probe for a hypothetical intra-atomic fifth force.

This defines the purpose of research of this work. To find proof of a model beyond the SM is imperative. IS studies and application of the KP method require highly

precise laser spectroscopy. To reduce statistical uncertainties, transitions in HCIs are sought after. The QLS method is favored to measure these transitions with high precision in the future. It uses a co-trapped logic ion to cool and measure the transition without the need of an in-ion cooling transition. As discussed, the drawback of this method is the need for ground-state transitions, which are typically unknown, as shown in Fig. 1.3.

An investigation for possible ground-state transitions in HCIs is imperative to perform the QLS. For this search, HCIs were produced in an EBIT and their fluorescence was measured with a spectrometer. Identifications were done by comparing the results with calculations. In preparation for these highly precise measurements, the found transitions were then analyzed theoretically in their IS with a hypothetical fifth force present. This was to determine the ideal combinations of isotopes and transition for the highest sensitivity to such a force. The findings of this research will establish a foundation for highly precise measurements and significantly constrain the current NP model parameter space.

Chapter 2

Theory

The analysis within this work relies heavily on the theory based on IS, the hypothetical fifth force, the KP method, as well as its multi-dimensional extension in the generalized KP method. These will be therefore introduced in greater detail. Other aspects of relevance, like the atom and its transitions, will be briefly introduced. The appropriate citations are provided for further reference.

2.1 Atomic structure

An electron in a potential formed by a proton-neutron nucleus takes on discrete energy levels. These energy levels can be described via the Schrödinger equation with a potential V

$$\hat{H}\Psi = \left(-\frac{\hbar^2}{2m}\nabla^2 + V\right)\Psi = E\Psi, \tag{2.1}$$

where $\hat{H}$ is the Hamilton and ∇ the Nabla operator. The first term of the Hamiltonian is the kinetic energy, with the reduced Planck constant $\hbar$ and the particles mass m. The electron wavefunction is Ψ and its resulting eigenvalue is the energy E. The results of that equation are the energy levels for a simple hydrogen-like atom with a reduced mass $m = m_\mathrm{e}m_\mathrm{A}/(m_\mathrm{e} + m_\mathrm{A})$ and a coulomb potential $V = -Ze^2/(4\pi\epsilon_0 r)$ with the nuclear charge Z. This gives

$$E_n = -\frac{mZ^2e^4}{8\epsilon_0^2h^2n^2} = -R\frac{Z^2}{n^2}, \tag{2.2}$$

with the elementary charge e, the vacuum permittivity ϵ_0, the Planck constant h and the principal quantum number n ranging from 1 to ∞ in whole numbers. The constant R is known as the Rydberg constant ($R = me^4/8\epsilon_0^2h^2$).

However, this description is insufficient as it neglects spin and relativistic effects. These terms are included in the Dirac equation, from which the fine structure is derived [77]

$$E_{\mathrm{FS}} = \alpha^2 \cdot \left(\frac{1}{j+1/2} - \frac{3}{4n} \right) \cdot E_n \frac{Z^2}{n}, \tag{2.3}$$

here the fine structure constant α is defined as

$$\alpha = \frac{e^2}{2\epsilon_0 hc}. \tag{2.4}$$

Discrepancies between this theory and measurements are mainly due to effects of virtual absorption and emission of photons by the bound electron itself, which causes a small change in energy due to this radiation field. This shift is part of the theory of quantum-electrodynamics (QED) [77]. If the nucleus also has a spin, hyperfine splitting occurs. This is the case for isotopes with odd mass numbers, i.e. an odd number of the sum of protons and neutrons in the nucleus.

The angular momentum for a single electron is $\vec{j} = \vec{l} + \vec{s}$, with $\vec{l}$ the orbital momentum and $\vec{s}$ the spin. For a complete system of multiple electrons, the total angular momenta describe the energy levels. These are typically written in LS-notation

$$^{2S+1}L_J, \tag{2.5}$$

where the total angular momentum is J, the total spin of the electrons is S, and the orbital angular momentum is L, the states of which are denoted as S, P, D, F for $L = 0, 1, 2, 3$ and so on. However, only light elements follow the LS-coupling and thus this notation. In heavier atoms, the levels begin to mix and thus are not strictly separated anymore. This is known as jj-level mixing.

The classical energy levels, as described Eq. 2.2 $E = R/n^2$, paved the way for a better understanding of the atom. One of these ways was to compute expectation values for transitions based on known transitions

$$(E_2 - E_1) = (E_2 - E_0) - (E_1 - E_0) \quad \Rightarrow \quad \frac{1}{\lambda_{2\to1}} = \frac{1}{\lambda_{2\to0}} - \frac{1}{\lambda_{1\to0}}. \tag{2.6}$$

This is known as the Rydberg-Ritz combination principle and holds true for level structures based on more complex theories than the principal quantum number. It is applied in the spectroscopy of extreme ultraviolet (EUV) transitions, where unobserved optical transitions are calculated. In optical spectroscopy, if all three of these transitions have been measured, the principle may help with the identification of lines.

Electronic transitions between energy levels in an atom not only carry the specific energy difference between those levels, but also must conserve angular momenta

Table 2.1: Rigorous selection rules for different types and poles of transitions [78]. E denotes an electric transition and M a magnetic one. Each higher pole has a reduced transition rate compared to the one before. ΔJ is the change in angular momentum and ΔP is the parity change.

Dipole (2^1)		Quadrupole (2^2)		Octupole (2^3)	
E1	M1	E2	M2	E3	M3
$\Delta J = 0, \pm 1$		$\Delta J = 0, \pm 1, \pm 2$		$\Delta J = 0, \pm 1, \pm 2, \pm 3$	
$\Delta P \neq 0$	$\Delta P = 0$		$\Delta P \neq 0$		$\Delta P = 0$

because the emitted photon has a spin of one. Such transitions can result from different kinds of dipoles, which are either magnetic or electric. These are then called M1 or E1 transitions, respectively. M1 transitions only happen between levels with the same parity and a total angular momentum change of $\Delta J = 0, \pm 1$, whereas $\Delta J = 0$ is only allowed when $J \neq 0$. E1 transitions are similar, but only happen between levels of different parity. A listing of the rigorous selection rules is in Tab. 2.1. Higher-order poles can also occur, which would allow a greater change of the total angular momentum ΔJ. Those higher transition orders are called quadrupole (E2, M2), octupole (E3, M3), etc. transitions. Although a higher-order transition can always account for a lower-order transition, the transition rate is slower for higher-orders, which will be addressed in chapter 2.1.2. Transitions are therefore named by their strongest allowed transition type.

2.1.1 Highly charged ions

The advantage of HCIs over neutral or singly charged atoms are numerous. A detailed summary can be found in e.g. Kozlov et al. [48]. Such effects scale differently with the nuclear charge Z for a hydrogen-like atom. For the scaling of multi-electron atoms, the dependence changes to $Z_{\text{eff.}} \approx Z - N_{\text{e}}$, with the number of shielding electrons N_e. For HCIs, the scaling is therefore proportional to the charge number $Q = Z_{\text{eff.}}$ [79]. As described in Tab. 2.2, the energy levels in HCIs shift to higher

Table 2.2: Scaling of effects with nuclear charge $Z = Z_{\text{eff.}}$ for HCIs [48]. Energy splitting increases while external effects are attenuated.

Effect	Scaling
energy levels	Z^2
fine structure splitting	Z^4
hyperfine splitting	Z^3
QED effects	Z^4
atomic size	Z^{-1}
polarizability	Z^{-4}

energies proportionally with the squared charge state. This shifts not only optical transitions into the EUV range, but also brings infrared (IR) transitions into the optical range. Consequently, classically forbidden transitions become visible due to an increased transition rate. HCIs expose the inner electron that are more tightly bound to the nucleus. This bond is much stronger than that in neutral atoms, and thus makes the system less susceptible for external perturbations exerted onto the observed electron. This effect is found in Tab. 2.2 as reduced polarizability effect. It is important to note that the HCIs also greatly reduce second-order Zeeman- and Stark-shifts [80]. The strong scaling of QED effects allows HCIs to be utilized to test the QED theory with increased precision. HCIs are also an ideal candidate for the search of an ULDM influence on the fine-structure constant α, because the splitting of the fine and hyperfine structure increases with the charge states, thus making a variation of α easier to observe.

2.1.2 Transition rate

The radiant power of a transition from level k to level i can be expressed as [81, 78]

$$\langle P \rangle = A_{ki} N_k \cdot h\nu, \tag{2.7}$$

where A_{ki} is the Einstein coefficient for the spontaneous decay with the frequency ν between these levels. The value N_k represents the number of atoms that have the valence electron in the upper state k. This number decreases with each decay to any potential state below k and increases with direct excitation to k or a decay from higher states n. A time dependence of the N_k value can be written as

$$\frac{\delta N_k}{\delta t} = -\sum_i N_k A_{ki} + \sum_n N_n A_{nk} + C, \tag{2.8}$$

where the C accounts for all other effects by electron impacts from the electron beam, including excitation, de-excitation, ionization, recombination, etc. These terms give rise to an average population of the k level $\overline{N_k}$. From this average and the radiant power Eq. 2.7, the intensity emitted per solid angle for an isotropical emission is

$$I = \frac{\overline{N_k} A_{ki} h\nu}{4\pi}. \tag{2.9}$$

For optical transitions, the power of the emitted radiation can be expressed by a classical electric dipole (Hertzian dipole) [82, 78]

$$\bar{P} = \frac{8\pi^3 \nu^4}{3\epsilon_0 c^3} \overline{p^2}. \tag{2.10}$$

Here, c is the speed of light, h the Planck constant and ϵ_0 the vacuum permittivity of a transition with frequency ν. The average electric dipole moment $\overline{p^2}$ can also be described by the expectation value of the dipole moment operator $\vec{p}$

$$\langle \vec{p} \rangle = \langle \Psi_k \,|\, q\vec{r} \,|\, \Psi_i \rangle = \overrightarrow{M_{ki}}. \tag{2.11}$$

By comparing the powers of Eq. 2.7 and Eq. 2.10, as well as replacing the electric dipole with the expectation value $\overline{p^2} = \frac{1}{2}(|M_{ki}| + |M_{ik}|)^2 = \frac{1}{2}(2|M_{ki}|)^2$ [83], the rate for the spontaneous emission A_{ki} can be expressed for one emitting atom as [78, 84]

$$A_{ki} = \frac{16\pi^3\nu^3}{3\epsilon_0 h c^3}|M_{ki}|^2. \tag{2.12}$$

Because A_{ki} depends on ν^3 between two energy levels, the energy difference of the transition strongly influences its probability. This makes transitions with the same dipole moment in the EUV more likely than an IR transition.

Calculating $|M_{ki}|^2$ is typically performed with computational codes such as AMBIT [85] or flexible atomic code (FAC) [86]. This value is also called the line strength S [81]. While the line strength S has the advantage of being independent of the transition wavelength, the rate A_{ki} is a better choice for judging the actual visibility of the transition due to its proportionality to the intensity (Eq. 2.9). The line strength S is often expressed in atomic units of $e\,a_0$ for the electric dipole moment. To convert the atomic units to SI units, this factor will be included for E1 transitions [81]

$$A_{ki,\mathrm{E1}} = \frac{16\pi^3}{3h\epsilon_0\lambda^3} \cdot \frac{S_{\mathrm{E1}} \cdot (ea_0)^2}{g_d}. \tag{2.13}$$

To account for the degeneracy of the upper state, the line strength is divided by $g_d = 2J_{\mathrm{inital}} + 1$. If this degeneracy g_d remains, then the transition will be reported as gA_{ki}.

Other types of transitions follow similarly with their own transition moments. For an electric quadrupole (E2) this results in

$$A_{ki,\mathrm{E2}} = \frac{8\pi^5}{5h\epsilon_0\lambda^5} \cdot \frac{S_{\mathrm{E2}} \cdot (ea_0^2)^2}{g_d}. \tag{2.14}$$

Here, the wavelength dependence changes from λ^{-3} for E1 to λ^{-5}. The electric dipole moment is changed to the electric quadrupole moment ea_0^2.

For forbidden transitions, like the magnetic dipole (M1), a similar result is obtained

$$A_{ki,\mathrm{M1}} = \frac{16\pi^3\mu_0}{3h\lambda^3} \cdot \frac{S_{\mathrm{M1}} \cdot (\hbar e/m_{\mathrm{e}})^2}{g_d}. \tag{2.15}$$

While it is similar to $E1$, there are distinct differences, like the vacuum permeability μ_0, and the magnetic dipole moment $\hbar e/m_e$. The differences between the rates can be observed from Eq. 2.13 and Eq. 2.15. For a transition of same strength and wavelength, the M1 transition is a factor $\mu_0(\hbar e/m_e)^2/(\epsilon_0^{-1}(ea_0)^2) \approx 5\times10^{-5}$ less likely than an E1 counterpart, which is why M1 transitions are called forbidden. Hence, M1 transitions are only visible in the lowest lying electron configuration, where the parity is unchanged and no faster E1 transitions are allowed. In neutral atoms, only IR transitions can occur in such lowest configuration due the closeness of its levels. This further decreases their transition rate, as the wavelength dependence is λ^{-3}. In HCIs, however, these are shifted from IR, with rates of less than one transition per second, to the optical range, with rates of hundreds of transitions per second.

2.1.3 Line broadening

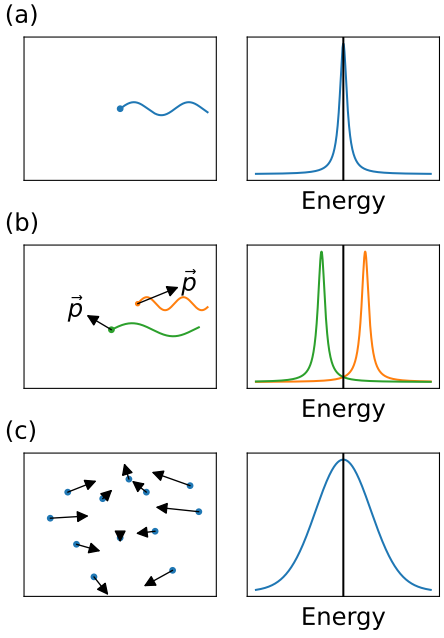

Figure 2.1: Scheme of line broadening. (a) Natural linewidth as Lorentzian. (b) Particle emitting light while moving toward (orange) and away from (green) the observer. (c) Average over all particles moving in random directions giving the line shape a Voigt profile. Adapted from Ref. [87].

Transitions between two levels are broadened by their own natural linewidth, which has a Lorentzian line shape [77]. Its width is a result of decay of the oscillating dipole, i.e. the lifetime of the upper level of the transition. A shorter lifetime results in a broader line and vice versa due to the uncertainty principle, which is expressed by [78]

$$\Delta E \Delta t \geq \hbar. \tag{2.16}$$

The lifetime Δt can be also written as the rate $\Delta t = 1/A_{ki}$, which leads to a frequency uncertainty of $\Delta\nu \geq A_{ki}/2\pi$.

An emitted photon is shifted in its energy when coming from a moving atom due to the Doppler shift with $E = p_x^2/2m$, where p_x is momentum towards the detector. Multiple atoms collectively cause a Gaussian line shape, which additionally broadens the linewidth. The resulting convolution of a Lorentzian and a Gaussian distribution is known as a Voigt distribution. This scheme is depicted in Fig. 2.1. The central part of the energy distribution is dominated by the Gaussian function, however, the Lorentzian line shape will become dominant towards the outside.

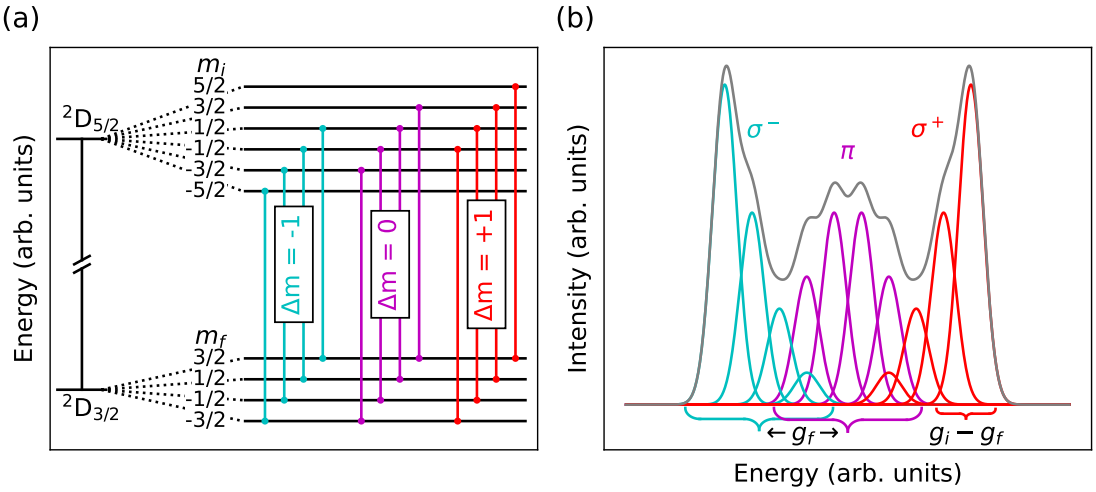

Figure 2.2: Scheme of Zeeman splitting based on $^2D_{5/2} - ^2D_{3/2}$ transition in Xe^{17+}. (a) Splitting of the energy levels by their total angular momenta J. Allowed transitions are indicated by $\Delta m = 0, \pm 1$. (b) Spectral line based on Zeeman splitting, where the energy splitting is a direct cause of the g-factors involved. Amplitudes of π and σ based on Clebsch-Gordan coefficients.

2.1.4 Zeeman effect

Caused by a magnetic field interacting with the electrons of an atom, the Zeeman effect splits the energy levels into three groups of $2J + 1$ components, where J is the lesser value of the two levels. This is schematically shown in Fig. 2.2 (a). This effect can be written as

$$\Delta E = \mu_B B g_J m_J. \tag{2.17}$$

Here, $\mu_B = \frac{1}{2} e\hbar / m_e$ is the Bohr magneton, g_J is the gyromagnetic factor and m_J the z-component of the total angular momentum of the level.

A transition between these split energy levels can be written as

$$\Delta(h\nu) = \mu_B B \cdot (g_i \cdot m_i - g_f \cdot m_f), \tag{2.18}$$

where the subscript J was omitted and instead contains i for the initial, upper level and f for the final, lower level. A transition between them is only allowed if $\Delta m = m_i - m_f = 0, \pm 1$ and are commonly denoted as π and $\sigma_\pm$ groups. The polarization of these groups are linear when observed perpendicular to the applied magnetic field. For M1 transitions the $\sigma_\pm$ lines are perpendicular- and the π lines parallel-polarized, relative to the applied magnetic field. The opposite is the case for E1 transitions [84].

The polarization also influences the effectiveness of the reflection of mirrors and gratings. For mirrors, the reflectivity of polarized light is represented for s-

and p-polarized light, where s is perpendicular to the plane of incidence and p is parallel to it. This concept is depicted in Fig. 2.3. Here, a mirror reflects a beam of light shown as a red arrow. This arrow spans the transparent red incidence plane. Polarization within or extruding from this incidence plane is called p-polarized light and s-polarized light, respectively.

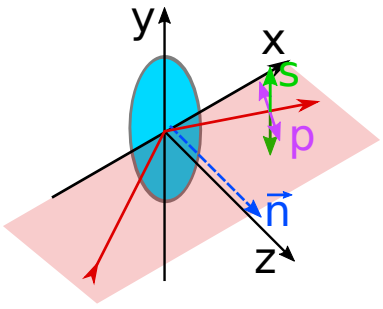

Figure 2.3: Definition of s- and p-polarization depending on the plane of incident (red). The normal of the mirror is $\vec{n}$.

Typically, mirrors reflect s-polarized light slightly better than p-polarized light at 45° reflective angles in the optical range [88]. This difference in reflection results in a difference in intensity for the π- and σ-components.

The g-factors play a role in the splitting of the Zeeman components. g_f is the main factor for the group separation between the π and σ groups, while the difference $g_f - g_i$ causes the peak separation within the groups. This can be understood by examining the $\sigma^{\pm}$ case of Eq. 2.18, where $m_f = m_i \pm 1$ and the splitting is expressed as $\Delta(h\nu) = \mu_B B(m_i(g_i - g_f) \pm g_f)$. Because $g_i - g_f$ is smaller than g_f, it directly causes smaller structures with m_i, while g_f causes the larger change between π and σ.

The g-factors of an electronic level can be approximated by the Dirac formula

$$g = 1 + \frac{J(J+1) + S(S+1) - L(L+1)}{2J(J+1)}, \tag{2.19}$$

which is based on the LS-coupling. Due to its simplicity, it does not account for the QED correction nor for strong level mixing. Better results can be computed with programs like AMBIT [85], which will be further introduced in the coming chapter 2.6.

The relative amplitude of the Zeeman components within each group of Δm can be calculated using Clebsch-Gordan (CG) coefficients, which stems from the Wigner-Eckart theorem [89]. These coefficients yield the probability of two total angular momenta j_1 and j_2 resulting in a new momentum j_3. Each has their z-axis projection $m_{1,2,3}$. A common notation of this is the Wigner 3-j symbol

$$\begin{pmatrix} j_1 & j_2 & j_3 \\ m_1 & m_2 & m_3 \end{pmatrix} = \begin{pmatrix} J_i & 1 & J_f \\ m & \Delta m & m + \Delta m \end{pmatrix} \quad \Rightarrow \quad \mathrm{CG}(J_i, J_f, m, \Delta m), \tag{2.20}$$

from which the CG coefficients can be calculated. A detailed way for calculating these, as well as different representations, can be found in Ref. [89]. The initial level is described by $j_1 = J_i$ and its projection $m_1 = m \in [-m_i, -m_i + 1, ..., m_i - 1, m_i]$. It is then investigated in its relation to a transition with $j_2 = 1$ and $m_2 = \Delta m$. The

final entry is the lower state of $j_3 = J_f$ and $m_3 = m + \Delta m$. The π and σ groups are represented by Δm, which is either 0 or ±1. The resulting CG coefficients can be seen in the amplitude of the different components within the π and $\sigma^{\pm}$ groups in Fig. 2.2 (b).

2.2 The fifth force as dark matter candidate

As introduced in chapter 1.2, there are numerous experiments searching for potential candidates for DM, but no proof has been found yet. In this work, the main focus is a hypothetical fifth force in the mass ranges from a few eV/c^2 to a few MeV/c^2. This range is within the electronic wavefunctions of an atom and would inflict small shifts in the energy levels. In general, such a force could couple to any particle in the atom, but a force coupling between neutrons and electrons would have the best chance of detection, as there are no other direct interactions expected in this range due to the charge neutrality of the neutron.

A general description of such a hypothetical fifth force interacting within an atom is a Yukawa potential

$$V_\Phi(r) = y_e y_n N \frac{\hbar c}{4\pi r} \exp\left(-\frac{c}{\hbar} \cdot m_\Phi \cdot r\right), \tag{2.21}$$

where the force strength is scaled by the coupling parameter $y_e y_n$ between electrons and neutrons via this force, as well as the number of neutrons $N = A - Z$ in the nucleus, which increase the number of partners the electron can couple to. The range of the force is scaled by the mass parameter m_Φ in the exponential function which causes a reduction in the range, if the mass parameter m_Φ is large, while a light mass means a longer range. The radial component is r and the constants are the reduced Planck constant $\hbar$ and the speed of light c.

DM below 1 eV/c^2 with a similar coupling could cause a similar effect on the electronic energy levels as it would have a reach beyond the atom, however, such a comparably long range is already excluded by studies of the Casimir effect. In these experiments, two plates are brought close to each other and the force exerted on them is measured. This limits the force range λ_Φ to be shorter than $\lambda_\Phi < 3$ nm ($m_\Phi > 65$ eV/c^2) at coupling strengths $y_e y_n > 8.6 \times 10^{-13}$ [90]. These excluded NP parameters are shown in Fig. 2.4 as a red-shaded area.

Investigations of scattering experiments, e.g. electron-neutron scattering [91], can also be used as probes for an intra-atomic force. These results already propose limits onto the NP parameter space. Most of the parameter space has been excluded by two kinds of experiments. The first experiment is on the magnetic moment $(g\text{-}2)_e$ of the electron, from which the fine-structure constant can be extracted [92], which

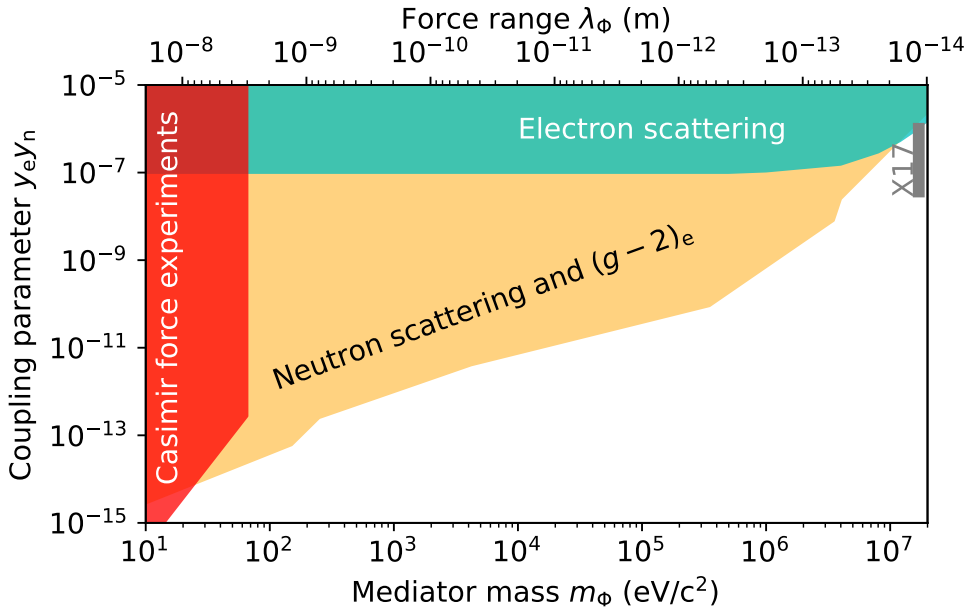

Figure 2.4: Overview of the excluded Yukawa-type fifth force parameter space by Casimir effect studies [90], electron scattering [91] and neutron scattering [94, 95, 96, 97] with electron magnetic moment $(g-2)_e$ [93, 92]. The potential X17 boson is given a gray marking [30, 31].

in turn yields a constraint on the coupling between electrons and a hypothetical boson [93]. The second experiment is on neutron scattering [94, 95, 96, 97], which restrains the coupling of the neutrons to such an NP boson. Multiplying both of these couplings results in an effective coupling constraint between neutrons and electrons to a hypothetical Yukawa-type boson. The NP parameters excluded by these scattering experiments are shown in Fig. 2.4 as green and yellow shaded areas.

The Be anomaly (X17), as introduction in chapter 1.2.1, lies at $m_\Phi = 17\,\mathrm{MeV}$ with interaction strengths between electrons and neutrons of $1.0 \times 10^{-6} \geq y_e y_n \geq 3.7 \times 10^{-8}$ [30, 31]. In Fig. 2.4, it is marked by a grey line. The white space in Fig. 2.4 is not constricted by any past experiment and may thus contain a fifth force boson.

2.3 Isotope shift and King plot

2.3.1 Isotope shift

As introduced in chapter 2.1, the electronic energy levels of an atom are mainly set by the Coulomb potential. These levels are not solely dependent on the nuclear

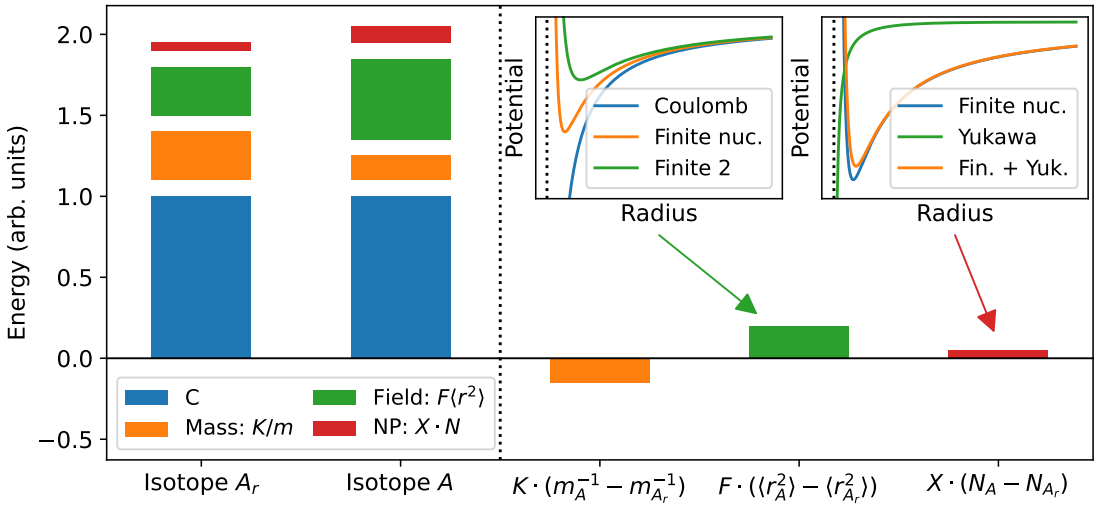

Figure 2.5: Scheme of a transition (left) and its IS (right) between two isotopes. C is the non-nucleus dependent part of the transition, K describes the mass shift, F the field shift, and X the hypothetical fifth force effects. Insets depict the change of the potential for a finite nucleus and an additional Yukawa potential. Note: not to scale.

charge, but also the finite size and the mass of the nucleus. A transition between two levels can be simplified to

$$\nu = C + K\frac{1}{m} + F\langle r^2\rangle + X \cdot N. \tag{2.22}$$

Here, C contains the nuclear-independent terms of the transition, consisting mainly of the coulomb-potential. The terms related to the mass m are represented by K, and the terms related to the finite nuclear size terms by the root mean square radius $\langle r^2\rangle$, which is represented by F. A fifth force parameter X would scale with the number of neutrons N in the nucleus. A schematic depiction of two isotopes can be seen on the left side in Fig. 2.5 with an exaggerated composition of the four energy terms. The IS, which is the change in energy between two isotopes, is shown on the right side of the figure, separated for the three changing terms. The non-nucleus dependent part C cancels out between the two isotopes. The remaining terms are mass shift (MS) and field shift (FS). MS is caused by the variation in the isotope masses, which affects the kinetic energy of the electrons. FS is caused by the different sizes of the nuclei and therefore its charge distribution within the nucleus. This changes the shape of the potential, which is depicted in Fig. 2.5 in an inset figure. Both of these effects change the energy of the electronic levels and thus their transitions. Note that the MS K is sometimes separated into the normal mass-shift (NMS) and special mass-shift (SMS), which are handled differently mathematically. The NMS is simply the change in the Bohr radius with the changed reduced mass, which can be handled analytically. Correlation terms between the momenta of the electrons are considered

in the SMS and are handled as a perturbation to the system, i.e. perturbation theory. However, both are part of the same MS K coefficient. [98, 99]

Mathematically, the IS $\delta\nu_i^a = \nu_i^A - \nu_i^{A_r}$ of an isotope-pair $a = (A, A_r)$ and the transition i can be written in the first-order SM as

$$\mathrm{IS}_{\mathrm{SM}} = \delta\nu_i^a = K_i\mu_a + F_i\delta\langle r_a^2\rangle. \tag{2.23}$$

The mass parameter $\mu_a = 1/m_A - 1/m_{A_r}$ is the difference of the inverse isotope masses and the radial parameter $\delta\langle r_a^2\rangle = \langle r_A^2\rangle - \langle r_{A_r}^2\rangle$ is the difference of the mean square nuclear charge radii.

A hypothetical fifth force described by a Yukawa-potential, as introduced in chapter 2.2, can be generally expressed as

$$\mathrm{IS}_{\mathrm{NP}} = y_{\mathrm{e}}y_{\mathrm{n}}X_i(m_\Phi)\gamma_a, \tag{2.24}$$

where the coupling to electrons and neutrons $y_{\mathrm{e}}y_{\mathrm{n}}$ scales the force strength and thus the shift strength. The dependence on the neutron number is set as $\gamma_a = N - N_r$ between the two isotopes. Finally, X_i is the electronic constant for the transition, which is a direct consequence of the Yukawa potential. It depends on the mass of the mediator boson m_Φ, which scales the force range. The effect of the Yukawa potential on the atomic potential is shown in Fig. 2.5 as inset. Compared to the Coulomb potential, the fifth force Yukawa potential has a minute and limited effect. The more the electronic wavefunction overlaps with the Yukawa potential, the greater the effect of the fifth force on the energy levels, thus improving the chance of detection.

2.3.2 Classical King plot

In the IS Eq. 2.23 the uncertainty of the nuclear radii are considerably greater than that of the nuclear masses, as seen in Tabs. 1.1 and 1.2. This would pose a stringent limitation on the sensitivity to a fifth force. To overcome this, the radius can be replaced with a second IS measurement. To perform this substitution, the IS is divided by the mass parameter μ_a, giving a *modified IS* $\mathrm{m}\delta\nu$ which is denoted with m. This results in an expression dependent only on a single isotope parameter $\delta\langle r_a^2\rangle/\mu_a$, which changes the IS Eq. 2.23 to

$$\frac{\delta\nu_i^a}{\mu_a} \equiv \mathrm{m}\delta\nu_i^a = K_i + F_i\frac{\delta\langle r_a^2\rangle}{\mu_a}. \tag{2.25}$$

This joined isotope-pair parameter can then be substituted by a second modified transition, resulting in a term which expresses these two transitions as

$$\mathrm{m}\delta\nu_1^a = \frac{F_1}{F_2}\mathrm{m}\delta\nu_2^a + \left(K_1 - \frac{F_1}{F_2}K_2\right). \tag{2.26}$$

This approach was first introduced by King [36], where Eq. 2.26 describes a linear relationship between the two modified transitions, known as the King-linearity. This equation can be solved by IS measurements of at least two isotope-pairs, which yields information about the FS and MS electronic constants F_i and K_i, respectively. The beauty of this method is that no calculations of these electronic coefficients are required.

If a fifth force causes an additional shift (Eq. 2.24) in these isotopes, the total IS changes to

$$\mathrm{IS} = \mathrm{IS}_{\mathrm{SM}} + \mathrm{IS}_{\mathrm{NP}} \;\equiv\; \delta\nu_i^a = K_i\mu_a + F_i\delta\langle r_a^2\rangle + y_{\mathrm{e}}y_{\mathrm{n}}X_i\gamma_a. \tag{2.27}$$

Modifying the IS of two transitions (Eq. 2.25) and replacing the united nucleus parameter $\mathrm{m}\delta\langle r_a^2\rangle$ results in

$$\mathrm{m}\delta\nu_2^a = \frac{F_2}{F_1}\cdot\mathrm{m}\delta\nu_1^a + \left(K_2 - \frac{F_2}{F_1}K_1\right) + y_{\mathrm{e}}y_{\mathrm{n}}\cdot\left(X_2 - \frac{F_2}{F_1}X_1\right)\cdot\mathrm{m}\gamma_a. \tag{2.28}$$

Similar to Eq. 2.26, the King-linearity term shows up, however, the NP contribution leads to an additional term. This term will result in a deviation from the expected linear behavior, i.e. a non-linearity (NL), unless it falls under one of two exceptions. Firstly, if the electronic coefficients F and X are equal or at least very similar, the term $X_2 - \frac{F_2}{F_1}X_1 = 0$ and no NL occurs. Secondly, if $\mathrm{m}\gamma_a$ is aligned with the one of the SM terms, then the fifth force contribution would be disguised as part of this SM shift. This alignment occurs when $N_A - N_{A_r}$ is proportional to either $1/m_A - 1/m_{A_r}$ or $\langle r_A^2\rangle - \langle r_{A_r}^2\rangle$ for the investigated isotopes.

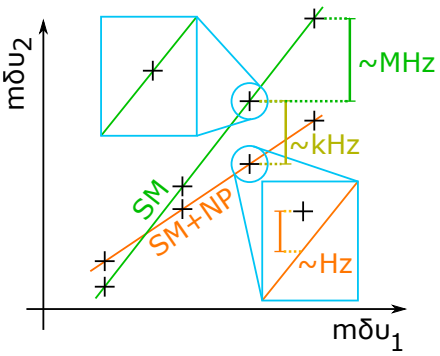

Figure 2.6: Scheme of a KP (not in proportions). Green represents the SM-only contribution, where the points are in $\mathcal{O}$(MHz) away from each other. The NP contribution in orange shifts this by $\mathcal{O}$(kHz), but the nonlinearity is only in $\mathcal{O}$(Hz).

Generally, IS calculations result in a fifth force contribution on the order of a few kHz. In terms of NL, however, most is lost due to the common shift between different pairs in the KP. A depiction of this problem is shown in Fig. 2.6, where the SM leads to the King-linearity between the isotope pairs of a few MHz. The fifth force IS causes a kHz shift, but only a small fraction results in an

NL of a few Hz, which is why high-precision spectroscopy is needed. Analyzing this NL in terms of resolvability requires accounting for the IS measurement uncertainty. This can be approached in various ways, one of which is to look at the deviation of a third isotope-pair to a linearity established by the first two pairs. The resolvability follows a direct comparison of the deviation to the measurement uncertainty. On a more general approach, the area spanned by the isotope-pairs can be evaluated. As presented in Ref. [39], a matrix can be used for this

$$M^{\mathrm{KP}}_{a_1,a_2,a_3} = \begin{pmatrix} \mathrm{m}\delta\nu_1^{a_1} & \mathrm{m}\delta\nu_2^{a_1} & 1 \\ \mathrm{m}\delta\nu_1^{a_2} & \mathrm{m}\delta\nu_2^{a_2} & 1 \\ \mathrm{m}\delta\nu_1^{a_3} & \mathrm{m}\delta\nu_2^{a_3} & 1 \end{pmatrix}. \tag{2.29}$$

This matrix contains the two mass-modified IS for the different isotope pairs a, which represent the set of linear equations. Since the IS have been divided by the mass parameter, the last column contains only $\overrightarrow{\mathrm{m}\mu} = (1,1,1)^T$, i.e. μ divided by μ. Since the radius parameter has been replaced by $\delta\nu_2$, it is the second column. The determinate of this matrix is the volume of the parallelogram spanned by the isotope vectors $\overrightarrow{\mathrm{m}\delta\nu_1}$, $\overrightarrow{\mathrm{m}\delta\nu_2}$ and $\overrightarrow{\mathrm{m}\mu} = (1,1,1)^T$

$$\begin{aligned} V^{\mathrm{KP}}_{a_1,a_2,a_3} =& \det\left(M^{\mathrm{KP}}_{a_1,a_2,a_3}\right) \\ =& \mathrm{m}\delta\nu_1^{a_1}\left(\mathrm{m}\delta\nu_2^{a_2} - \mathrm{m}\delta\nu_2^{a_3}\right) \\ &- \mathrm{m}\delta\nu_1^{a_2}\left(\mathrm{m}\delta\nu_2^{a_1} - \mathrm{m}\delta\nu_2^{a_3}\right) \\ &+ \mathrm{m}\delta\nu_1^{a_3}\left(\mathrm{m}\delta\nu_2^{a_1} - \mathrm{m}\delta\nu_2^{a_2}\right). \end{aligned} \tag{2.30}$$

Using Gaussian error propagation through the determinate, one can obtain the uncertainty of this volume, which includes the measurement uncertainties of every isotope-pair and transition

$$\begin{aligned} \Delta V^{\mathrm{KP}}_{a_1,a_2,a_3} =& \Delta\mathrm{m}\delta\nu_1^{a_1}|\mathrm{m}\delta\nu_2^{a_2} - \mathrm{m}\delta\nu_2^{a_3}| + \Delta\mathrm{m}\delta\nu_1^{a_2}|\mathrm{m}\delta\nu_2^{a_1} - \mathrm{m}\delta\nu_2^{a_3}| \\ &+ \Delta\mathrm{m}\delta\nu_1^{a_3}|\mathrm{m}\delta\nu_2^{a_1} - \mathrm{m}\delta\nu_2^{a_2}| + \Delta\mathrm{m}\delta\nu_2^{a_1}|\mathrm{m}\delta\nu_1^{a_3} - \mathrm{m}\delta\nu_1^{a_2}| \\ &+ \Delta\mathrm{m}\delta\nu_2^{a_2}|\mathrm{m}\delta\nu_1^{a_1} - \mathrm{m}\delta\nu_1^{a_3}| + \Delta\mathrm{m}\delta\nu_2^{a_3}|\mathrm{m}\delta\nu_1^{a_2} - \mathrm{m}\delta\nu_1^{a_1}|. \end{aligned} \tag{2.31}$$

With this calculated parallelogram by the NL and its uncertainty from the measurements, the resolvability R can be defined as

$$R = \frac{V^{\mathrm{KP}}_{a_1,a_2,a_3}}{\Delta V^{\mathrm{KP}}_{a_1,a_2,a_3}}. \tag{2.32}$$

If $R > 1$, the area of the parallelogram can be resolved; while a $R \leq 1$ signifies an area below the resolution of the measurement. This property is used later in the analysis of KPs.

2.3.3 No-mass King plot

A possible limitation of for the KP analysis can stem from uncertainties of the isotope masses, as

$$\begin{aligned} \mathrm{m}\delta\nu_i^a &= \frac{\delta\nu_i^a}{\mu_a} = \frac{\nu_i^A - \nu_i^{A_r}}{1/m_A - 1/m_{A_r}} \\ \Delta\mathrm{m}\delta\nu_i^a &= \frac{\Delta\nu_i^A + \Delta\nu_i^{A_r}}{|1/m_A - 1/m_{A_r}|} + \frac{\Delta m_A m_A^{-2} + \Delta m_{A_r} m_{A_r}^{-2}}{(1/m_A - 1/m_{A_r})^2}|\nu_i^A - \nu_i^{A_r}|. \end{aligned} \tag{2.33}$$

High Δm_A or Δm_{A_r} can overshadow the measurement uncertainty. In this case, the mass parameter from the IS can be exchanged for a third transition. The relation $\overrightarrow{\mathrm{m}\mu} = (1,1,1)^T$ in the matrix Eq. 2.29 stems from the isotope-independent term $K_2 - K_1 \cdot F_2/F_1$ in Eq. 2.28. By keeping the IS unmodified and instead exchanging the mass parameter with a third measurement, the set of linear equations is a so-called no-mass King plot (NmKP) [39]. The NmKP matrix is

$$M_{a_1,a_2,a_3}^{\mathrm{NmKP}} = \begin{pmatrix} \delta\nu_1^{a_1} & \delta\nu_2^{a_1} & \delta\nu_3^{a_1} \\ \delta\nu_1^{a_2} & \delta\nu_2^{a_2} & \delta\nu_3^{a_2} \\ \delta\nu_1^{a_3} & \delta\nu_2^{a_3} & \delta\nu_3^{a_3} \end{pmatrix}. \tag{2.34}$$

Similar to Eq. 2.30, the volume of the parallelogram formed by the vectors can be obtained by the determinant of the matrix

$$V_{a_1,a_2,a_3}^{\mathrm{NmKP}} = \det\left(M_{a_1,a_2,a_3}^{\mathrm{NmKP}}\right). \tag{2.35}$$

Now, the uncertainty of the volume $\Delta V_{a_1,a_2,a_3}^{\mathrm{NmKP}}$ only depends on the measured IS $\Delta\delta\nu_i^a = \Delta\nu_i^A + \Delta\nu_i^{A_r} \approx 2\Delta\nu$.

2.3.4 Higher-order SM shifts

Nuclear effects have an undeniable influence on the electronic levels and transitions. While the finite nuclear size and the nuclear mass have the strongest effect, there are potentially smaller contributions which may become relevant in IS. This appearance of smaller effects with increased precision is shown schematically in Fig. 2.7. While large measurement uncertainties would make the nucleus seem spherical, finer precision may reveal small deformations, and an even fur-

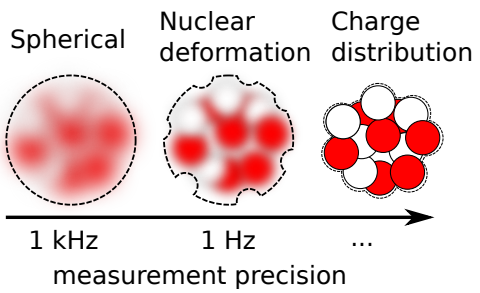

Figure 2.7: Scheme of the visible effects by the nucleus for different measurement uncertainties.

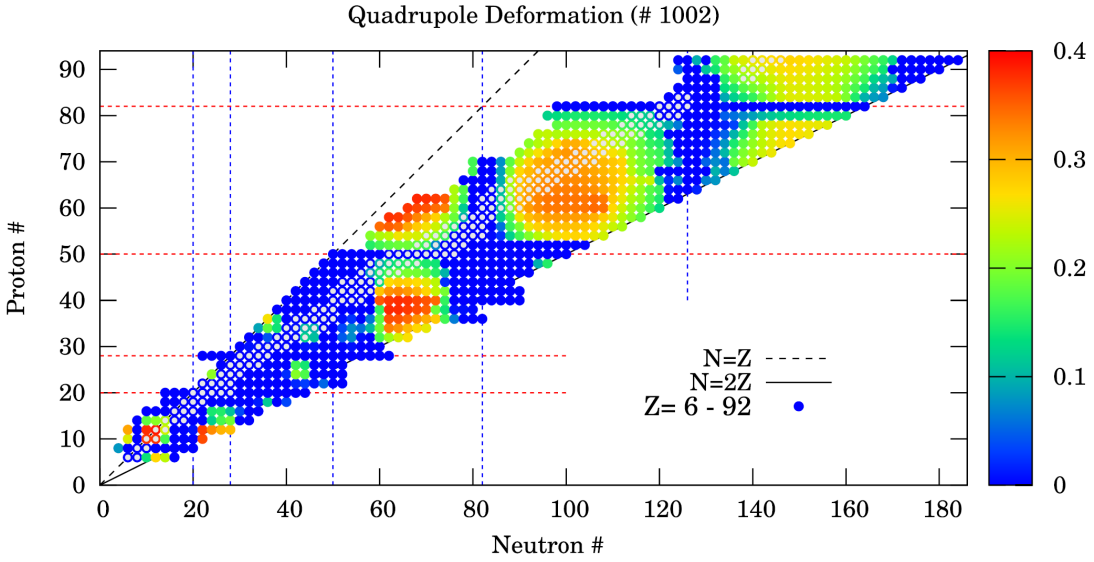

Figure 2.8: Quadrupole deformation parameter of even isotopes. Empty circles represent stable isotopes. Blue: spherical nucleus, red: spheroidal deformed nucleus. From Ref. [104].

ther improved precision may reveal the precise distribution of the charges in the nucleus affecting the electrons. These effects could also be seen in perturbation theory as higher-orders of the SM. [100, 101]

Quadratic mass-shift The quadratic mass-shift (QMS) is a higher-order term to the MS. It can be explained as a nuclear recoil, where the electrons exert a force on the nucleus [102]. This effect is more significant in lighter atoms than in heavier ones. Calculations estimated the QMS for calcium to be on the order of 3 Hz for Ca^+ [103]. This would be observable with sub-Hz precision using current laser spectroscopy and QLS. In IS, the QMS adds a term $M \cdot \mu^2$, where M is an electronic coefficient, and is thus treated as a perturbation to the existing MS $K \cdot \mu$.

Quadratic field-shift The quadratic field-shift (QFS) is a higher-order contribution to the FS, which is typically on the order of a few kHz for heavy atoms. This effect becomes dominant in heavy atoms, due to the increased nuclear charge and consequently the relativistic corrections. These relativistic terms will cause the field shift to be stronger further away from the nucleus [103]. This can be treated either as a nucleus-dependent FS parameter $F(a)$, or as an added perturbation term $G \cdot (\delta\langle r^2 \rangle)^2$ [100] with an electronic coefficient G.

Nuclear deformation Some combinations of neutron and proton numbers allow for non-spherical patterns. This nuclear deformation affects the energy levels of the electrons.

Until recently, the effects of nuclear deformation have been underestimated on their role in IS. Its significance became evident only after the analysis of an NL observed in a KP analysis in ytterbium [41, 105]. Calculations from Ref. [104] of the deformation for different nuclei are shown in Fig. 2.8. As a dipole deformation is simply a positional shift of the nucleus, the quadrupole deformation is the lowest deformation term and describes the shape of a spheroidal nucleus [106]. There are patches with strong nuclear deformation seen in Fig. 2.8. Magical numbers (20, 28, 50, 82, 128), which are indicated with red and blue dashed lines, are correlated with spherical nuclei. Best examples are Ca, Ni, Sn and Pb. A large variety of nuclear deformed isotopes are found in ytterbium with $Z = 70$ protons. While Ca has a magical $Z = 20$, Xe has some slightly deformed isotopes ^{124}Xe through ^{128}Xe, however, their deformation parameter is still smaller than that of Yb. According to Ref. [100], the IS terms would written as $a\Delta(\beta^2) + b\Delta(\beta^3) + c\delta\langle r^2\rangle\Delta(\beta^2)$ with a, b and c as electronic constants and β the quadrupole deformation parameter, where $\Delta(\beta^2) = \beta_1^2 - \beta_2^2$ and $\Delta(\beta^3) = \beta_1^3 - \beta_2^3$.

Ref. [104] also investigates the effect of the next higher-order, an octupole deformation, which would describe a pear-shaped nucleus. However, this kind of deformation is irrelevant for the isotopes of the elements analyzed and discussed in this work, therefore will not be included here.

Nuclear polarizability The nuclear polarizability α_p can also have an influence on isotopes. This effect arises especially in large nuclei which affects the electronic wavefunctions via the nuclear giant dipole resonance, and via the rotational states in deformed nuclei. Its potential can be written as

$$V_{\alpha_p} = -\frac{1}{2}\frac{\alpha_p e^2}{r^4}. \tag{2.36}$$

The isotope dependency lies within α_p, which depends on a combination of Z and A. The reduction by r^4 makes this effect most substantial in close proximity to the nucleus, thus s-orbitals are most significantly affected, while effects on p-orbitals are already magnitudes lower. This effect is rather small for Ca and Xe, especially compared to heavier elements like Yb. [107]

The nuclear polarizability relies on a number of nuclear parameters, which makes separation of the nuclear- and non-nuclear-dependent parts difficult. As an IS term, it will be handled as one single parameter $\delta\nu_{\alpha_p}$ [108].

2.3.5 Generalized King plot

By including all these contributions in the IS equation Eq. 2.27, the shift terms become numerous

$$\begin{aligned}\delta\nu_i^a =& K_i\mu_a + F_i\delta\langle r_a^2\rangle \\ &+ M_i\mu_a^2 + G_i\cdot(\delta\langle r^2\rangle)^2 + a_i\Delta(\beta^2) + b_i\Delta(\beta^3) + c_i\delta\langle r^2\rangle\Delta(\beta^2) + \delta\nu_{\alpha_p} \\ &+ y_e y_n X_i\gamma_a.\end{aligned} \tag{2.37}$$

Each term has a unique dependence on the nucleus of an isotope and shifts the energy levels accordingly. This property could be used to distinguish these effects, and a method will be discussed in chapter 2.3.6. However, it becomes necessary to focus on the main contributions visible with a given measurement uncertainty. For spherical nuclei, like Ca, the β terms will not play a significant role. For slight deformations, like in some Xe isotopes, the main shift lies within the $\Delta\beta^2$ term, however, compared to Yb, this shift is expected to be much smaller. The nuclear polarizability is expected to become most visible in heavy nuclei, because of the greater overlap of the electronic wavefunction with the nucleus. Due to its short range, only the innermost electrons are sufficiently experiencing it to be detected. This leaves predominantly the QMS and QFS as SM NL.

Each of these higher-order SM terms contribute to the NL. To separate them, the GKP has been developed by Refs. [37, 39]. Here, the KP is extended with additional transitions into higher dimensions. Each higher dimension counters one higher-order SM effect, without the need to know the specific details of that term [39]. Similar to the KP linearity Eq. 2.28, the GKP spans a mutli-dimensional linearity, a hyperplane, through the SM terms. However, each higher dimension requires another isotope-pair to remain a determined system.

To remove one higher-order SM term, the GKP becomes four dimensional. Here, the calculation of the volume with the determinant becomes advantageous, as the volume can still obtained with the determinant of the matrix

$$M^{\mathrm{GKP}}_{a_1,a_2,a_3,a_4} = \begin{pmatrix} \mathrm{m}\delta\nu_1^{a_1} & \mathrm{m}\delta\nu_2^{a_1} & \mathrm{m}\delta\nu_3^{a_1} & 1 \\ \mathrm{m}\delta\nu_1^{a_2} & \mathrm{m}\delta\nu_2^{a_2} & \mathrm{m}\delta\nu_3^{a_2} & 1 \\ \mathrm{m}\delta\nu_1^{a_3} & \mathrm{m}\delta\nu_2^{a_3} & \mathrm{m}\delta\nu_3^{a_3} & 1 \\ \mathrm{m}\delta\nu_1^{a_4} & \mathrm{m}\delta\nu_2^{a_4} & \mathrm{m}\delta\nu_3^{a_4} & 1 \end{pmatrix}, \tag{2.38}$$

$$V^{\mathrm{GKP}}_{a_1,a_2,a_3,a_4} = \det\left(M^{\mathrm{GKP}}_{a_1,a_2,a_3,a_4}\right). \tag{2.39}$$

If there is a large uncertainty reigning from the isotopes masses, the GKP can still overcome these uncertainties using the technique from the NmKP, forming the no-mass generalized King plot (NmGKP). As before, the last column of the matrix

is exchanged with a fourth transition. As the mass parameter μ is replaced with an IS, there is no need to modify these IS by the masses anymore

$$M^{\mathrm{NmGKP}}_{a_1,a_2,a_3,a_4} = \begin{pmatrix} \delta\nu_1^{a_1} & \delta\nu_2^{a_1} & \delta\nu_3^{a_1} & \delta\nu_4^{a_1} \\ \delta\nu_1^{a_2} & \delta\nu_2^{a_2} & \delta\nu_3^{a_2} & \delta\nu_4^{a_2} \\ \delta\nu_1^{a_3} & \delta\nu_2^{a_3} & \delta\nu_3^{a_3} & \delta\nu_4^{a_3} \\ \delta\nu_1^{a_4} & \delta\nu_2^{a_4} & \delta\nu_3^{a_4} & \delta\nu_4^{a_4} \end{pmatrix} \tag{2.40}$$

The more SM IS terms there are to account for, the further the GKP can be expanded into higher dimensions.

$$M^{\mathrm{NmGKP}}_{a_1,a_2,a_3,a_4,\ldots} = \begin{pmatrix} \delta\nu_1^{a_1} & \delta\nu_2^{a_1} & \delta\nu_3^{a_1} & \delta\nu_4^{a_1} & \cdots \\ \delta\nu_1^{a_2} & \delta\nu_2^{a_2} & \delta\nu_3^{a_2} & \delta\nu_4^{a_2} & \\ \delta\nu_1^{a_3} & \delta\nu_2^{a_3} & \delta\nu_3^{a_3} & \delta\nu_4^{a_3} & \\ \delta\nu_1^{a_4} & \delta\nu_2^{a_4} & \delta\nu_3^{a_4} & \delta\nu_4^{a_4} & \\ \vdots & & & & \ddots \end{pmatrix} \tag{2.41}$$

The only limit to this method is the number of transitions and available isotopes.

The resolvability R is calculated for any of these KP methods (KP, NmKP, GKP or NmGKP) with $R = V/\Delta V$. This R is used in the analysis of the KPs to investigate their sensitivity to a fifth force.

2.3.6 Analyzing the breaking of the King plot linearity

In the theoretical analysis of the KPs, the parameters of the included Yukawa potential can be scaled accordingly. The resolvability R can be calculated using KP volumes and their uncertainties, and used to adjust the parameters $y_e y_n$ and m_Φ in the Yukawa model to achieve $R = 1$. This limit is reached when the $\mathrm{IS}_{\mathrm{NP}}$ shift is as large as the error bars, caused by the assumed measurement uncertainties. When repeated for all mediator masses m_Φ, this will result in a curve for an exclusion-plot as shown in Fig. 2.4. Details of this method will be given in the analysis chapters 5.1 and 5.2.

Analyzing experimentally acquired KPs is slightly different, as an observed NL sets the R to a fixed value. However, the resulting NL is still compared to the

Yukawa-model of the fifth force. For the classical KP, the solution for the coupling parameter is [109, 39]

$$y_e y_n = \frac{\left|\begin{pmatrix} m\delta\nu_1^{a_1} & m\delta\nu_2^{a_1} & 1 \\ m\delta\nu_1^{a_2} & m\delta\nu_2^{a_2} & 1 \\ m\delta\nu_1^{a_3} & m\delta\nu_2^{a_3} & 1 \end{pmatrix}\right|}{\left|\begin{pmatrix} X_1(m_\Phi)\cdot m\delta\nu_2^{a_1} - X_2(m_\Phi)\cdot m\delta\nu_1^{a_1} & m\gamma_{a_1} & 1 \\ X_1(m_\Phi)\cdot m\delta\nu_2^{a_2} - X_2(m_\Phi)\cdot m\delta\nu_1^{a_2} & m\gamma_{a_2} & 1 \\ X_1(m_\Phi)\cdot m\delta\nu_2^{a_3} - X_2(m_\Phi)\cdot m\delta\nu_1^{a_3} & m\gamma_{a_3} & 1 \end{pmatrix}\right|}, \tag{2.42}$$

which is only dependent on the measurement results $m\delta\nu$ and the theoretical model that is used to describe the fifth force $X(m_\Phi)$. Even if no breaking of the linearity occurred, the results can still be used to exclude the NP parameter space that is covered by that measurement. In essence, the fifth force model is maximized within the limits of measurement uncertainties without compromising the observed linearity.

Given the number of possible SM IS terms shown in Eq. 2.37, an observed NL could as well be caused by one or more of these terms. In particular, this can be problematic if it is an effect that was underestimated in the theoretical framework. A possible way to interpret the NL from an observation is to analyze the pattern the isotope-pairs exhibit in the KP. For four isotope-pairs, it can either follow a zigzag $(+ - + -)$, or a curved $(+ - - +)$ pattern. As no measurement strictly follows these patterns to perfection, a mixture of zigzag and curved patterns is expected, which can be visualized in a plot. In such a plot, the different IS terms draw a line that expresses the pattern ratio of that shift. This ratio of these patterns is different for each term of Eq. 2.37 on the isotopes. A KP analysis would mark a single point on this plot, which is spread out by its uncertainties. This plot allows the distinction of an NP shift from a SM shift. Recently, this method was used on a Yb KP measurement [41, 105]. The analysis led to identification of a nuclear deformation, instead of a NP boson, that caused the observed NL. The nuclear deformation was until then supposedly negligible in its effects on the KP analysis. The initial analysis was done in Counts et al. [41] with this pattern plot method, which is shown in Fig. 2.9. Here, $\zeta_\pm$ is the pattern obtained with

$$\zeta_+ = d_a - d_b + d_c - d_d, \zeta_- = d_a - d_b - d_c + d_d, \tag{2.43}$$

where $d_x = m\delta\nu_i^x - f(m\delta\nu_j^x)$ being the vertical offset of the data points $m\delta\nu_i^x$ from the linear fit function $f(m\delta\nu_j^x)$. The isotope is denoted with x and the two transitions are i and j. In this figure, two lines are drawn, each representing a particular ratio of zigzag to curved. For a fifth force, the ratio dependence is plotted in green, while a QFS is seen as a blue dashed line. Both ratios could explain the red circle where the

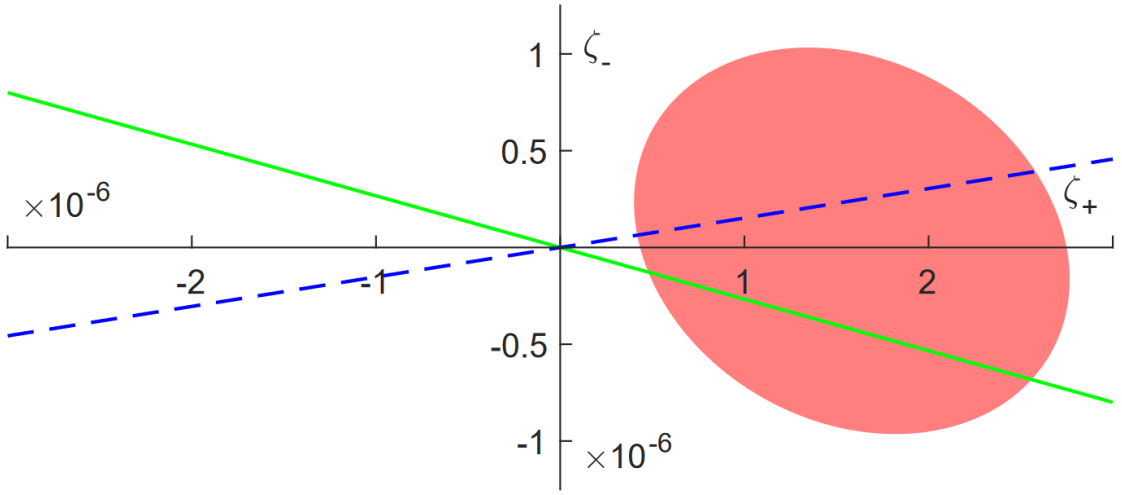

Figure 2.9: Pattern plot from Ref. [41]. Green line represents NL behavior for a pure NP boson, while the blue dashed line is the expected pattern for a QFS. The red area is where the measurement lies including its uncertainty.

measurement lies. If the measurement is improved further, the red circle will become smaller and may end up on one of these ratio lines. This would be a clear indication of what effect is present. The more IS components, the more lines would be drawn. Since this particular figure was a preliminary analysis, the nuclear deformation was not yet accounted for.

This method works best for four isotope-pairs, as there are only two possible patterns for the NL. More isotope-pairs would allow for more patterns, which would complicate this analysis by expanding the plot into higher dimensions for each pattern.

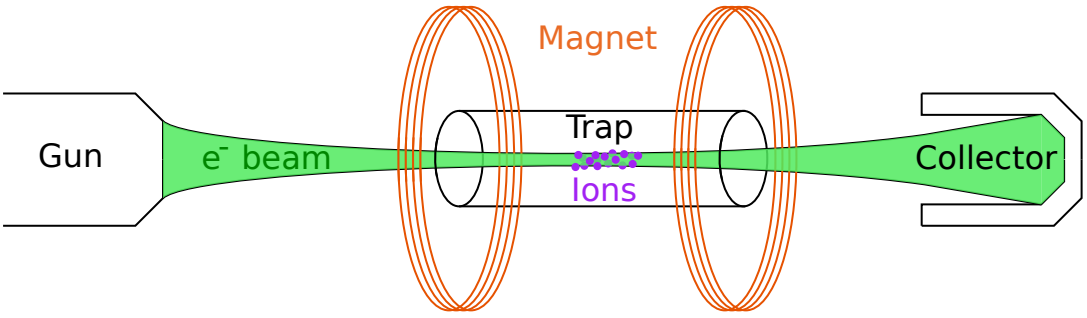

Figure 2.10: General setup of an EBIT. An electron gun generates an electron beam, which is guided by an magnetic field to a collector. The ions are produced in the central trap region.

2.4 Electron Beam Ion Trap

Numerous isotopes and transitions are required for the KP and the subsequent GKP analysis. Additionally, to make use of future high-precise QLS measurements, ground-state transitions are required. In chapter 2.1.1 the advantages of HCIs on precision measurements have been elucidated.

To produce these HCIs, an electron beam ion trap (EBIT) is commonly used. A general setup is depicted in Fig. 2.10. In these EBITs, an electron gun is heated to release electrons, which are then accelerated by the potential difference between a cathode and the central trap. The acceleration voltage ranges from a few tens of volts to several hundred kilovolts. A magnetic field guides and compresses the electron beam. The energy of the electron beam is determined by the acceleration voltage, which in turn allows the beam to strip electrons from atoms crossing its path. The electrons can be progressively stripped away by the sheer number of electrons emitted by the gun. The limit is reached when the ionization energy of the bound electron is greater than the beam energy. This limits the charge state of the produced ions. There is a collector at the end of the EBIT, which stops the electrons in their path and dissipates the heat generated from the electron impact. Details of the setup are discussed in chapter 3.1.

Interactions between the electron beam and an injected atom are highly dependent on the beam energy. Firstly, it may excite an electron of the atom A to a higher energy level A^*, which eventually returns to a lower level and the energy difference is released as a photon $h\nu$

$$A + e^- \rightarrow A^* + e^- \rightarrow A + h\nu + e^-. \tag{2.44}$$

This is also known as fluorescence. An empirical formula from Van Regemorter [110] allows an estimation of the cross-section of the excitation process

$$\sigma_{\text{Regemorter}} \approx 2.36 \times 10^{-13}\,\text{cm}^2\text{eV}^2 \frac{1}{E_{\text{beam}}^2} \frac{G \cdot f_{ki}}{h\nu}. \tag{2.45}$$

Here, a transition is excited by an electron beam with the energy E_{beam}. The transition has an energy of $h\nu$ and the absorption oscillator strength f_{ki}, where the latter is scaled by an empirical Gaunt factor $G = 0.074\sqrt{E_{\text{beam}}/h\nu} \cdot (1 + E_{\text{beam}}/h\nu)$ [110].

If the electron in the beam has more energy than the ionization threshold, then the bound electron may be released

$$A + e^- \rightarrow A^+ + 2e^-. \tag{2.46}$$

The released electron gains momentum from the interaction and will either travel with the beam to the collector, or spiral due to the electric and magnetic fields until it is stopped by a wall or another object. The empirical formula by Lotz [111] below can be employed to estimate the chance of ionization for beam energies E_{beam} close the ionization potential $E_{\text{ion.}}$.

$$\sigma_{\text{Lotz}} \approx 4 \times 10^{-14}\,\text{cm}^2\text{eV}^2 \cdot N_{\text{e}} \frac{\ln\left(E_{\text{beam}}/E_{\text{ion.}}\right)}{E_{\text{ion.}}^2} \cdot (1-b), \tag{2.47}$$

where N_{e} is the number of the electrons which contribute to the cross-section of the subshell and a factor b based on experimental results. For $E_{\text{beam}} >> E_{\text{ion.}}$ this factor is $(1-b) = E_{\text{ion.}}/E_{\text{beam}}$ [111]. From this formula it follows that lighter bound electrons are easily removed from an atom, while tightly bound electrons require a more targeted hit for electron ionization. Therefore, a high electron density n_{e} of the beam becomes important to achieve high charge states. A high-energy photon is released when an electron recombines with the atom.

Ionization might become easier for when the atom A is already in an excited state. Typically, this requires a meta-stable state, which has a longer lifetime than other states due to the lack of fast decaying transitions.

$$A^* + e^- \rightarrow A^+ + 2e^- \tag{2.48}$$

The radial extent of the beam for an ideal system is described by the Brillouin radius

$$r_{\text{B}} = \sqrt{\frac{m_{\text{e}} I}{\pi\epsilon_0 \sqrt{2eU_c/m_{\text{e}}}\, B^2}}\,, \tag{2.49}$$

with current of the electron beam I, and the cathode voltage U_c.

As the beam consists of electrons that repel each other but attract positively-charged ions, it directly affect EBIT operations. To estimate its electromagnetic influence, the beam can be approximated as a homogeneously charged rod. The potential of such a rod of indefinite length is

$$\Phi(r) = \frac{\rho}{2\pi\epsilon_0} \ln \frac{r}{r_{\text{out}}}, \tag{2.50}$$

where r_{out} is the limit posed by an outer surface, which is set by the radius of the trap electrodes. The electron density of the rod ρ can be further estimated on average

$$\rho = \frac{Q}{A} = \frac{I}{\sqrt{2eU_c/m_{\text{e}}}\,\pi r_{\text{B}}^2}. \tag{2.51}$$

To relate Q to the current, the definition for the current can be used $I = Q/t = Q \cdot L/v$ to obtain $Q = I \cdot L/v$, where L is the length. The area A for a cylindrical rod is $A = \pi r_B^2 L$ where the Brillouin radius defines its thickness. The velocity v is further substituted with the kinetic energy of the electrons obtained by the acceleration potential U_c. The spatial extent of the electron beam changes the potential in the inner region $r \leq r_B$ to [112]

$$\Phi_{\text{inner}}(r) = \frac{\rho}{2\pi\epsilon_0}\left(\frac{r^2}{r_B^2} - \frac{1}{2} - \ln\frac{r_B}{r_{\text{out}}}\right). \tag{2.52}$$

This potential is known as the space charge potential and reflects the effect the electrons have on the trap and on the beam, which results in an electron beam energy of

$$E_{\text{beam}} = e(U_c - \Phi_{\text{inner}}(r = 0)). \tag{2.53}$$

This is evident for the acceleration, which is set by the potential difference between the cathode and the center of the trap.

The electron beam is guided by a magnetic field. The higher the magnetic field, the stronger the confinement of the beam, and with a stronger compression of the beam, an increased electron density n_e. A high n_e would achieve a more narrow charge state distribution than a low n_e. This would improve targeting of specific charge states and thus a higher intensity yield (see chapter 2.1.2). The advantage of an EBIT over an EBIS is that it traps the produced ions directly and keeps the ions in a fairly steady charge state distribution. The ions are trapped radially by the magnetic field and the aforementioned space charge of the beam, while electrical fields trap the ions axially. The well-like electric field is generated by trap electrodes which cause a lower field in the center of the trap and a higher field either end of the trap. This keeps the ions centered near a window for observational purposes.

2.5 Spectrometer

To measure the spectrum of trapped ions, a spectrometer is used. It must have a wavelength dispersing component, which can be either a prism, a transmission grating, or a reflective grating. A Czerny-Turner spectrometer, as used in this work, typically contains a reflective grating. In our case, this is either a blazed or holographic grating. The former has reflective edges that have a collective angle in relation to the grating normal. The Czerny-Turner setup, as depicted in Fig. 2.11 (a), contains two curved mirrors which collimate the light into the reflective grating and refocus the diffracted light onto a detector.

2.5.1 Blazed grating

As with any grating, the blazed grating can be parameterized with an incident angle α and diffraction angle β with the grating equation

$$n\lambda = \frac{1}{k}(\sin(\alpha) + \sin(\beta)), \tag{2.54}$$

where n is the order of interference, λ the wavelength and k the groove density of the grating. The zeroth-order $n = 0$ is fulfilled when $\alpha = -\beta$, i.e. when a reflective grating reflects the light like a mirror. This is depicted in Fig. 2.11 (b) as the black outgoing line has the same angle as the incident line. As the wavefront is scattered of the grating surface, different outgoing beams coincide, forming an interference pattern depending on their wavelength. This can be seen in Fig. 2.11 (b) where the blue line under the angle β_1 is the first-order of interference for photons with a shorter wavelength as compared to the red line under the angle β_2, which represents a longer wavelength. A higher-order interference can be seen at different angle, here shown for the blue line under angle β_1'. In practice, the grating is angled so that the desired wavelength is in view of the detector. If the blue line is at 300 nm then the second-order would be visible at 600 nm. If the red line would be at 400 nm, it would be visible with an angle in between $\beta_1 < \beta_2 < \beta_1'$.

Blazed gratings are typically blazed to one single wavelength. Its normal n_b is dotted in the Fig. 2.11 (b). The blaze angle is between n_g and n_b. The optimal wavelength for such a grating is when the outgoing angle is parallel to the blaze normal n_b. This makes it ideal for wavelengths around this blazed angle wavelength, and deviation from this wavelength reduces the signal strength.

Another type of grating is the holographic grating. Instead of sharp edges, it has a sinusoidal structure [113]. An example is depicted in Fig. 2.11 (c). Its efficiency is reduced compared to the blazed grating, however, its diffraction is less prone to errors due its grooves made with laser light interference on a surface. Because holographic gratings do not have a blazed angle, a wider wavelength range can be measured with a continuous, though reduced, efficiency.

The polarization dependence of the reflectivity varies strongly for different gratings. However, the reflectivity of p-polarized light is generally reduced for larger wavelengths of $\gtrsim 500$ nm [114]. This behavior can be attributed to the similitude between the wavelength and groove width. A polarization perpendicular to the groove lines would lead to a loss of efficiency, while a parallel polarization would be less affected.

To obtain a relation between the output angle β and the wavelength for a fixed incident angle α, Eq. 2.54 is derived by the angle β yielding

$$\frac{\delta\lambda}{\delta\beta} = \frac{\delta}{\delta\beta}\frac{1}{nk}(\sin(\alpha) + \sin(\beta)) = \frac{1}{nk}\cos\beta, \tag{2.55}$$

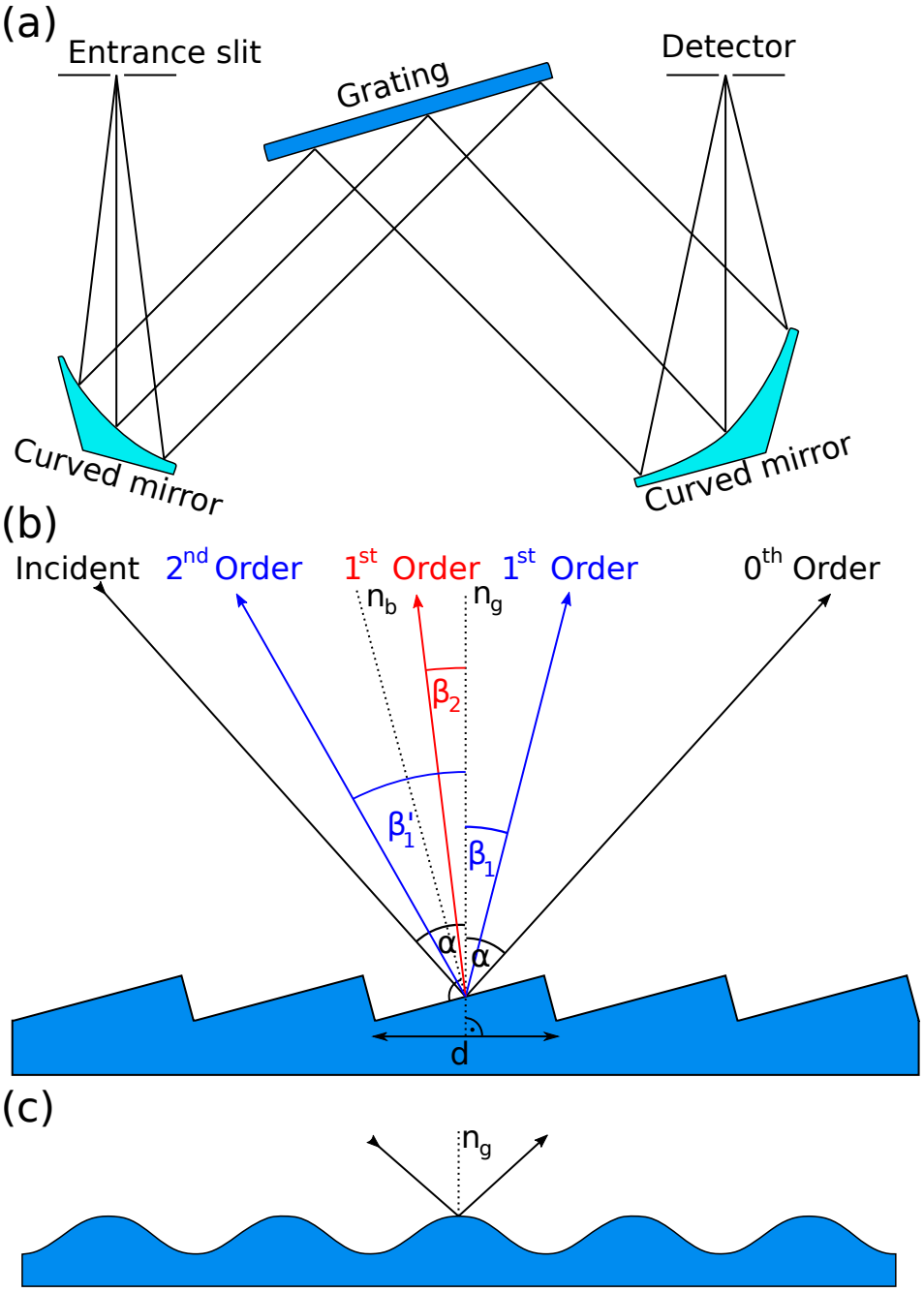

Figure 2.11: (a) Scheme of a Czerny-Turner spectrometer configuration, in which a curved mirror collimates light onto a grating. The dispersed light is refocused onto the detector by a second curved mirror. (b) Scheme of a blazed grating. Incident and zeroth-order (mirror-like) lines are shown in black. A short wavelength photon is shown in blue with its first- and second-order of interference. A longer wavelength is shown in red. The normal to the whole grating is n_g and to the blazes is n_b. (c) Scheme of a holographic grating.

which is usually expressed as

$$\frac{\delta\beta}{\delta\lambda} = \frac{nk}{\cos\beta}. \tag{2.56}$$

This relation shows that either a grating with higher groove density, or a higher-order, improves the resolution, as the angle $\delta\beta$ has to vary more to cover the same wavelength range $\delta\lambda$.

2.5.2 Dispersion function

The dispersion caused by the grating can be described by the dispersion function D. It can be described via

$$D(\lambda) = \frac{\delta\lambda}{\delta p} = \frac{\delta\lambda}{\delta\beta}\frac{\delta\beta}{\delta p} = \frac{d\cos\beta}{n}\frac{\delta\beta}{\delta p}. \tag{2.57}$$

A relation between the position p and the wavelength λ can then be established by integrating the dispersion function D

$$\lambda = \lambda_0 + \int_{p_0}^{p} D(\lambda)\mathrm{d}p' \tag{2.58}$$

However, the dispersion function is not known and thus is usually described by an approximation by comparing known wavelengths with their position on the detector, i.e. $\delta\lambda/\delta p$ of Eq. 2.57. For this comparison, a polynomial function of statistically significant order is applied to known lines of a calibration lamp. The statistical significance arises from the resulting uncertainty of the polynomial and its fit to the data. The model has to describe the data to a satisfactory degree, if the residuals still inhibit a systematical shape, the degree of the polynomial has to be increased. If the degree of the polynomial is appropriate, the uncertainties of the fit parameters need to be investigated. While a high degree would always predict the data points, each additional parameter carries added uncertainty.

2.6 Computation codes

Analyzing an atomic system requires knowledge about the energy levels and their properties, like total angular momentum, g-factors, level mixing and such. The complexity of the system is governed by the number of electrons to consider in the calculations, in particular the number of free valence electrons in an open shell. Typically, the fewer degrees of freedom in an open shell, the better the calculation results. For example, calculation of the $4d^1$ shell is more accurate than the $4d^2$, which is more accurate than the $4d^3$ and so on. If there are fewer 'holes' than electrons, then the holes can be used in the calculation instead of the electrons. This would mean a

$4d^9$ system can be calculated as accurately as a $4d^1$. Thus, half-open shells are the most difficult systems to consider, due to their equally high number of electrons and holes.

There is a wide variety of codes to use - some designed for a simpler handling for the price of accuracy, while others require some initial information about the system to provide more accurate results. In the following, FAC [86] and AMBIT [85] will be presented, both of which can be handled with relative ease.

Usually numerical calculations of this kind are needed for complicated systems with multiple electrons, requiring calculation of these electrons around the nucleus and their interactions, even when they are not directly involved in the excitation process. For many electrons the Schrödinger equation Eq. 2.1 can be written as

$$H\Psi = \left(\sum_i -\frac{h^2}{2m}\nabla_i^2 - \frac{Ze^2}{r_i} + \sum_{i<j} \frac{e^2}{r_{ij}} \right) \Psi = E\Psi. \tag{2.59}$$

Here, the third term is an correlation term for electron-electron interactions. As their distance r_{ij} is practically impossible to be computed for multiple electrons, the calculation of the energy levels can be difficult. Sometimes the potential also includes a term B_{ij}, known as Breit operator, to account for further effects between the electrons, like spin-spin, magnetic interactions, and retardation [115].

2.6.1 Flexible Atomic Code

FAC [86] is based on Dirac-Fock and the configuration interaction (CI) method, which are optimized for a given configuration. The electrons are separated into valence electrons, which are free to undergo excitation processes, and frozen or inert core electrons.

To overcome the electron-electron interaction problem of Eq.2.59, the wavefunction Ψ is approximated with a spatial factorization $\Psi = \phi_1(1) \cdot \phi_2(2) \cdot ... \cdot \phi_N(N)$, and to account for the Pauli-principle it should then be written as a determinant [116]

$$\Phi = \frac{1}{\sqrt{N!}} \left| \begin{pmatrix} \phi_1(1) & \phi_1(2) & ... & \phi_1(N) \\ \phi_2(1) & \phi_2(2) & ... & \phi_2(N) \\ ... & ... & ... & ... \\ \phi_N(1) & \phi_N(2) & ... & \phi_N(N) \end{pmatrix} \right|. \tag{2.60}$$

Here, the ϕ are single electron wavefunctions for N electrons, which are separated by the spin and spatial coordinates of the other electrons $1...N$, resulting in a $N \times N$ matrix (Slater matrix). This is known as the Dirac-Fock approach and has proven

itself to be a good approximation for the wavefunction. The total wavefunction is then the sum of these matrices

$$\Psi = \sum_i c_i \Phi_i, \tag{2.61}$$

where c_1 to c_N are coefficients minimizing the energy $(H - E) \cdot \vec{c} = 0$, with $\vec{c} = (c_1, ..., c_N)^T$.

To perform FAC calculations, the considered configurations in the calculations have to be specified. This reduces the computation time because a large number of higher states, typically in the continuum, are not considered. This reduces accuracy compared to other codes. Sufficient accuracy can still be achieved with a selected set of configurations that can be found by trial and error. A specific example on how such calculations can be conducted can be found in appendix B for calcium. While FAC does not return g-factors, other ways need to be taken to obtain at least the initial estimation. Appendix C introduces such a way. It utilizes the GRASP [117] module JJ2LSJ to obtain the LS-notation from FAC by using a compatible output for the wavefunction, which can then be interpreted in that module. The output of the JJ2LSJ module includes the percentage of the level mixing and their respective LS-notation. From this LS-notation, the g-factors can be calculated via the Dirac formula Eq. 2.19.

An advantage of FAC over other codes is the collision radiative modelling (CRM), which is designed to calculate the excitation due to electron collisions in a plasma, which is the interaction with the electron beam. When these interactions are not accounted for, the intensity of a transition can only be estimated with their transition rates A_{ki}. However, the intensity or the radiant power is dependent on the population of atoms in the excited upper state, as seen in Eq. 2.7. While the change of population of the upper state does not have a simple solution as seen Eq. 2.8, a numerical approach accounts for the branching ratios of every level and the electron impact excitation. As seen in Eq. 2.45, the electron collision excitation cross-section is scaled with the energy of the electron beam [118]. From these excited states, the decay into all lower levels using the radiant power formula in Eq. 2.7 is calculated with their respective transition rates A_{ki}. This results in an overview of the expected transition intensities, which can be crucial in the identification process. It was shown in Ref. [119] that an electron density of around $n_e \approx 10^{11}\,\mathrm{cm}^{-3}$ yields good results, compared to the experimental data for low energy electron beams with low current.

Using the Yukawa potential, FAC is used to calculate the electronic $X(m_\Phi)$ parameters of the fifth force. Here, the potential is simply added, with scaling parameters of $y_e y_n$ and m_Φ, to the coulomb potential. To overcome numerical limitations of the calculations for such a small contribution to the energy, the fifth force strength is heavily exaggerated. By subtracting the transition without fifth

force influence, the X coefficient can be extracted, which in return can be scaled to appropriate strengths in the consecutive analysis. A more detailed description of how to acquire the IS coefficients will be included in chapter 5.

The advantage of FAC is that it is much easier to use than other software like GRASP [117] or COWAN [120], as it only requires the specified electronic configurations. The accuracy of the levels is stated to be about 1 eV [86] for EUV transitions. However, comparisons with measurements revealed a general relative uncertainty of about 20% for optical transitions, which lowers the absolute uncertainty to around 0.5 eV in the optical range. Unfortunately, this is about 100 nm in the wavelength scale, which can complicate analysis if there are many levels and transitions to consider.

2.6.2 AMBiT

Another easy-to-use code is AMBIT [85]. It is newer than FAC and is based on a slightly different approach of combining configuration interaction and many-body perturbation-theory (CI+MBPT). The CI calculation was described before and accounts for electron-electron interactions with a good precision. However, the interaction with the core electrons has significant influences on the wavefunction and its treatment becomes complicated in the CI method as the matrix becomes quite large. An alternative approach is to handle the core electrons with MBPT and modify the wavefunction of the CI valence electrons as a perturbation [35]. This allows for a more accurate calculation of heavy atoms or atoms with a complicated level structure.

In AMBIT, core and valence electrons are separated with a set Fermi-level marked by a colon `1s2 2s2 2p6 3s2: 3p6`. Everything beyond the Fermi-level can be excited into higher levels. If the Fermi-level is set too low, i.e. too many shells included, the calculation can lose a lot of otherwise achieved accuracy. The highest configurations for excitation in the CI calculation can be specified, known as the `ValenceBasis`, e.g. `8spdf` allows the valence electrons to be excited up to $n = 8$ in $l = 0(s)$ to $l = 4(f)$. This should be chosen within reason. When this basis is set too small, the calculation becomes too inaccurate, but when the basis is too large, the calculations become too extensive, which also leads to a loss of accuracy.

The configuration may require a relativistic notation. An example would be `4d5` ⇒ `4d2 4d+3`. In this notation, a part of the valence electrons are pushed back into the inert core electrons. The way the electrons are split is explained by the degeneracy of the shells. A listing of these degeneracies can be found in Tab. 2.3 for the lowest shells. From this list the degeneracy g_d of a d-shell is 4 to 6. This fraction is applied to the total number of electrons in the shell to spell out the relativistic notation.

Table 2.3: Relativistic shells according to the notation of Swirles [121]. Orbital quantum number l, principal orbital quantum number j and degeneracy $g_d = (2j + 1)$ are given. Adapted from Ref. [122].

Shell	$s_{1/2}$	$p_{1/2}$	$p_{3/2}$	$d_{3/2}$	$d_{5/2}$	$f_{5/2}$	$f_{7/2}$	$g_{7/2}$	$g_{9/2}$
l	0	1	1	2	2	3	3	4	4
j	1/2	1/2	3/2	3/2	5/2	5/2	7/2	7/2	9/2
g	2	2	4	4	6	6	8	8	10

Furthermore, a specification of the `LeadingConfigurations` can focus the calculation onto a specific configuration. This can be especially important at level crossings.

Lastly, the MBPT basis for the calculation can be set larger than the one for the CI calculation, because MBPT is faster to compute than CI. It is set with a given principal n and orbital l quantum number, like `30spdfgh`.

Achieving good results with AMBIT requires experimenting with the parameters. A sample code for performing an AMBIT calculation on a system in Xe can be found in appendix D. To calculate transition rates in AMBIT, only the type of transition, such as M1, is required. While this results in a line strength S in atomic units, a conversion to A_{ki} rates is given by Eq. 2.13, 2.14 and Eq. 2.15, which already include the conversion to SI.

The ab-initio results of AMBIT lie within $\approx 30\,\text{nm}$ of the measured values for optical transitions and are therefore more precise than those achieved in FAC. Furthermore, the results also contain an expectation value for the g-factors of each level. This offers a great basis to identify transitions. However, FAC still has the distinct advantage of being faster and easier to perform. Its CRM calculations can be invaluable for finding and identifying the strongest lines in a spectrum. Using both programs together gives the fastest and best option to identify experimental transitions.

Chapter 3

Experimental setup

Formerly known as FreEBIT [123], Heidelberg-EBIT (HD-EBIT) was used for the production and trapping of HCIs. Over its more than 20 operational years, it has endured production and measurement of HCIs of various elements. Currently, the HD-EBIT is mainly used to measure optical transitions. The HD-EBIT uses superconducting coils to generate an 8 T strong magnetic field to guide the electron beam. This field strength also provides a strong Zeeman splitting of the transitions, which allows for high precision spectroscopy and improved line identification.

3.1 Heidelberg-EBIT

The HD-EBIT is separated into three main sections: The gun section to emit the electrons, the central trap section to trap the produced ions, and the collector section where the electron beam is stopped and the electric circuit is closed.

3.1.1 Electron gun

A cross-section of the electron gun is depicted in Fig. 3.1. In the center a cathode is heated with about 10 W (7 V, 1.4 A) to approximately 1200°C to release electrons from the metal. To maintain such high temperatures and have a good electron emission, the gun has a cathode made from tungsten permeated with barium. An applied voltage on the cathode accelerates the freed electrons out of the electron gun. A focus electrode and anode are then used to adjust the flow and focus of the electrons. The HD-EBIT was designed for acceleration voltages of up to 350 kV [123], however, for optical spectroscopy voltages rarely exceed 2.5 kV, as the levels for most higher charge states would be too spread apart for optical transitions to occur. To magnetically guide the electron beam through the setup, a pair of superconducting Helmholtz coils are used, located around the trap. However, the magnetic field from these coils interferes negatively with the emission of the electrons from the gun. To

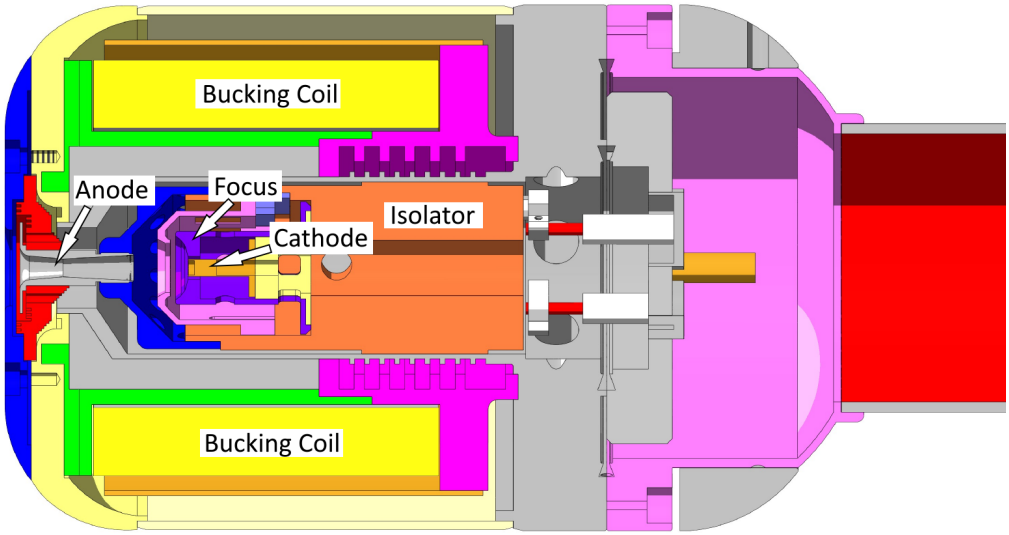

Figure 3.1: The electron gun of the HD-EBIT. A small electrode emits and accelerates electrons in respect to the potential at the trap center. The anode and focus electrodes adjust the beam. A bucking coil counters the magnetic field of the superconducting coils to improve electron emission.

reduce this field near the cathode, a soft-iron shielding (yoke) is placed at the front. To counter the residual field, a bucking coil is used, which is usually set to around 42 W (3 V, 14 A).

3.1.2 Trap and magnet

Placed between the electron gun and the collector, the trap section is depicted in Fig. 3.2. Around the trap, the aforementioned superconducting Helmholtz coils are placed inside a 4.2 K liquid He tank. This tank is insulated by two heat shields of 20 K and 50 K, which are cooled by a cryogenic compressor. The temperature of the lq. He allows the coils to become superconductive and carry a self-sustaining current of 76.24 A, which corresponds to an 8 T magnetic field in the center.

The 4.2 K tank can hold up to 50 L of lq. He, however, losses in the lq. He transfer and evaporative cooling of the warmer parts of the tank require approx. 80 – 100 L lq. He per filling. A full tank allows for approximately one week of operation of the EBIT, before the coils are exposed as the lq. He is gradually depleted. The quintupling of lq. He prices over the last few years, made the operation of the HD-EBIT excessively expensive. To reduce the high costs of ordering externally, a helium recovery system was installed early 2023 [124]. Here, the vaporized He is collected from the exhaust of the tank and compressed for storage in pressurized He gas bottles. These bottles are transferred to the Max-Planck Institute for Solid State Research in Stuttgart, where this gaseous He is liquefied and returned. This cycle

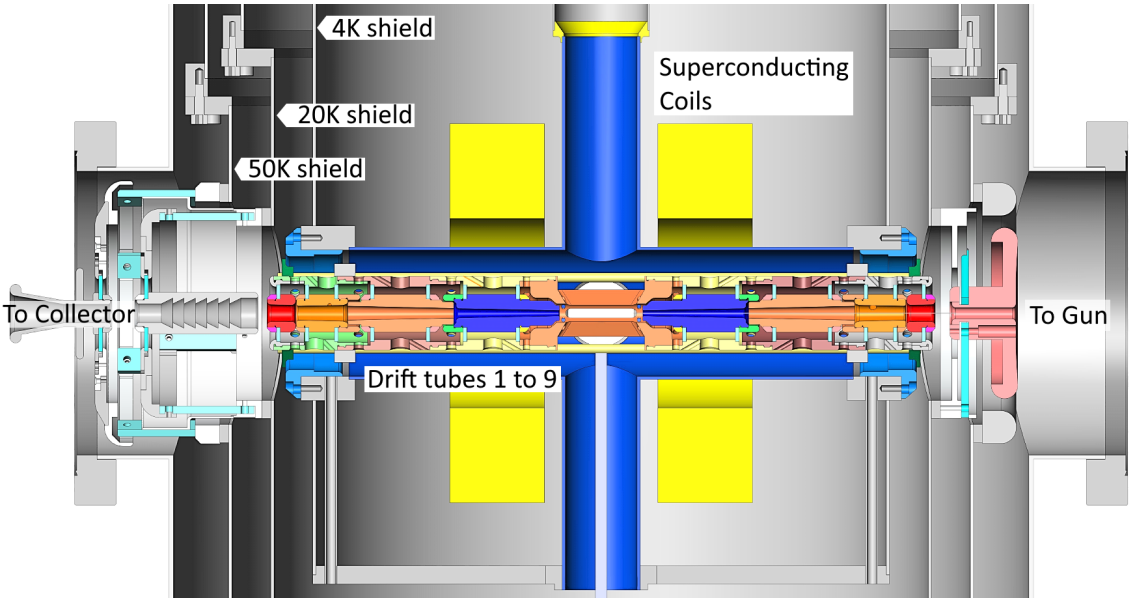

Figure 3.2: Trap region of the HD-EBIT. Superconducting coils inside a 4 K liquid He tank generate a magnetic field to guide the electron beam. The drift tubes are electrodes to trap the ions. To the right is the gun and to the left the collector.

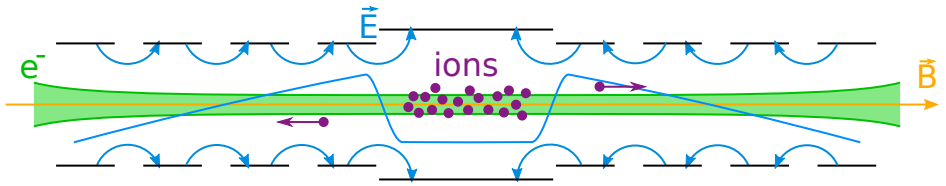

Figure 3.3: Scheme of the trap with magnetic field B guiding the electron beam. Drift tube electrodes generate an electric field between them and generating the depicted trapping potential in blue to keep the ions trapped inside the center.

allows a tenfold reduction of the prices. Besides the HD-EBIT, other lq. He requiring experiments, e.g. penning traps, are also connected to this recovery system.

A positive side-effect of the lq. He tank is a reduced temperature of the surrounded trap to 4.2 K, which in return helps to maintain a ultra-high-vacuum (UHV) [118]. A good vacuum reduces interactions with residual gases, notably by charge exchange, which is critical in the production and storage of HCIs. Producing HCIs in an EBIT works by collision ionization between the electron beam and an injected atomic beam. These ions are radially confined by the same magnetic field that guides the electron beam, as well as the negative potential arising from the beam electrons. To stop the ions of escaping axially, the trap contains nine electrodes along the beam path, known as drift tubes. A scheme of this drift tube setup is shown in Fig. 3.3. The voltages of each electrode is adjusted in ascending order towards the trap center, which is set to a lower voltage, and by doing so, a trapping potential is formed by the electric fields. Ions outside the central trapping region are accelerated outwards and thus removed

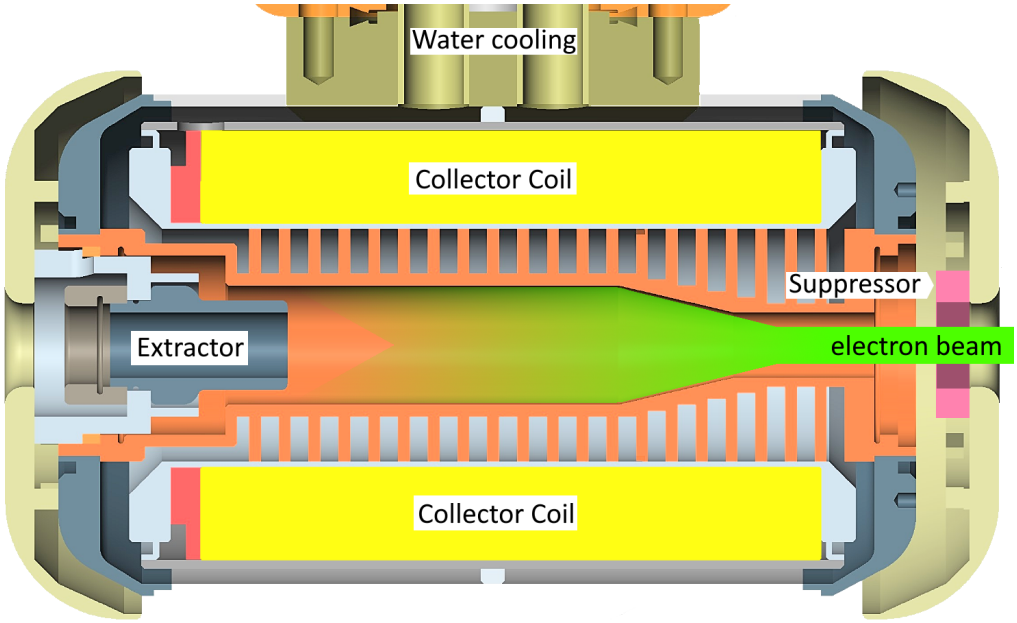

Figure 3.4: The electron collector of the HD-EBIT. The incoming electron beam is stopped by an extractor electrode and is further dispersed by the collector coil.

from the trap. Adjusting the form of this electric trapping potential can be used to reduce the Doppler broadening. For this, the central trap potential can be adjusted in its electrical depth. While a deeper trap would capture more ions and thus increase the collective light, it would trap faster and slower ions alike, leading to a wider Doppler broadening. A shallower trap would let the faster ions escape, reducing the total amount of light going into the spectrometer but increasing the resolution. Furthermore, ions of tungsten and barium are byproducts of the operation of the electron gun and slowly accumulate inside the trap. Lighter injected elements would be pushed out over time. By inverting the trapping potential temporarily, all ions in the trap are removed. Afterwards, the injected atoms fill the trap more quickly and thus form the majority of the trapped ions momentarily. For elements such as Ca and Xe, this dumping process was done every 60 s to 120 s for 2 s. Heavier elements like Bi, or similar, benefit from a slower dumping process of about every 600 s for 5 s.

3.1.3 Collector

The electron beam, guided by the magnetic field through the trap, ends in the collector. A cross-section of the collector can be seen in Fig 3.4. To stop the primary electrons from escaping the collector, an electric field is applied by a highly negative extractor cathode, which is typically set to 2 kV, exceeding the cathode voltage. To stop secondary electrons from being reflected back into the trap, a suppressor cathode is used to generate an electric field with a voltage of −200 V. The power of the incoming electrons will generate a significant amount of heat when stopped,

and could cause damage to the system if they hit a single spot. A coil is used to scatter and distribute the electron beam across the collector. This coil is typically operated with 2.29 V and 76.6 A. The resulting heat is removed from the system by water cooling. To achieve an electrically closed system, the collector and the gun share a common electrical ground separated only by a large resistor. This allows a collector current to be measured and the number of electrons in the beam to be inferred. Currents measured in the suppressor electrode serves as a gauge for how well the beam is passing through the system.

While these currents help to determine if the beam reaches the collector, small position adjustments of the gun are still needed to optimize for any spiraling motion of the beam, which would lead to a reduction of produced ions and thus light in the spectrometer. A typical optimization procedure includes adjusting the horizontal or vertical positioning of the gun by a few micrometers and a consecutive spectrometer measurement. The measured intensity from the ions is put into perspective with the positional change of the gun and the procedure is repeated until the signal has been optimized.

To improve spectral line resolution, the measured collector current is used as a gauge. A reduction of the current, i.e. fewer electrons in the beam, leads to reduced collisions between the electrons and the ions. This reduction leads to a decreased acceleration of the trapped ions, which in turn reduces the Doppler broadening at the cost of fewer ions.

3.1.4 Injection system

To inject atoms into the trap of the EBIT, a gas injection system is used in which gas traverses a two-stage pump system to provide an inflow into the UHV trap of a few million atoms per second. Fig. 3.5 depicts a scheme of the injection system. Via a needle valve, injected gas enters the two-stage system, where each stage has its own turbopump. A small aperture (AP1) separates the two stages, causing a pressure difference of about one order of magnitude. Between the second stage and the trap region, two additional apertures on the heat shields (AP2 and AP3) ensure that only a small fraction of the gas enters the EBITs trap region to maintain the UHV.

If an element does not exist in a gaseous form, it often can be found bound in an organo-metallic compound. Such a compound needs to be vaporized for injection. This can be achieved by the vacuum itself, thus reducing the evaporation or sublimation temperature, or by additionally heating the compound. Occasionally, the vaporization process is slow and it may be necessary to remove the needle valve as it may hinder the injection, for example, when a compound is denatured and yields insufficient gas.

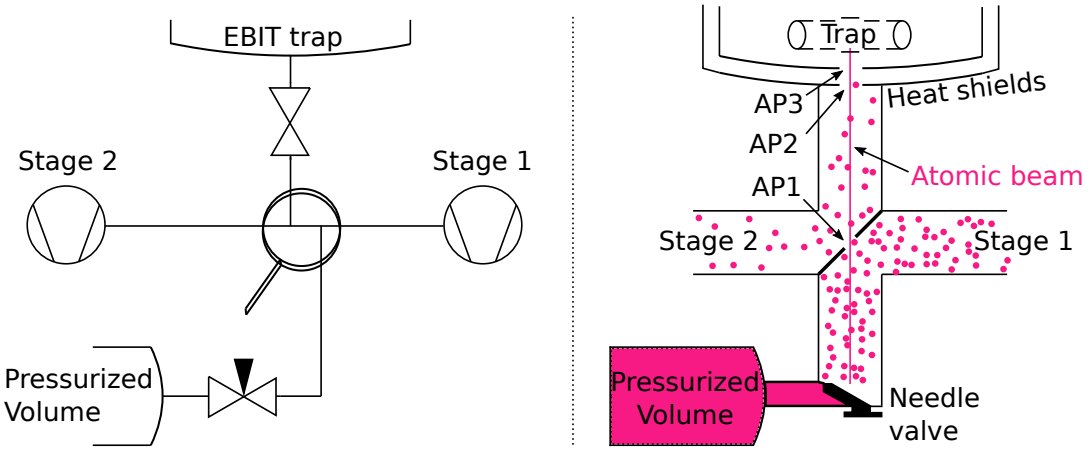

Figure 3.5: Setup of the injection system. A small aperture (AP1) separates the two injection stages to reduce the pressure. Two additional apertures (AP2, AP3) further reduce the pressure to the vacuum level of the EBIT trap.

To inject radioactive elements which practically cannot be bound in a organo-metallic compound, a laser ablation system will be an addition to the experimental setup. For such a system, the ablation laser light enters from above through a window, where it is collimated and refocused onto the target which will be placed in close proximity to the electron beam. The target itself is precisely positioned by a 600 mm x-y-z stage from the other end of the setup. A wire allows the target to be set to the central drift tube voltage to not disturb the electric field and thus the electron beam. Once the EBIT-Dewar is filled with lq. He, the trap temperature is at 4.2 K, and any heat transfer will negatively impact the trap and increase lq. He evaporation. Therefore, thermal conductivity is kept to a minimum by only a single connecting wire and an insulated target holder. Perfect alignment of the laser beam onto the target holder is ascertained by an external camera. This system is currently being installed for upcoming measurements. These include californium, a clock candidate, and thorium, a nuclear transition candidate.

3.1.5 Electron beam

To understand the ionization process, the properties of the electron beam have to be understood.

As seen in Eq. 2.49, the radial extent of the beam can be expressed as the Brillouin radius. However, this equation does not consider the magnetic field at the cathode B_c, nor the radius r_c or temperature T_c of the cathode. To account for these effects, the Herrmann approximation [125] can be used

$$r_{\mathrm{H}} = r_{\mathrm{B}} \sqrt{\frac{1}{2} + \sqrt{\frac{1}{4} + \frac{8 m_{\mathrm{e}} k_{\mathrm{B}} T_c r_c^2}{e^2 B^2 r_{\mathrm{B}}^4} + \frac{B_c^2 r_c^4}{B^2 r_{\mathrm{B}}^4}}} \,, \tag{3.1}$$

which results in beam radii in the range of about 20 μm to 200 μm [119], strongly depending the magnetic field B_c at the cathode. As derived in Eq. 2.52, the potential caused by the electrons in the center of the trap $\Phi_{\text{inner}}(r = 0)$, which is also known as the space charge Φ_{sc}, changes with the Herrmann radius to

$$\Phi_{\text{sc}} = \Phi_{\text{inner}}(r) = \frac{I}{2\pi\epsilon_0\sqrt{2eU_c/m_e}\pi r_H^2}\left(\frac{r^2}{r_H^2} - \frac{1}{2} - \ln\frac{r_H}{r_{\text{trap}}}\right), \tag{3.2}$$

in which the larger radius by Herrmann over Brillouin spreads the space charge across a larger volume, and the outer radius is set by the trap size r_{trap}. Acceleration of the beam and subsequently its energy is expressed as the sum of all potentials,

$$E_{\text{beam}} = e(U_c + U_{\text{trap}} - \Phi_{\text{sc}}), \tag{3.3}$$

including the positive potential of the central drift tube U_{trap}.

It is reasonable to assume that the beam goes straight through the center of the EBIT if it was optimized correctly. However, a slightly off-axis beam may experience instabilities considering the electric and magnetic fields present at all stages of the EBIT. The main force affecting the electrons in the beam and the trapped ions is the Lorentz force

$$F_{\text{Lorentz}} = q(E + v \times B). \tag{3.4}$$

The EBIT is designed so that the electrons with velocity v are moving along B, thus only experiencing the force from the potential difference between gun cathode and trap center. The electrical field by the drift tubes also do not exert a force onto a central beam due to the cylindrical symmetry. To center the beam, the gun is adjustable in its position in all directions with micrometer precision. A deviation from the central axis would give v a perpendicular velocity $v_\perp$ relative to the magnetic field. The velocity $v_\perp$ results in a force according to Eq. 3.4, which leads to a constriction of the beam for small $v_\perp$, but a larger deviation causes the beam to perform a spiral motion around the central axis. This motion lowers the effective ionization and leads to a reduced number of trapped ions and with it a lower signal in the detector of the spectrometer. A beam closer to one side of the drift tubes further increases this motion through the electric field E. Furthermore, the dumping process, every 60 s, temporarily increases the potential of the central electrode by a few hundred Volts. This change of the electric field causes another force onto an off-axis electron beam, according to Maxwell's equations. This may result in a sudden change in the beam's path, and therefore a change in the measured currents, which is direct evidence that the beam requires further optimization.

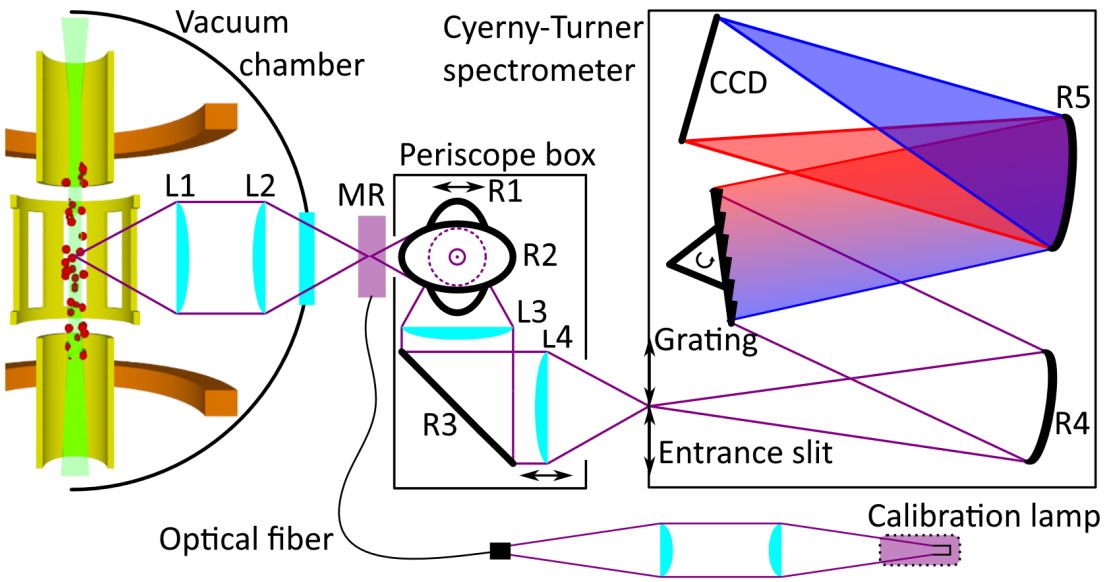

Figure 3.6: Optical spectroscopy setup at the HD-EBIT. Horizontal light from the EBIT is directed and refocused on the entrance slit of a 2 m Czerny-Turner spectrometer. A movable reflector (MR) allows temporary insertion of calibration light. See text for details. Originally from [126], adapted from [119].

3.2 Czerny-Turner spectrometer

The optical setup at the HD-EBIT is depicted in Fig. 3.6. Here, light emitted by trapped ions in the EBIT leaves the vacuum chamber via two lenses (L1 and L2) built into the heat shields inside the vacuum chamber. Their diameter is 25.4 mm and their focal length is 150 mm. Unfortunately, for their placement in the vacuum chamber, only single lenses could be used, making the setup chromatic, which means a different focal point for every wavelength. To maximize the light entering the spectrometer's vertical entrance slit, the light from the horizontally trapped ions is turned vertically by three mirrors (R1, R2, and R3) in the periscope box. Mirror R1 is positioned on a linear stage to align the light-stripe with the entrance slit, while the light is refocused on it by lenses L3 and L4. Additionally, L4 is placed on an automated linear stage to correct for the wavelength-dependent focal point. A movable reflector (MR) can be automatically raised to allow light from a calibration lamp to traverse along the same optical path as the light from the EBIT. This is used to compensate for any setup imperfections and to obtain the dispersion function. All these lenses are made from fused silica and all the mirrors have an UV-enhanced Al coating, which provides a good efficiency for wavelengths between 200 and 800 nm.

The effective attenuation of the both angles of polarization of an M1 emission can be estimated by the descriptor of reflection with s- and p-polarization as introduced in chapter 2.1.4. In all mirrors, except R2, the π component is seen as p-polarized, while σ is s-polarized. A reflection of 45° allows the s-polarization a greater reflectivity than

Table 3.1: Gratings for the spectrometer McPherson Model 2062. Values taken from Ref. [127].

Grating ($^{gr.}/_{mm}$)	Main wavelength (nm)	Dispersion ($^{nm}/_{mm}$)	Bandwidth
150	500	3.32	91.6 nm
1800	400-800 (holographic)	0.26	7.2 nm
3600	200-400 (holographic)	0.14	3.9 nm

p-polarization [88], resulting in a reduced amplitude of the π component, compared to the σ components. Furthermore, the used gratings further lower the intensity of the π component for wavelengths $\gtrsim 500\,\text{nm}$ [114] (see chapter 2.5). Below this wavelength, the effect becomes too unpredictable and a generalization is not possible.

3.2.1 Spectrometer and gratings

The spectrometer is a 2 m McPherson Model 2062 [127] Czerny-Turner spectrometer with three available gratings. These are listed in Tab. 3.1. A finer grating means higher resolution, as seen from Eq. 2.56. The specified blazing angle promotes reflection efficiency. The 150 grooves/mm grating is blazed at 500 nm, which yields highest efficiency for observed light of such wavelength. Interference angles of other wavelengths will lead to a loss of efficiency (see chapter 2.5.1). The lower limit of the 150 grating has been experimentally identified at $\approx 310\,\text{nm}$. This wavelength corresponds to an angle where the efficiency of the grating is minuscule. This also results in a more intense second order of a transition than its first order below this threshold. The other two gratings are holographic gratings, which instead have smooth edges that allow an efficient interference of a wider range of wavelengths (see Fig. 2.11 c).

These gratings allow observation of strong lines down to 240 nm without purging the optical setup from air with nitrogen to counter the absorbance of the air. Note that the dispersion listed in Tab. 3.1 is merely an approximation from the datasheet, however, it serves as a starting point for finding the local dispersion function based on the calibration lamp.

As discussed before, the reflectivity of the mirrors are polarization-dependent and lead to a different intensity for the π and σ components of the Zeeman splitting. However, gratings also have a strong dependence on the polarization of the light for the reflectivity. This increases the difference in amplitude between the π and σ lines depending on the wavelength and grating used. While a fit of the Zeeman structure can account for this difference, if the actual π/σ ratio is required, it is necessary to consider these effects carefully.

The entrance slit can be varied between 5 mm and 10 μm. While a smaller entrance slit generally enhances the resolution, a slit causing a light-cone smaller than the spectroscopy mirror R4 will only limit the intensity without gaining resolution. This is because there is less coverage of the grating, which reduces its effectiveness. By using a flashlight in front of the entrance slit, it was found that a minimum slit width of 40 μm was sufficient to illuminate the entirety of the collimating mirror in the spectrometer (see Fig. 3.6, mirror R4).

A motor rotates the grating and sets the spectrometer to the specified wavelength. An analog dial on the spectrometer can be used to manually confirm the positioning. As introduced in chapter 2.5.1, the constructive interference wavelength depends on the angle and the groove density. A different grating has a different relation between the angle and the wavelength, as seen in Eq. 2.56. This can be toggled in the control software, which adjusts the motor accordingly. While the grating can cover a wide range, its rotation is physically limited by the motorized thread, which is only as long as the width of the spectrometer. The grating can be manually rotated a bit further to utilize the gratings efficiency at higher wavelengths. This overcomes the limitation posed by the thread and extends the wavelength range. This so-called *extended mode* increases the range of the 3600 grating from maximal 400 nm to 450 nm, and for the 1800 grating from 840 nm to 1030 nm. This extension can be important for highest precision measurements, as changing from the 3600 to the 1800 grating would reduce the resolution by a factor of two. Similarly, going up to 1000 nm with the 1800 grating can be advantageous. While the wavelength efficiency drops for the used CCD camera for such high λ, it can be used for measuring a higher-order of a transition of a lower wavelength.

3.2.2 CCD camera

At the other end of the spectrometer is an Oxford Instruments Newton DU940P-BU2 CCD camera [128] cooled to -80°C. The cooling is essential to reduce thermal noise to measure weak lines from the EBIT trap. The camera counts $P_x \times P_y = (2048 \times 512)$ px, with 13.5 μm pixel size, resulting in a $27.6 \times 6.9\,\mathrm{mm}^2$ detection area. Thermal noise is specified at $0.0003\,\mathrm{e}^-/\mathrm{px/s}$ at a temperature of −80°C, which is the lowest possible temperature given the connected cooling water temperature. The typical readout noise is specified as 11 e^-. [128]

By combining these, the total noise per exposure time τ can be calculated

$$\Delta I = \mathrm{readout} \cdot \frac{P_x}{b_x}\frac{P_y}{b_y} + \mathrm{thermal} \cdot P_x \cdot P_y \cdot \tau. \tag{3.5}$$

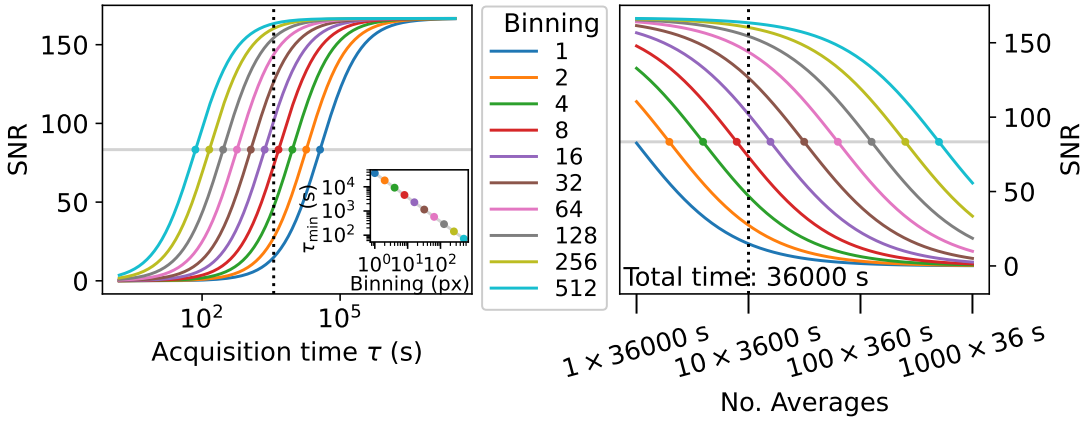

Figure 3.7: Signal-to-noise-ratio (SNR) for different binning of the vertical pixels (color coded). Left: SNR for different acquisition times, dots mark the $\tau_{\min}$ value, the inset shows its relation with the binning. The dotted line marks 1 h. Right: SNR for a given total time of 10 h with different averages.

Here, P_x and P_y are the horizontal and vertical pixels of the CCD chip, and b_x and b_y are the binning in each of these axes. With the known parameters inserted, the equation is

$$\Delta I = 11\,\mathrm{e}^- \cdot \frac{(2048 \times 512)\,\mathrm{px}}{b_x \cdot b_y} + 0.0003 \frac{\mathrm{e}^-}{\mathrm{px}\,s} \cdot (2048 \times 512)\,\mathrm{px} \cdot \tau.$$

Because the wavelengths are dispersed along the x-axis, binning x-pixels would not be beneficial, as it would lead to a loss of resolution. The quotient of the two noise contributions, i.e. of when both noise contributions become equal, is

$$\tau_{\min} \cdot b_y = \frac{\text{readout}}{\text{thermal}} = \frac{11\,\mathrm{e}^-}{0.0003 \frac{\mathrm{e}^-}{\mathrm{px}\,s}} = 36666.667\,\mathrm{px} \cdot \mathrm{s}, \tag{3.6}$$

which results in the time $\tau_{\min}$ needed for the thermal noise to become the dominant noise term. No binning in y would make the noises equal at $\tau_{\min} = 10\,\mathrm{h}$, whereas if all the vertical pixels are binned together ($b_y = 512\,\mathrm{px}$), the time is reduced to $\tau_{\min} = 1\,\mathrm{min}$. The signal-to-noise ratio (SNR) can be expressed as

$$\mathrm{SNR} = \frac{I}{\Delta I} = \frac{\text{signal} \cdot (100 \times 512)\,\mathrm{px} \cdot \tau}{11\,\mathrm{e}^- \cdot \frac{(2048 \times 512)\,\mathrm{px}}{b_y} + 0.0003 \frac{\mathrm{e}^-}{\mathrm{px}\,s} \cdot (2048 \times 512)\,\mathrm{px} \cdot \tau}. \tag{3.7}$$

Here, the signal spans all vertical pixels and 100 px along the horizontal detector axis. It scales linearly with time τ.

A visualization of Eq. 3.7 is shown in Fig. 3.7. Here, SNR for a varying acquisition time for different binning b_y is shown. The time $\tau_{\min}$ is marked with a dot for each

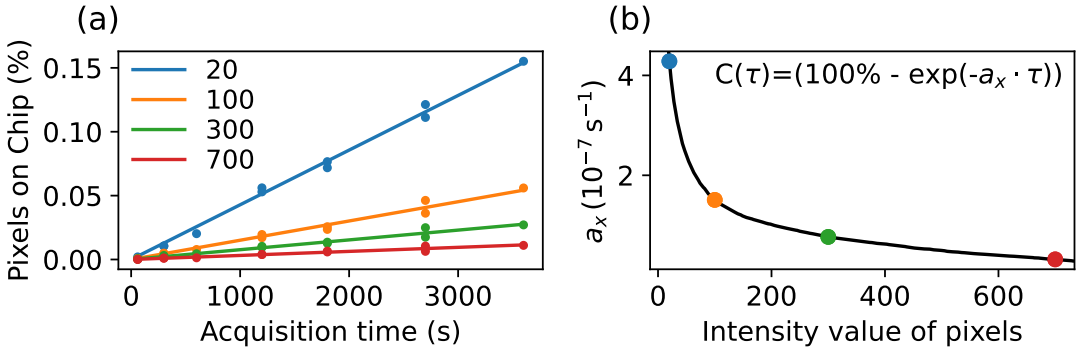

Figure 3.8: (a) Percentage of camera chip covered by cosmics for intensity thresholds of 20, 100, 300 and 700. An exponential fit was fitted through the points. (b) Occurrence rate parameter a_x for the different intensity thresholds.

binning. Acquisition times under this mark are dominated by the readout noise, while the thermal noise is more present when above the mark. At high τ, the SNR becomes constant, as the readout noise part becomes negligible and the τ dependencies cancel out. A lower binning requires a longer acquisition time to achieve a comparable SNR. On the right of Fig. 3.7, the effect of averaging is shown for a fixed total acquisition time of 10 h. An increasing number of averages lowers the SNR due to the added readout noise for every average and the reduced acquisition time. The acquisition time of 1 h is marked in both plots as a reference, for which the binning should be $b_y = 512\,\text{px}$ at all times. While a high binning leads to better SNR, external influences can be a limiting factor, e.g. atmospheric changes and high energy particles. The latter hit the earth's atmosphere, which lead to a shower of different particles. These are mostly electrons, protons, pions, neutrons and muons, which usually occur in this exact order [129, 130]. These will be referred to as *cosmics* from now on. The total amount of cosmics is determined by the height above sea level, but this may increase given the experiments around the HD-EBIT. Their interaction with the camera chip will result in a strong, but very local, signal limited to a few pixels.

To evaluate the number of cosmics and their intensities on the camera chip, a few dark-images were taken with different exposure times τ ranging from 60 s to 3600 s. These images were taken without binning to evaluate the whole chip. The number of pixels that exceed a given intensity are shown in Fig. 3.8 (a). A lower intensity threshold naturally leads to a higher number. A simple exponential function [130] was fitted through each of the thresholds

$$C(\tau) = 100\% - \exp\left(-a_x \cdot \tau\right). \tag{3.8}$$

This function represents the percentage of the camera chip which experienced a cosmic event of a given amplitude threshold. Its resulting fit parameter a_x can be

Table 3.2: Exponential parameters a_x for the rate of an cosmic event occurring with a given intensity threshold.

Intensity	a_x (s^{-1})
20	4.28×10^{-7}
100	1.51×10^{-7}
300	0.767×10^{-7}
700	0.317×10^{-7}

expressed for each threshold value as shown in Fig. 3.8 (b). Some key parameters are listed in Tab. 3.2. Therefore, given this parameter, the statistical time it takes to fill the camera chip to a certain extent can be calculated. The inverse function is

$$\tau = -\frac{\ln(100\% - C)}{a_x}. \tag{3.9}$$

For example, to estimate when $C = 50\%$ of the detector has experienced a cosmic event of intensities over 300, the associated parameter of $a_{300} = 0.767 \times 10^{-7}\,s^{-1}$ is used, which results in a time of $\tau = 104.6\,d$. Evidently, this is an absurd exposure time to use for spectroscopy. However, when binning the pixels, the rate a_x parameter will scale with the binning $a'_x = a_x \cdot b_y$. An explanation is that a hit on an individual pixel counts as a hit on the binned pixel, which doubles the rate for every event. A binning of $b_y = 2$ would lead to a 75% coverage of the detector in equal acquisition time. In this case, where all vertical y-axis pixels were binned together, a time of $\tau = 4.9\,h$ fills half of the detector with cosmics. This would hide potential signals, thus rendering analysis impossible. Cosmics with intensities of 100 or more are even more present, filling half the detector with its $a_{100} = 1.51 \times 10^{-7}\,s^{-1}$ in $\tau = 2.5\,h$ at full binning. A optimal value to settle for is a binning of 16 px, which reduces the 512 px to 32 px. This allows picking out strong cosmics with ease and weaker cosmics can still be removed without substantially interfering with the signal. In this case, cosmics with more than 20 intensity only occupy 20% of the detector within 9 hours of continuous measurement.

While high binning initially seems beneficial, a single cosmic event, or a broken pixel, can be highly disruptive for the acquired image. This is shown in Fig. 3.9, where the Eq. 3.7 is changed to include the effects of the cosmics on the signal-noise ratio. The strong cosmics effectively reduce the number of pixel used. To achieve this, C from Eq. 3.8 is calculated for each time τ and $a_x = a_{25}$ and their percentage is subtracted from the total pixel count. Intensities between 10 and 25 are counted towards the noise with their respective probability: $\sum_{i=10}^{25} i \cdot (C(a_i \cdot b_y, \tau) - C(a_{i+1} \cdot b_y, \tau))$, and intensities lower than 10 are seen as accounted for by thermal and readout noises. In comparison to Fig. 3.7, each binning now has a peak time before the cosmics

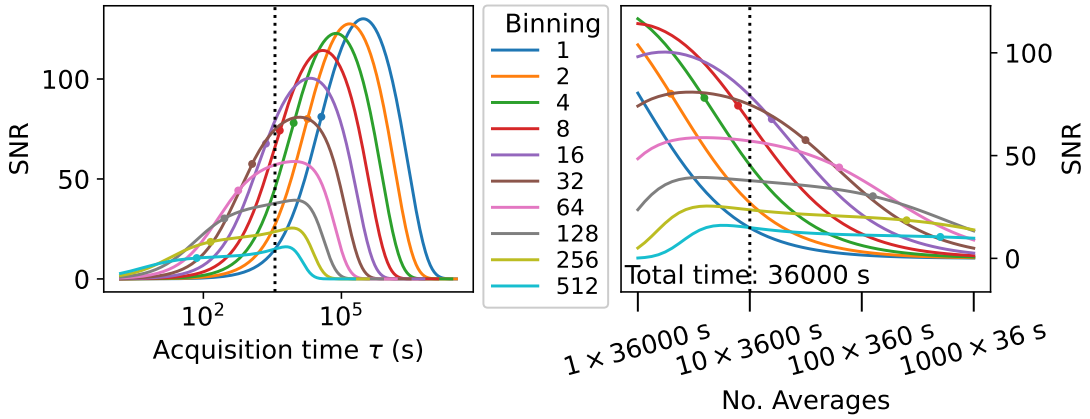

Figure 3.9: Signal-noise ratio including the effects of cosmics. Left: for different acquisition times, right: for different number of averages.

overwhelm the signal. This result disputes the previous assessment that the highest possible binning is the best option. Depending on the acquisition time, a different binning is ideal. It is still advantageous to measure for as long as possible, however, there is an additional limiting factor of atmospheric influences, such as temperature, on the setup. These influences would cause a slight change in the spectrometer size, as well as in the position of lenses and mirrors, effectively inducing a shift in the spectrum. To avoid this, it is recommended to not exceed two hours of continuous recording, as otherwise the lines would be heavily skewed, and thus reducing resolution. In this regard, the ideal binning for that time frame is 16 pixels.

Chapter 4

Measurement

Calcium and xenon are elements with a large number of stable isotopes without nuclear spin. Calcium has five such isotopes: 40, 42, 44, 46, and 48; and xenon has seven: 124, 126, 128, 130, 132, 134, and 136. These are highly favourable for IS studies and the KP method, and will be theoretically analyzed in chapter 5. Before studying these IS, groundwork needs to be laid out, which requires fluorescence spectroscopy. Optical transitions above $A_{\mathrm{ki}} \approx 10\,\mathrm{s}^{-1}$ can be precisely measured with the optical spectroscopy setup with down to 10^{-7} fractional uncertainty.

In the following chapter, the EBIT and image optimization processes are explained, followed by the spectroscopy results for calcium and xenon.

4.1 Resolution improvement

There are fewer optical lines as the transitions shift with increasing charge states to higher energies. For this reason, only spectra up to a cathode voltage of 2500 V are investigated. As mentioned before, the signal resolution can be improved with settings of the EBIT. There are three main means to do so: beam current adjustment, trap depth adjustment, and buffer gas injection.

Beam current The beam current can be reduced by lowering the voltage of the focus electrode. This causes fewer electrons to leave the cathode and reduces the electron density in the beam, which will excite a smaller amount of the inserted ions. However, the subsequent reduced amount of collisions of electrons with the atoms will narrow the Doppler broadening of the linewidth. This is shown in Fig. 4.1, where the same transition was measured at different collector currents, causing a subsequent reduction of the standard deviation σ of the Zeeman components. The lowest currents achieved in this work are 5 mA.

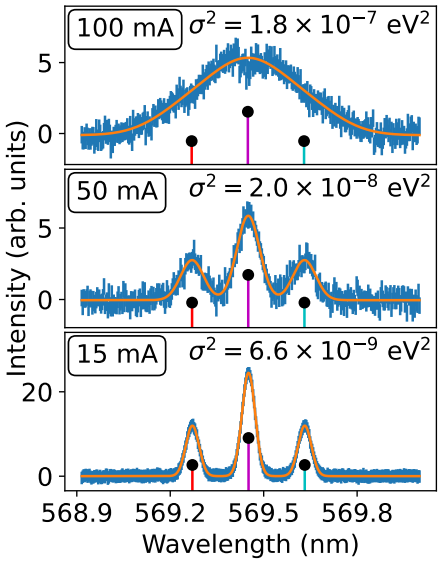

Figure 4.1: Effect of the beam currents on the linewidth. Example measured on the $^3P_1 - ^3P_0$ ground-state transition of Ca^{14+}.

Trap depth A reduction of the trapping potentials by the drift tubes can improve resolution as well. A shallow trap allows fast ions to escape while retaining the slow ions. This also reduces the overall intensity but effectively reduces the Doppler effect in the spectral line. This advantage is more evident in heavy ions, where a slight inversion of the trap can be used to retain only the slowest ions, which cannot escape quickly due to their high inertia and low momenta.

Buffer elements A third option to improve resolution is to additionally inject a lighter gas (e.g. neon), which would buffer the energy of the heavier injected ions and thus reduce the temperature of the ions of interest. In principle, a collision event will transfer momentum from the heavy ion to the light ion, which is then forced out of the trap. Moreover, the buffer gas can be an advantageous byproduct of the injection of e.g. organo-metallic compounds. Here, the compound C and H atoms will leave the trap, taking the energy of the heavier ions with them. [131]

4.2 Image preparation and optimization

4.2.1 Image correction

Cosmic particles The interference of cosmic particles with the detector was previously discussed in chapter 3.2.2. These events are energetic, but highly localized. Thus, removing a few strong cosmics is relatively simple and could be performed manually. However, a more reliable method is to use an automated script, as used in Ref. [119], which evaluates the histogram of a small area of e.g. 32×8 px from the camera image for a cosmic event. To avoid accidentally removing any signals from ions, only outliers from the histogram are filtered out.

This procedure is shown in Fig. 4.2 (a) for a dark image of 1 h acquisition time without binning. A red box marks the small area that is subject to the evaluation. The intensities of its pixels are sorted into a histogram, which is shown as an inset plot. To separate the real image and the cosmics, the histogram is evaluated in terms of the number of consecutive empty bins. If the number of empty bins is grater than

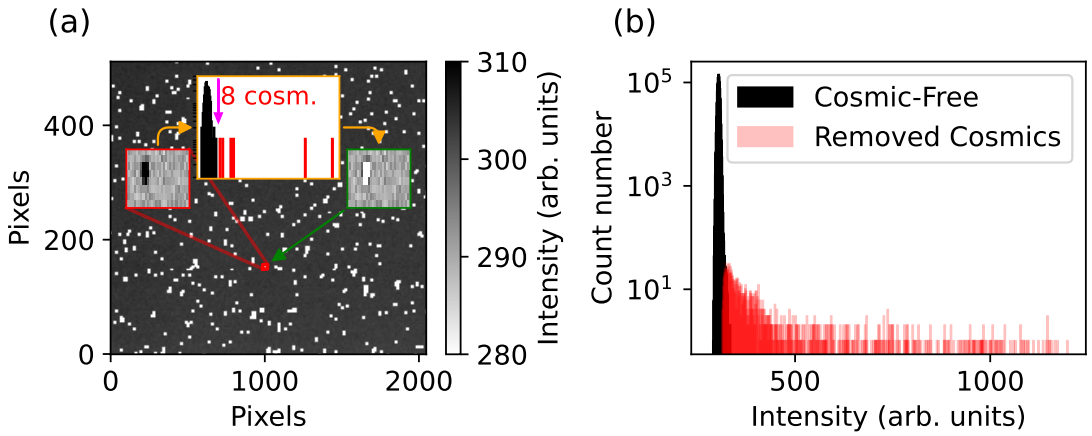

Figure 4.2: (a) Removal of cosmics based on histograms taken from small sub-figures, where the magenta arrow is placed on three consecutive bins, marking the cut-off point. (b) Histogram of the entire image before and after removal of the cosmics in red.

a chosen factor of the histogram's standard deviation, then this marks the separation point. In this case, a gap of three bins separates the images from the outliers for that small area. This separation point is marked in the inset histogram by a magenta arrow. The removed pixels are then replaced by not-a-number (NaN) values which will then be ignored in the consecutive image optimization process. This is repeated until the entire image is divided into small areas, which are then investigated and cleared of cosmics.

In Fig. 4.2 (b) the histogram of the total image is shown. The black bars represent the cosmic-corrected image, while the red bars show the removed cosmics. In this example, a total of 1612 px were removed using this method. This number is in agreement with the expected occurrence of cosmics from chapter 3.2.2, Eq 3.8 and Tab. 3.2, where 1614 px are expected to contain cosmics with intensities above 20.

Signal curvature At the end of chapter 3.2.2 the changing of materials due to temperature and its shifting effect on the measurement has been contemplated. Additionally, the signal may contain a slight curvature caused by lenses and parabolic mirrors.

To counter both effects, a 2D Gaussian shape is fitted to the brightest calibration lines

$$I(x,y) = A \cdot \exp\left(-\left(\frac{x-(m\cdot(y-y_0)^2+b\cdot(y-y_0)+c)}{\sigma_x}\right)^2-\left(\frac{y-y_0}{\sigma_y}\right)^2\right)+d. \quad (4.1)$$

The fit is done for all the bright calibration lines $I_{\text{total}} = \sum_i I_i(x,y)$. The curvature of the lines is described by a quadratic polynomial $m\cdot(y-y_0)^2+b\cdot(y-y_0)+c$. Its

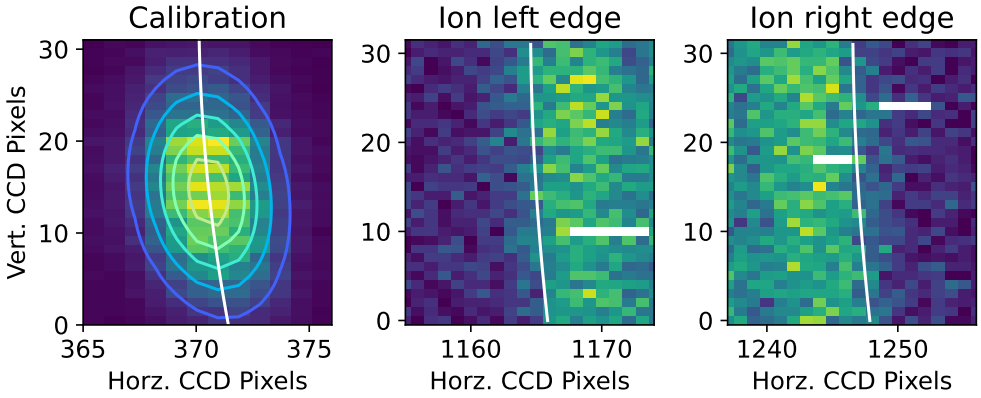

Figure 4.3: Curvature effect seen in calibration and ion image. Left: Zoom into one example calibration line where the 2D-Gaussian function (Eq. 4.1) was fitted to. The white line is the resulting quadratic polynomial from that function. Middle and right: Each side of the ion spectral line with the same polynomial function plotted.

component c is the center position of the calibration line, which yields the temperature shift for each of the fitted calibration lines when compared to the position of the same lines in the other images.

Fig. 4.3 shows this fit in the example of a single calibration line. The contour lines are from the 2D-Gaussian fit, and the white line is the quadratic polynomial describing the shift of the center position over the vertical axis of the camera. The same polynomial was drawn into the left and right edges of the ion line. It can be seen to match the curvature, proving the correctness of the fit and that it is not an effect solely from the calibration lines. The curvature effect can be explained by the parabolic mirrors inside the spectrometer. A possible curvature caused by the lenses before the spectrometer can be ruled out due to the narrow entrance slit.

On another note, it can be seen that the calibration line does not completely fill the camera due to the point source which is scattered off a diffusor (see chapter 3.2) which follows a Gaussian distribution. The ion line, on the other hand, has a uniform distribution along the vertical axis due to the trapped ions in an elongated trap.

Temperature shift As previously mentioned, there is an observable shift caused by the temperature. This shift can be extracted directly from the performed curvature correction Eq. 4.1 as the parameter c. The air conditioning installed at the HD-EBIT compensates for the largest temperature shifts in the room, however, small day/night differences still cause a slight change in temperature. This has an influence on the optical setup between the HD-EBIT and the spectrometer. A small shift in the line position over the day has occurred before [119]. The same effect was observed again and visualized in Fig. 4.4 where the calibration line positions were measured over a 24 h interval. The initial external temperature was 31°C in the afternoon,

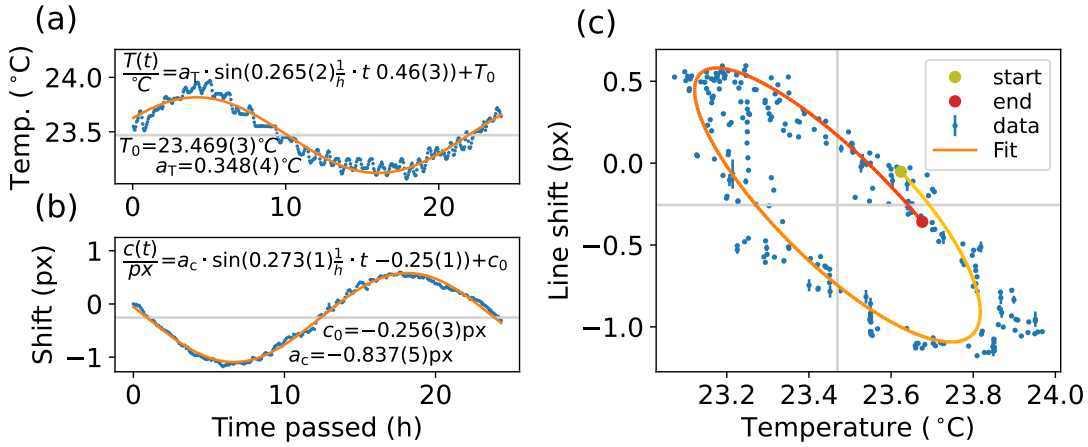

Figure 4.4: Temperature influences on line position on detector. (a) Temperature log over 24 h. Fluctuations were caused by air conditioning. (b) Line position on CCD over 24 h. (c) Lissajous figure from both sinusoidal behaviors. The gray lines represent the offset position of the fitted sinusoidal functions.

which peaked in the evening at 34°C and dropped to a low of 19°C in the following morning. This was reflected in the logged internal temperatures (a) at the HD-EBIT. The smaller fluctuations in the data were due to the air conditioning turning on and off. Multiple 5-minute measurements on calibration lines with the 1800 gr./mm grating were performed in direct succession. Their position (b) shifted with the temperature, but with a slight delay. The small but more attenuated effects of the air conditioning unit were also observed. Both data were fitted with a sinusoidal function $x(t) = a \cdot \sin(f \cdot t + \phi) + x_0$, and the parameters of the amplitude a, frequency f for the time t [h], phase ϕ and the offset x_0 are included in the figure. The delay between the temperature and the shift was also observed in the constructed Lissajous figure (c), whose oval shape was a direct consequence of this delay. The color-coded line represents the direction in which the data was obtained, representing the total phase difference of $\phi = -221(2)°$. The phase shift, without the 180° due to the different signs in temperature and line shift, was $\phi = 41(2)°$, and represents a time delay of $\Delta t = \phi/f = 2.7(2)$ h. The materials in the optical setup, including stages, lens and mirror holders, as well as the whole spectrometer, were slowly affected by the temperature change. This delay was due to 1) its thermal conductivity, and 2) its encasing, which lowers the speed of the heat exchange. Considering the 2 m length of the spectrometer, a temperature shift of 1°C, as seen in the temperature measurement, would lead to a shift of 45 μm in its length [132]. Further consideration of the angles between the mirrors and the grating [127] would lead to a spectral line shift on the detector of 11.25 μm. Given the CCD pixel size of 13.5 μm, this would mean a shift of 0.83 px, which is consistent with the observation.

The positional shift can be converted into a wavelength shift for a given grating. In the example of the 1800 gr./mm grating and its dispersion of 0.26 nm/mm (see Tab. 3.1), the shift between two time points t_0 and t_1 is calculated by

$$\delta\lambda = D\frac{l_x}{P_x} \cdot (c(t_1) - c(t_0)) = 0.26\,\frac{\text{nm}}{\text{mm}} \cdot \frac{26.7\,\text{mm}}{2048\,\text{px}} \cdot (c(t_1) - c(t_0)), \tag{4.2}$$

with dispersion D, horizontal detector length l_x and pixels P_x, and shift function $c(t)$. An acquisition time of 1 hour would lead to a wavelength shift of 0.00005 nm at the sinusoidal peak, and of up to 0.00077 nm at the starkest change. A shortened acquisition time of 30 minutes reduces this range to 0.00001 nm and 0.00039 nm respectively, while a longer acquisition time of 2 hours would lead to bigger shifts between 0.00016 nm and 0.00129 nm. Continuous acquisition of e.g. 5 hours would result in up to 0.00358 nm uncertainty due to this temperate shift. These positional shifts are more pronounced because of stronger temperature shifts on this day. Days with less pronounced temperature changes would result in a smaller line shift. It is unlikely that shifts would normally exceed this measured shift. To contrast this with the SNR analysis in chapter 3.2.2, where the 1 h acquisition time is marked with a dotted line in Fig. 3.9, the highest SNR is achieved at a binning of $b_y = 16\,\text{px}$ for such an acquisition time.

4.2.2 Dispersion function

The above image corrections were applied to achieve an accurate projected image. To ultimately obtain absolute values for the wavelength of the measured ions, the pixel-wavelength relation was evaluated on the CCD. Hollow cathode lamps of various elements were used as calibration source. The calibration line positions were acquired by a Gaussian fit on the projection image. As these lamps have known lines listed in the NIST database [45], this generated a correspondence between their wavelengths and their pixel positions. The wavelength of each line was plotted over its pixel position on the detector and a polynomial function was fitted through these to obtain a dispersion function, resulting in a pixel-wavelength correlation. This process is visualized in Fig. 4.5, where a Fe-Ar lamp was used. The choice of lamp depends on the number of visible lines for the grating used and the wavelength studied. The polynomial used was of third-order with the following equation

$$\begin{aligned}\lambda(p) =& 1.4(2) \times 10^{-12}\,\frac{\text{nm}}{\text{px}^3} \cdot (p - 1198\,\text{px})^3 - 5.2(1) \times 10^{-9}\,\frac{\text{nm}}{\text{px}^2} \cdot (p - 1198\,\text{px})^2 \\ &+ 3.36053(8) \times 10^{-3}\,\frac{\text{nm}}{\text{px}} \cdot (p - 1198\,\text{px}) + 436.14097(3)\,\text{nm}.\end{aligned}$$

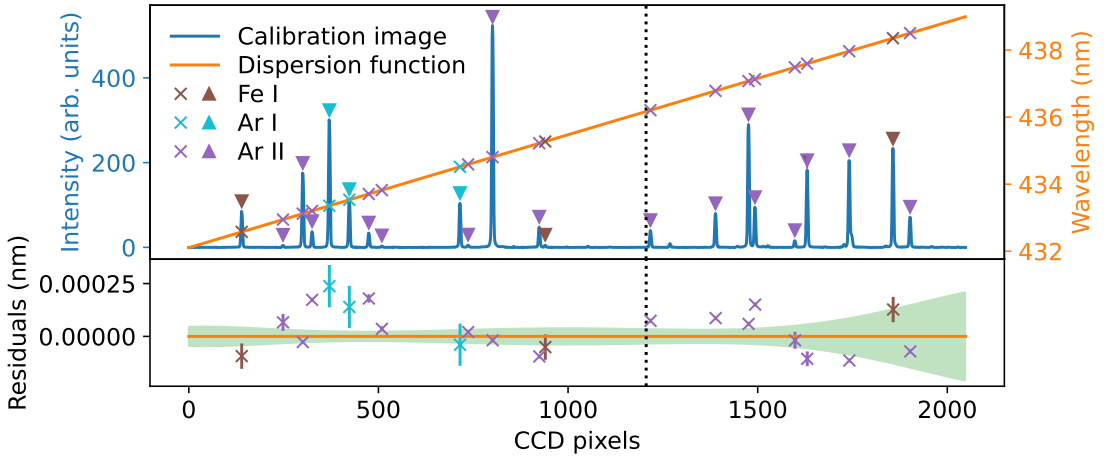

Figure 4.5: Determination of the dispersion function using Xe^{17+} as an example . Top: Spectral lines of a Fe-Ar calibration lamp were identified with their corresponding wavelengths from the NIST database [45]. Their positions on the camera provide a pixel-wavelength relationship. Bottom: Residuals of the calibration lines to the dispersion function. The green band shows the 1-σ confidence band. The dotted line represents the position of the measured Xe^{17+} line.

The function of the wavelength λ at the pixel position p on the detector was evaluated at the position of the investigated line of 1198 px to minimize the uncertainty. However, a third-order polynomial is rather the exception than the norm, as most cases were optimally fitted by a quadratic polynomial function. This shows that it has proven useful to always fit both and to use the better one. Since both pixel and wavelength values have uncertainties, orthogonal distance regression (ODR) [133] was used to fit the polynomial to the data. Essentially, this method attempts to minimize ovals around each point in accordance with the x- and y-uncertainty.

The dispersion function was obtained at various wavelengths for the three gratings over many performed measurements. From the dispersion function above and Fig. 4.5,

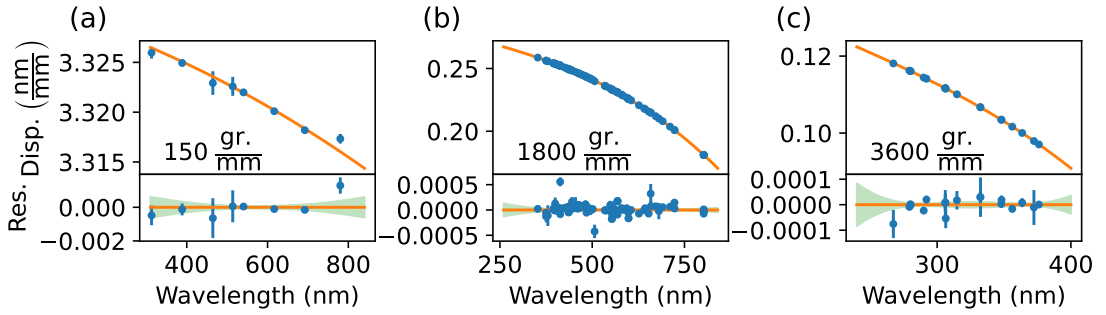

Figure 4.6: Local linear dispersion parameter at different wavelengths for different gratings. Points are based on measurements from the past four years with uncertainties resulting from the applied fit. A polynomial fit was fitted through it, its result is listed in Tab. 4.1.

Table 4.1: Fit parameters through dispersion functions from measurements done in the past four years, according to the formula: $D(\lambda) = a{\cdot}(\lambda{-}\mathrm{k})^3{+}m{\cdot}(\lambda{-}\mathrm{k})^2{+}b{\cdot}(\lambda{-}\mathrm{k}){+}c$. The rightmost column is the dispersion as noted in Ref. [127]. The wavelength evaluation point k was chosen in the middle of the given range of that grating. And was $k = 600\,\mathrm{nm}$ for the 150 and 1800 gratings, and $k = 300\,\mathrm{nm}$ for the 3600 grating.

Grat.	$a\left(\frac{10^{-10}}{\mathrm{nm}^2\cdot\mathrm{mm}}\right)$	$m\left(\frac{10^{-7}}{\mathrm{nm}\cdot\mathrm{mm}}\right)$	$b\left(\frac{10^{-5}}{\mathrm{mm}}\right)$	$c\left(\frac{\mathrm{nm}}{\mathrm{mm}}\right)$	Disp. [127]
150	/	−0.24(3)	− 2.59(6)	3.32053(2)	3.32 $\frac{\mathrm{nm}}{\mathrm{mm}}$
1800	− 1.30(4)	−1.975(4)	− 0.01746(1)	0.255637(2)	0.26 $\frac{\mathrm{nm}}{\mathrm{mm}}$
3600	−12(1)	−3.1(1)	−17.53(2)	0.112719(9)	0.14 $\frac{\mathrm{nm}}{\mathrm{mm}}$

it is clear that the last two terms, i.e. the offset and the linear dispersion term, are the main contributors, and thus can be precisely determined. These two terms plotted against each other can visualize the dispersion function over the whole range of wavelengths. This result can be seen in Fig. 4.6, where each point is from a measurement from the past four years. The dispersion functions were converted from pixels to the physical detector size. Through these points, a polynomial fit was then fitted and the resulting parameters are written in Tab 4.1, where the given parameters were set for a wavelength k within their range. The resulting parameters can be compared to the dispersion from the datasheet [127], as shown in Tab. 3.1. It becomes clear that the given dispersion values are merely taken from one singular wavelength and that the real dispersion ever so slightly depends on the wavelength currently observed.

While these values cannot be used directly to analyze an unknown spectral line, they provide an improved first estimate of the dispersion at the investigated wavelength than the datasheet [127], which will help identify calibration lines with greater ease and quicken the analysis process.

Furthermore, the reduced dispersion at higher wavelengths also corresponds to a reduction of resolution as the components of a transition are slightly closer together. Taking the extremes of the 1800 gr./mm grating, the resolution will decrease from 400 nm to 800 nm by almost 30%.

4.2.3 Fitting of Zeeman structure

The Zeeman structure can be fitted to the measured line once the images are cleared of cosmic particles and corrected for their curvature and temporal shift, as well as the dispersion relation between the pixels and wavelengths was found, and the line identified.

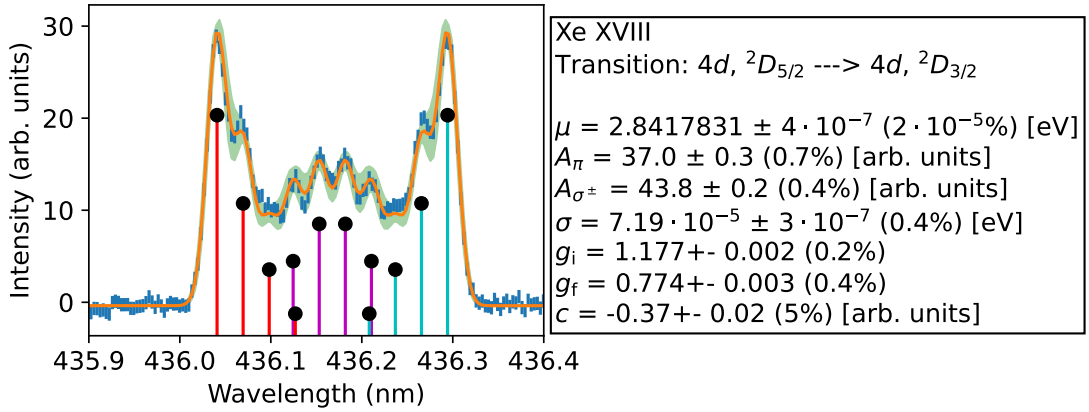

Figure 4.7: Zeeman fit result for the example Xe^{17+} transition. All fit parameters are shown on the right with their (relative) uncertainty. The green band around the fitted Zeeman structure is the 95% confidence band.

The Zeeman structures were fitted by combining Gaussian functions to each component in the Zeeman structure (see theory chapter 2.1.4)

$$I = \sum_{i,f} A_{\Delta m} \cdot \mathrm{CG}(J_i, J_f, m_i, m_f) \cdot \exp\left(-\frac{1}{2}\left(\frac{\mu + \mu_\mathrm{B} B(m_i g_i - m_f g_f)}{\sigma}\right)^2\right) + c. \tag{4.3}$$

The subscripts i and f note the initial (i, upper) and final (f, lower) state of the involved levels. The parameters to be adjusted by the fitting routine are the amplitudes $A_{\Delta m}$ of π ($\Delta m = 0$) and $\sigma^\pm$ ($\Delta m = \pm 1$) peaks, standard deviation σ, g-factors g_i and g_f, as well as center position μ and total offset c. The Clebsch-Gordan coefficients $\mathrm{CG}(J_i, J_f, m_i, m_f)$ were multiplied by the amplitude to account for the intensities of the individual peaks (see Eq. 2.20). Because the Zeeman splitting is an energy splitting, the wavelengths from the dispersion function were first converted into energy. The fitting was then done in the energy space and later converted back to wavelengths. This required the refractive index of air n_Air [134]

$$\lambda = \frac{\lambda_\mathrm{vac}}{n_\mathrm{Air}} \Rightarrow \lambda_\mathrm{vac} = \lambda \cdot \left(1 + \left(8060.51 + \frac{2480990}{132.274 - S} + \frac{17455.7}{39.32957 - S}\right) \cdot 1 \times 10^{-8}\right), \quad \text{with}: \quad S = \left(\lambda \cdot 10^{-6}\,\mathrm{m}^{-1}\right)^{-2}, \tag{4.4}$$

where λ the measured wavelength in air and λ_vac in vacuum. The energy can be calculated from the latter. Since this refractive index is wavelength-dependent, every pixel was converted according to the dispersion function. As with the dispersion function before, the ODR method [133] was used for fitting to account for the uncertainties in the independent and dependent variable.

The result of fitting such Zeeman structures can be seen in Fig. 4.7. The π components are in magenta, and the σ^+ (σ^-) is in red (cyan). The parameters from

the ODR fit are included in the figure. The percentage value behind each variable is the relative uncertainty. The center position is the most precise parameter with a relative uncertainty on the order of 10^{-7}, while values like the g-factor cannot be resolved that well. The intensities A_π and $A_{\sigma^\pm}$ are different due to their polarization, which depends on the grating and its angle. The standard deviation σ depends on the temperature of the trapped ions, as discussed above in chapter 4.1. The differences between the measured and theoretical g-factors are due to limitations in the QED calculation [135], in this case AMBIT. The nonzero background can be explained by nonuniformities which vary the dark signal or the signal response [136]. They could be mitigated by flat-field corrections, but since their effect was insignificant on the spectrum for the wavelength determination, they were not treated further.

4.3 Calcium measurement results

Highly charged calcium has first been observed in the absorption lines of the sun's corona [137]. However, these astronomical measurements usually have a precision of $\mathcal{O}(0.1\,\mathrm{nm})$ which can be improved substantially with laboratory measurements. Furthermore, highly precise IS studies have only used singly charged calcium so-far due to lack of known transitions.

To give experimentalists and theoreticians precise values to work with, highly charged calcium was investigated [F1]. To inject Ca into the EBIT, a bis-calcium (CAS No. 118448-18-3) compound [138] was heated up to 70°C in a reservoir, while being in a vacuum of a few 10^{-3} mbar. This reduced the sublimation point drastically, allowing the evaporation of the organic compound, which then flowed into the trap where it was broken down and ionized. The pressure in the two injection stages was about $P_{\mathrm{Inj},1} = 4 \times 10^{-8}$ mbar and $P_{\mathrm{Inj},2} = 2 \times 10^{-9}$ mbar.

The image acquisition time was set to 30 min for each image, averaging over seven to ten images with 16-times binning in y-axis and about four dark images to correct the signal background. For the EBIT settings, electron beam currents of no larger than 15 mA were used for the brightest lines, and only Ca^{16+} was measured at 25 mA. The low current allowed for narrow Zeeman-peaks and subsequent precise results.

As seen in Fig. 4.8 and summarized in Tab. 4.2, the measured calcium transitions were found by comparing the measurements with the energies and transition rates calculated with FAC. All of the transitions are P-P transitions, and four of which are ground-state transitions, which would allow for QLS. The transitions of the Ca^{11+}, Ca^{12+} and Ca^{14+} charge states were observed before in the solar corona with roughly hundredfold larger uncertainties [137].

Three different codes were compared to calculate the energy levels in atoms. The programs were FAC [86], AMBIT [85] and RATIP/GRASP [117]. The latter one was

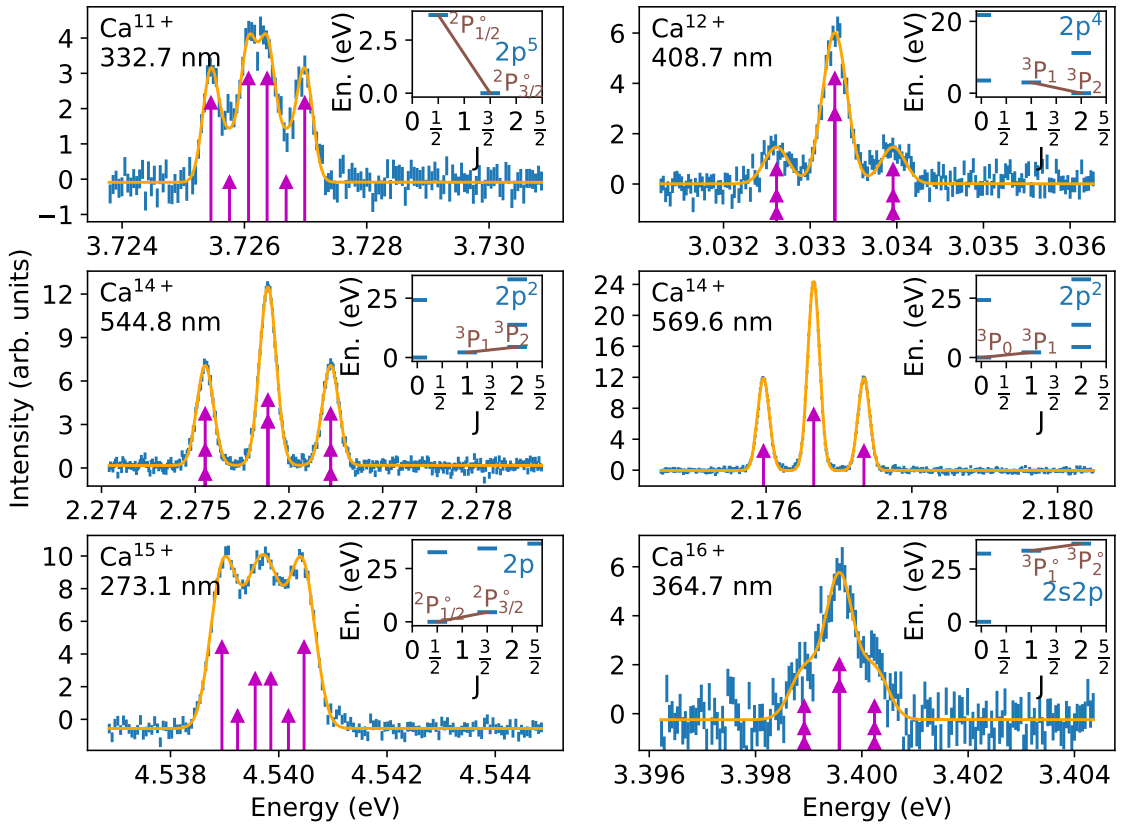

Figure 4.8: Fitted Zeeman structures in measured transitions in calcium. The magenta arrows show the placement and relative intensity of the individual components of the Zeeman splitting. The inset plots depict energy levels calculated by FAC. The line between the levels shows which transition was observed.

Table 4.2: Forbidden optical fine-structure transitions in highly charged Ca ions. Measured energies, the vacuum wavelengths λ_{vac}, and upper and lower g-factors have been observed. For comparison, two Ca^+ transitions have been included with values from the NIST database [45].

Ion	Transition	Energy (eV)	λ_{vac} (nm)	g_{upper}	g_{lower}
Ca^{11+}	$2p^5$ $^2P^\circ_{1/2}$ - $^2P^\circ_{3/2}$	3.7262192(28)	332.73458(25)	0.672(12)	1.328(7)
Ca^{12+}	$2p^4$ $^3P_1$ - $^3P_2$	3.0332843(19)	408.74572(26)	1.468(14)	1.468(14)
Ca^{14+}_a	$2p^2$ $^3P_1$ - $^3P_0$	2.1766536(10)	569.60923(26)	1.489(3)	/
Ca^{14+}_b	$2p^2$ $^3P_2$ - $^3P_1$	2.2757757(7)	544.79971(16)	1.561(44)	1.485(16)
Ca^{15+}	$2p$ $^2P^\circ_{3/2}$ - $^2P^\circ_{1/2}$	4.5397089(27)	273.11046(16)	1.326(9)	0.703(31)
Ca^{16+}	$2s2p$ $^3P^\circ_2$ - $^3P^\circ_1$	3.3995766(74)	364.70482(79)	1.428(36)	1.428(36)
Ca^+	$3d$-$4s$ $^2D_{5/2}$ - $^2S_{1/2}$	1.699932 [45]	729.348 [45]	/	/
Ca^+_b	$3d$-$4s$ $^2D_{3/2}$ - $^2S_{1/2}$	1.692408 [45]	732.389 [45]	/	/

Table 4.3: Comparison of measured Ca transition energies with the energies of three different codes for calculating atomic structure. Also included are the calculated transition rates A_{ki}. The different codes are FAC [86], RATIP/GRASP [117] and AMBIT [85].

	Observed	FAC		RATIP/GRASP		AMBIT	
Ion	Energy (eV)	En. (eV)	A_{ki} (s^{-1})	En. (eV)	A_{ki} (s^{-1})	En. (eV)	A_{ki} (s^{-1})
Ca^{11+}	3.7262192(28)	3.716(3)	483(1)	3.718(1)	483.9(1)	3.719(2)	483.5(3)
Ca^{12+}	3.0332843(19)	3.022(4)	316(1)	3.012(2)	312(1)	3.020(3)	315(1)
Ca_a^{14+}	2.1766536(10)	2.15(5)	91(6)	2.06(3)	81(3)	2.172(8)	94(1)
Ca_b^{14+}	2.2757757(7)	2.31(2)	83(2)	2.32(2)	83(2)	2.40(2)	92.4(8)
Ca^{15+}	4.5397089(27)	4.60(6)	459(17)	4.5352(2)	439.0(1)	4.67(13)	480(20)
Ca^{16+}	3.3995766(74)	3.3839(8)	272.2(2)	3.392(3)	274(1)	3.39(2)	273(1)
Ca^{+}	1.699932 [45]	1.88(6)	1.7(2)	2.0228(4)	/	1.49(5)	/

performed by Steven King at the PTB in Braunschweig. The results are listed in Tab. 4.3. All the given uncertainties for the codes were obtained by convergence tests, which required running the same calculations with slightly different parameters. The resulting variation between the results was then regarded as uncertainty. By comparing the ab-initio results of FAC, GRASP and AMBIT, it can be observed that the transition rates A_{ki} are quite similar and are likely to have mostly deviated from the calculated energy which enters with λ^{-3} (see Eq. 2.15 in chapter 2.1.2). The energies, however, vary within 0.15 eV between the calculations, except for Ca^+ which had the greatest variance. Overall, GRASP is closest to the measured values with a smaller convergence uncertainty than FAC. Calculations with AMBIT resulted in similar values, but with more scattering, which may be due to certain inaccurate input settings.

In general, comparisons between FAC and measurements resulted in a relative uncertainty of about 20% of the transition energies, which is reflected in deviations of wavelengths of up to 100 nm. Ground-state transitions typically have considerably lower uncertainties, as seen in Tab. 4.3, because only the upper level carries the uncertainty, as the ground-state is fixed at zero.

4.4 Xenon measurement results

The main advantage of xenon over calcium is that it has seven stable isotopes with a non-zero nuclear spin. This allows for up to six isotope-pairs in the KP, which is

more than the isotope-pairs in calcium or ytterbium. This large number would allow compensation for more higher-order SM effects in the GKP than Ca or Yb.

As a noble gas, Xe is inert and can be stored as a gas, which makes injection a simple matter of pressure reduction. A small reservoir was filled with about 2 bar of pressure and its flow was regulated by a needle valve into the injection cross (see chapter 3.1.4 for details on the injection system). Typical pressures in the two stages were about $P_{\mathrm{Inj},1} = 1 \times 10^{-7}$ mbar and $P_{\mathrm{Inj},2} = 1 \times 10^{-8}$ mbar. Like with many elements, it has been previously investigated predominantly in neutral and singly charged states. In fact, the NIST database [45] lists, as of today, 1955 optical transitions ranging from Xe^{+} to Xe^{7+}, but none of them are ground-state transitions.

This lack of known transitions and the fact that theoretical atomic structure calculations are more complex in xenon than in calcium, calls for an investigation of the visible transitions in multiple adjacent charge states. To obtain an overview of the spectral region, an energy scan was performed. Here, the electron beam energy was adjusted by cathode voltages from 80 V to 2500 V. The spectrometer was equipped with the 150 gr./mm grating to utilize its large bandwidth of about 90 nm (see Tab. 3.1). The wavelength was scanned by positioning the spectrometer between 340 nm and 760 nm in 85 nm steps, where the difference between bandwidth and step size generated a small overlap to avoid missing any lines and to minimize redundancy. Each separate image was projected down to the x-axis and then stacked on top of each other to obtain the intensity change for the same wavelength. This was then repeated for each step of the wavelength. While transitions were observed over the whole energy range, most of them were below 500 V. The energy scan in the lower cathode voltage range of 150 V to 500 V is shown in Fig. 4.9, which combines the images of the different wavelengths. In the energy scan, transition lines faded in and out repeatedly with rising beam energy, corresponding to its charge state present in the EBIT. The overlapping of lines was a result of a given charge state distribution present in the trap. The different lines were grouped together by examining where they begin, end, and peak in their intensity. Comparing the ionization energy and calculations with FAC helped to identify each of the charge states. These charge states are marked with a colored-coded dotted lines with a label on the right-hand side. The dots on this line indicate the transitions of that state.

Once the lines were grouped by charge state, more detailed comparisons were made with FAC or AMBIT computations to determine between which levels these transitions occurred. For example, CRM of FAC was used (see chapter 2.6.1) to calculate the relative intensity of one line to another, which was used to assess the measured lines. Calculations with AMBIT provided more precise results which were helpful for the identification. Once all of these methods were exhausted, further insight into these transitions required detailed measurements with a finer grating.

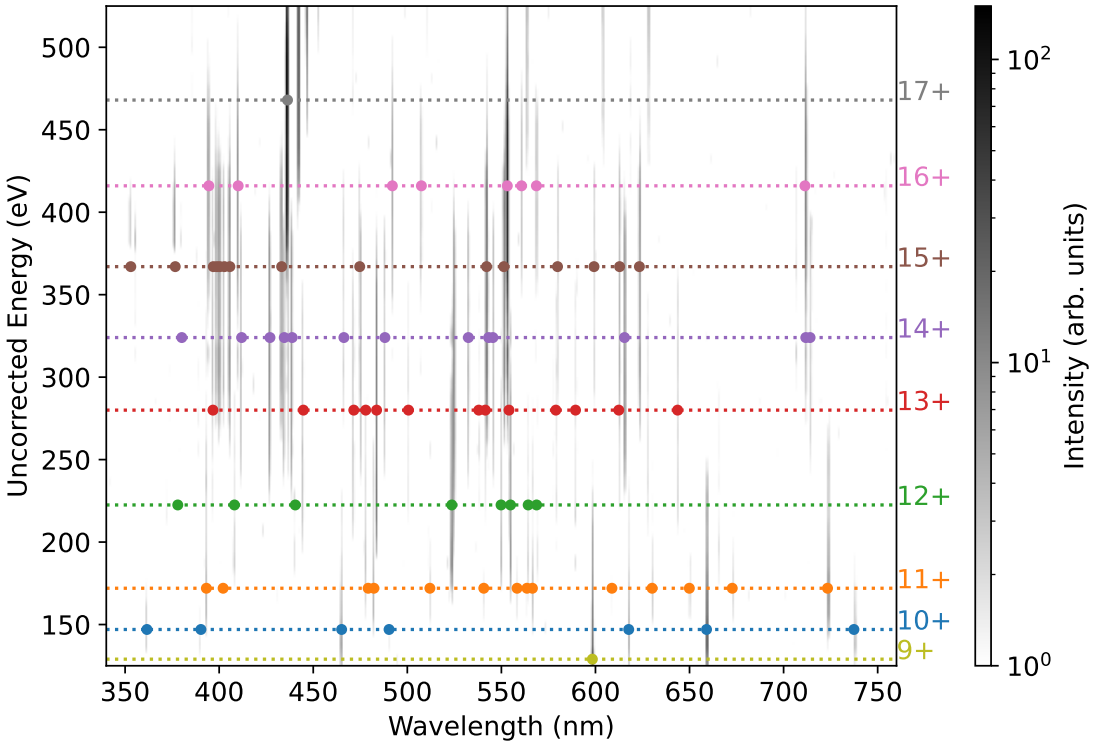

Figure 4.9: Energy-wavelength plot for the charge states of Xe^{9+} to Xe17+. The different colors indicate the maxima of different charge states, which are stated on the right side. The most prominent lines are marked with a dot.

With the 8 T magnetic field at HD-EBIT, this resulted in a Zeeman structure from which more precise wavelengths and g-factors were obtained. These results were compared with those from AMBIT calculations, which allowed further validation of the correctness of the identification.

For xenon, the exposure time per image was set to either 30 minutes, for intense transitions, or 1 hour, for weaker transitions, averaging a total of 10 hours per line. The directly measured lines are summarized in Fig. 4.10 and Tab. 4.4. Indirect lines, i.e. found via the Rydberg-Ritz combination method, are denoted as 'Ritz'. These transitions are much more diverse than the P-P transitions in calcium. Also listed are the measured g-factors in comparison to the AMBIT results. Although the spectroscopy method is not optimal for obtaining the g-factors, it can still reveal some discrepancies between theory and experiment.

In Fig. 4.11 the Grotrian diagrams of the investigated charge-states are shown. The different line-styles clarify if the line was identified (solid), only indirectly measured via Rydberg-Ritz combination (dash-dotted), or not measured but potentially of interest (dashed). Preliminary identifications are represented by dotted lines and further measurements are needed to dispel any ambiguity. [F2]

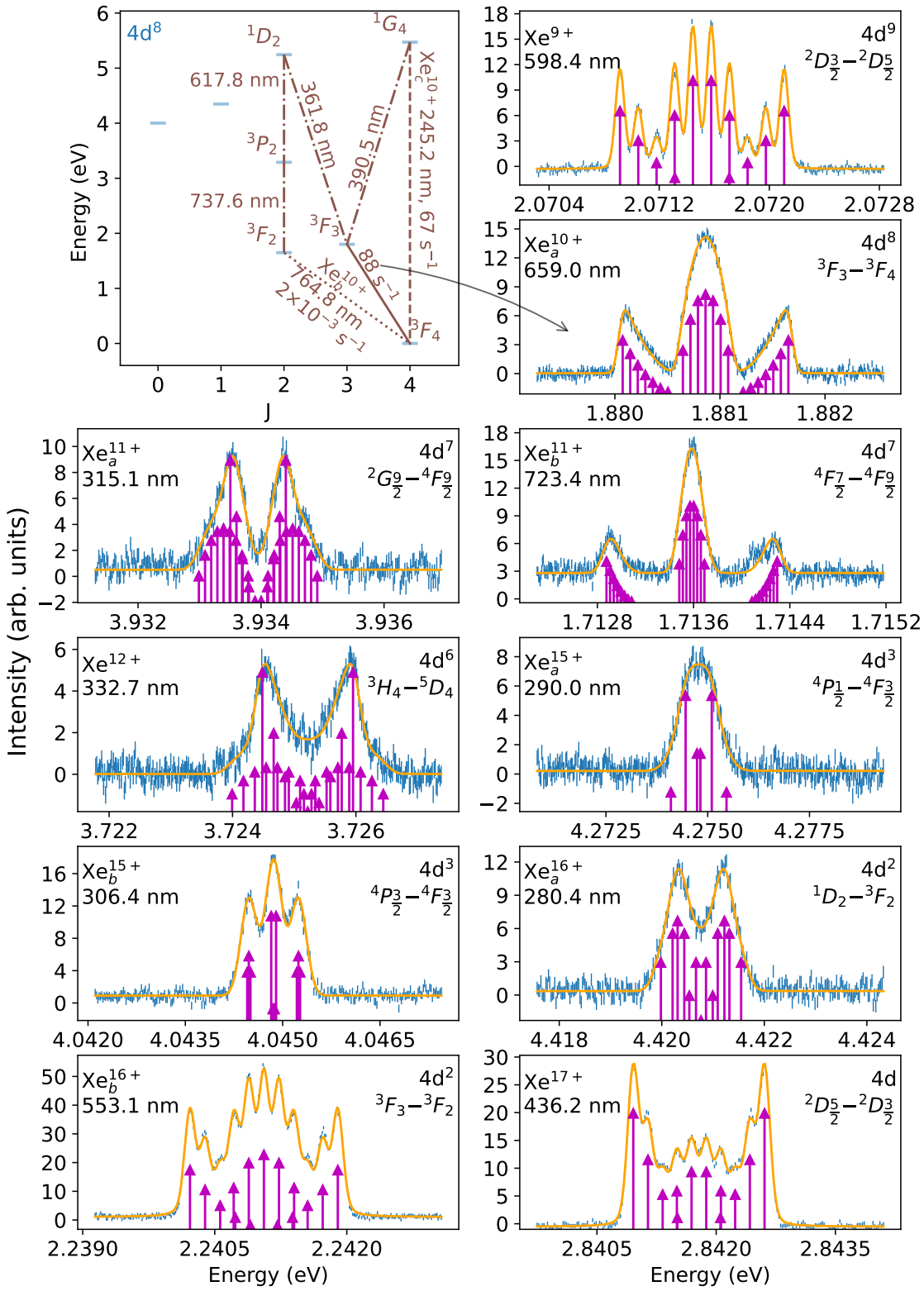

Figure 4.10: Zeeman structure in the directly measured transitions in xenon. The magenta arrows depict the positioning of the individual Zeeman components. For Xe^{10+} a level scheme by FAC shows the calculated electric quadrupole (E2) transition by Rydberg-Ritz combination.

Table 4.4: Ground-state transitions found in highly charged Xe ions: Measured energies, vacuum wavelengths λ_{vac}, and g-factors of upper and lower energy levels obtained through fitting of the Zeeman-structure with their corresponding uncertainties. Theoretical transition probabilities A_{ki} and ab-intio wavelengths λ_{A} were calculated with AMBIT [85].

			Observed values				calculations				
Ion	Transition		Energy (eV)	λ_{vac} (nm)	g_{upper}	g_{lower}	λ_{A}(nm)	A_{ki}(s^{-1})	$g_{A,\mathrm{upper}}$	$g_{A,\mathrm{lower}}$	Type
Xe^{9+}	$4d^9$	$^2D_{3/2}$ - $^2D_{5/2}$	2.07151156(28)	598.520419(90)	0.792(2)	1.189(1)	595.4	67.5	0.8	1.2	M1
Xe_a^{10+}	$4d^8$	$^3F_3$ - $^3F_4$	1.8808627(14)	659.18789(56)	1.082(4)	1.238(3)	665.1	88.4	1.0833	1.2426	M1
Xe_b^{10+}	$4d^8$	$^3F_2$ - $^3F_4$	1.62122(21)	764.8753(16)(R)	/	/	735.6	0.002	0.9792	1.2426	**E2**
Xe_c^{10+}	$4d^8$	$^1G_4$ - $^3F_4$	5.05708(39)	245.18684(36)(R)	/	/	242.9	67.1	1.0074	1.2426	M1
Xe_a^{11+}	$4d^7$	$^2G_{9/2}$ - $^4F_{9/2}$	3.9339517(50)	315.16451(45)	1.105(37)	1.321(35)	313.3	107.7	1.0823	1.3054	M1
Xe_b^{11+}	$4d^7$	$^4F_{7/2}$ - $^4F_{9/2}$	1.71358555(87)	723.53667(37)	1.242(9)	1.306(7)	727.4	82.8	1.2276	1.3054	M1
Xe^{12+}	$4d^6$	$^3H_4$ - $^5D_4$	3.7252183(78)	332.82398(79)	1.058(32)	1.455(31)	328.6	110.8	1.0438	1.462	M1
Xe_a^{15+}	$4d^3$	$^4P_{1/2}$ - $^4F_{3/2}$	4.2747781(74)	290.03657(50)	2.17(20)	0.78(9)	297.7	16.8	2.2137	0.47304	M1
Xe_b^{15+}	$4d^3$	$^4P_{3/2}$ - $^4F_{3/2}$	4.0448609(24)	306.52277(20)	0.856(57)	0.799(28)	337.1	101.7	1.4357	0.47304	M1
Xe_a^{16+}	$4d^2$	$^1D_2$ - $^3F_2$	4.4207651(39)	280.45869(25)	1.197(11)	0.704(15)	271.3	84.4	1.2027	0.70681	M1
Xe_b^{16+}	$4d^2$	$^3F_3$ - $^3F_2$	2.24105833(38)	553.23949(11)	1.073(1)	0.702(2)	555.4	137.6	1.0833	0.70681	M1
Xe_c^{16+}	$4d^2$	$^3P_1$ - $^3F_2$	4.9243572(77)	251.77721(33)(R)	/	/	244.3	10.3	1.5	0.70681	M1
Xe^{17+}	$4d$	$^2D_{5/2}$ - $^2D_{3/2}$	2.84178291(47)	436.290179(73)	1.184(2)	0.785(3)	433.8	123.7	1.2	0.8	M1

R: Rydberg-Ritz combination

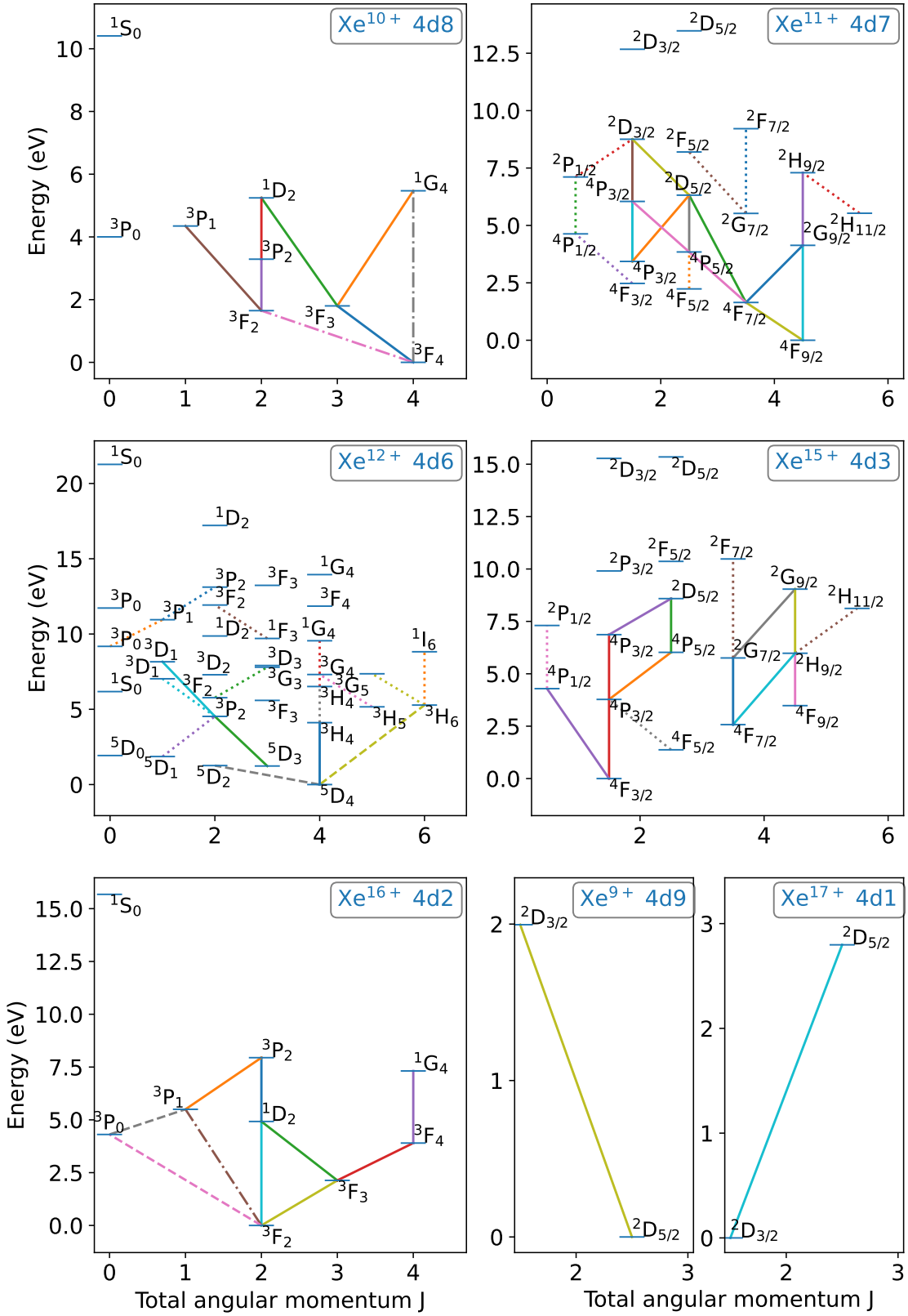

Figure 4.11: Grotrian diagrams of the investigated xenon charge states Xe^{9+} through Xe^{16+}. Solid lines represent identified transitions. Dash-dotted lines represent transitions calculated via Rydberg-Ritz combination. Dotted lines represent preliminary identifications and dashed lines are not found, but potentially interesting E2 transitions.

Details of these lines can be found in Tab. 4.5 for Xe^{10+}, Xe^{11+} and Xe^{12+}, while the charge states Xe^{15+} and Xe^{16+} are listed in Tab. 4.6.

In Xe^{10+}, all optical transitions were identified, which allowed the calculation of an E2 line at 764.8 nm, as listed in Tab. 4.4. This transition has a narrow natural linewidth of 0.3 mHz, which makes it a potential clock candidate.

All optical transitions were also successfully identified in Xe^{16+}. Unobserved M1 and E2 transitions were added to Tab. 4.6 with their AMBIT results, which are denoted with an A. Its E2 transition has a transition rate of $A_{ki} = 1.05\,s^{-1}$ and thus a natural linewidth of $\delta\nu = 0.15$ Hz, which indicates that this transition would be a potential clock candidate as well. To find its true transition energy, a 955 nm, $19\,s^{-1}$ M1 transition needs to be measured first. To find this missing transition, the experimental setup will have to be adjusted for the infrared range. Doing so will enable the identification of the line between all the known higher-orders, despite a weak rate of $A_{\mathrm{ki}} = 19\,s^{-1}$.

Xe^{11+}, Xe^{12+} and Xe^{15+} include preliminary identifications, denoted with a p, where identification was ambiguous as either the Zeeman structure was not sufficiently resolved or there were too many lines too close to each other to be identified with the given FAC and AMBIT uncertainties. In Xe^{11+} and Xe^{15+}, most identifications resulted from the Ritz-Rydberg combination principle. Xe^{12+} had less intense transitions, which could be attributed to the large number of electronic levels. This low intensity had the drawback that the Ritz-Rydberg combination principle could not be applied. However, Xe^{12+} may contain two ultra-narrow E2 transitions with an expected natural linewidth of as low as 0.016 mHz, if calculations are correct. To ultimately find them, however, more work is required, as a large variety of transitions have to be identified first.

Transitions measured in other charge states are not listed here, because they had no observable ground-state transitions. This made them irrelevant in this work and thus they were left mainly unidentified but listed in the appendix A.

Table 4.5: Other identified transitions in Xe^{10+}, Xe^{11+} and Xe^{12+}. Transition details, ab-initio wavelength λ_A and A_{ki} values are based on AMBIT calculations. Xe^{10+} transitions were used to calculate Ritz-Rydberg combination listed in Tab. 4.4. Xe^{12+} contains two with AMBIT calculated E2 transitions to point them out.

Ion	Transition		Energy (eV)	λ_{vac} (nm)	λ_A (nm)	A_{ki} (s^{-1})
Xe^{10+}	$4d^8$	$^1D_2$ - $^3F_3$	3.4276528(10)	361.71748(10)	353.6	159.5
Xe^{10+}	$4d^8$	$^1G_4$ - $^3F_3$	3.1758602(72)	390.39563(88)	382.6	10.7
Xe^{10+}	$4d^8$	$^3P_1$ - $^3F_2$	2.6655150(26)	465.14163(45)	453.7	47.8
Xe^{10+}	$4d^8$	$^1D_2$ - $^3P_2$	2.0067271(28)	617.84283(85)	615.9	55.8
Xe^{10+}	$4d^8$	$^3P_2$ - $^3F_2$	1.68081600(90)	737.64289(39)	741.4	35.3
Xe^{11+}	$4d^7$	$^2D_{5/2}$ - $^4F_{7/2}$	4.397932(52)	281.9147(33)	272.9	246.1
Xe^{11+}	$4d^7$	$^2H_{9/2}$ - $^2G_{9/2}$	3.1523(48)	393.3(6)	395.9	99.6
Xe^{11+}	$4d^7$	$^2D_{5/2}$ - $^4P_{3/2}$	2.8739(33)	431.42(49)	422.0	42.4
Xe^{11+}	$4d^7$	$^2D_{3/2}$ - $^4P_{3/2}$	2.5866(22)	477.713(90)	468.0	104.4
Xe^{11+}	$4d^7$	$^4P_{3/2}$ - $^4P_{3/2}$	2.5707010(33)	482.29723(62)	474.9	113.5
Xe^{11+}	$4d^7$	$^2D_{5/2}$ - $^4P_{5/2}$	2.4899(15)	497.93(29)	494.9	27.4
Xe^{11+}	$4d^7$	$^2D_{3/2}$ - $^2D_{5/2}$	2.29265(30)	540.790(70)	533.8	53.9
Xe^{11+}	$4d^7$	$^2G_{9/2}$ - $^4F_{7/2}$	2.21997(16)	558.50(4)	550.3	8.8
Xe^{11+}	$4d^7$	$^4P_{3/2}$ - $^4P_{5/2}$	2.18799(39)	566.66(10)	569.2	61.8
Xe^{11+}	$4d^7$	$^2P_{5/2}$ - $^4F_{7/2}$	1.907216(88)	650.079(30)	608.4	16.7
$Xe^{11+}p$	$4d^7$	$^2F_{7/2}$ - $^2G_{7/2}$	3.0825(38)	402.21(50)	361.5	37.7
$Xe^{11+}p$	$4d^7$	$^2F_{5/2}$ - $^2G_{7/2}$	2.5732(21)	481.83(39)	525.0	6.7
$Xe^{11+}p$	$4d^7$	$^2P_{1/2}$ - $^4P_{1/2}$	2.42089(80)	512.14(16)	510.7	129.1
$Xe^{11+}p$	$4d^7$	$^4P_{1/2}$ - $^4F_{3/2}$	2.03614(13)	608.918(40)	597.5	21.5
$Xe^{11+}p$	$4d^7$	$^2H_{9/2}$ - $^2H_{11/2}$	1.842646(25)	672.860(9)	674.3	29.3
$Xe^{11+}p$	$4d^7$	$^2D_{3/2}$ - $^2P_{1/2}$	1.76973(23)	700.583(90)	732.5	10.1
$Xe^{11+}p$	$4d^7$	$^4P_{5/2}$ - $^4F_{5/2}$	1.54551(39)	802.22(20)	837.6	5.8
Xe^{12+}	$4d^6$	$^3D_1$ - $^3P_2$	3.7282435(96)	332.55391(86)	340.1	105.5
Xe^{12+}	$4d^6$	$^3P_2$ - $^5D_3$	3.278867(10)	378.1313(12)	365.2	203.9
$Xe^{12+}p$	$4d^6$	$^1I_6$ - $^3H_6$	3.327889(18)	372.5611(20)	373.2	72.4
$Xe^{12+}p$	$4d^6$	$^1G_4$ - $^3H_4$	3.0372(30)	408.21(39)	394.5	121.3
$Xe^{12+}p$	$4d^6$	$^3P_2$ - $^5D_1$	2.81415(10)	440.57(15)	459.0	66.0
$Xe^{12+}p$	$4d^6$	$^3F_2$ - $^1F_3$	2.4539(11)	505.25(22)	480.6	63.6
$Xe^{12+}p$	$4d^6$	$^3G_4$ - $^3H_5$	2.42449(90)	511.38(18)	505.6	33.8
$Xe^{12+}p$	$4d^6$	$^3H_4$ - $^3H_4$	2.36708(45)	523.79(10)	527.9	120.3
$Xe^{12+}p$	$4d^6$	$^3G_5$ - $^3H_6$	2.2546375(23)	549.90744(55)	540.0	54.3
$Xe^{12+}p$	$4d^6$	$^3D_1$ - $^3P_2$	2.23393(12)	555.01(3)	549.9	75.9
$Xe^{12+}p$	$4d^6$	$^3P_2$ - $^3P_1$	2.19676(47)	564.39(11)	584.9	60.8
$Xe^{12+}p$	$4d^6$	$^3P_1$ - $^3P_0$	2.17953(38)	568.86(10)	592.8	54.6
$Xe^{12+}p$	$4d^6$	$^3D_3$ - $^3F_2$	1.928492(90)	642.907(30)	636.9	31.6
$Xe^{12+}A\,(E2)$	$4d^6$	$^5D_2$ - $^5D_4$	/	/	931.8	0.0007
$Xe^{12+}A\,(E2)$	$4d^6$	$^3H_6$ - $^5D_4$	/	/	274.6	0.0001

p: preliminary, A: AMBIT results only

Table 4.6: Continuation of identified non-grounds-state transitions in Xe^{15+} and Xe^{16+}. Transitions from Xe^{16+} used for Rydberg-Ritz combination to calculate one transition in Tab. 4.4. Xe^{16+} also contains two with AMBIT calculated transitions to point them out.

Ion	Transition		Energy (eV)	λ_{vac} (nm)	λ_{A}(nm)	A_{ki}(s^{-1})
Xe^{15+}	$4d^3$	$^2G_{9/2}$ - $^2G_{7/2}$	3.2906036(29)	376.78253(33)	376.7	162.6
Xe^{15+}	$4d^3$	$^4P_{3/2}$ - $^4P_{3/2}$	3.1088401(49)	398.81175(62)	397.9	198.8
Xe^{15+}	$4d^3$	$^2H_{9/2}$ - $^4F_{7/2}$	3.096290(15)	400.428(2)	394.2	76.5
Xe^{15+}	$4d^3$	$^2G_{9/2}$ - $^2H_{9/2}$	3.056024(16)	405.7042(21)	400.6	160.5
Xe^{15+}	$4d^3$	$^2G_{7/2}$ - $^4F_{7/2}$	2.861683(14)	433.2561(21)	420.4	65.7
Xe^{15+}	$4d^3$	$^2D_{5/2}$ - $^4P_{5/2}$	2.41424(85)	513.55(17)	501.1	11.8
Xe^{15+}	$4d^3$	$^2H_{9/2}$ - $^4F_{9/2}$	2.286319(11)	542.2875(25)	536.6	82.9
Xe^{15+}	$4d^3$	$^4P_{5/2}$ - $^4P_{3/2}$	2.2483297(50)	551.4502(12)	554.1	59.6
Xe^{15+}	$4d^3$	$^2D_{5/2}$ - $^3P_{3/2}$	1.55279(97)	798.45(49)	777.0	18.1
$Xe^{15+}p$	$4d^3$	$^2F_{7/2}$ - $^2G_{7/2}$	4.269411(14)	290.40114(96)	278.6	50.6
$Xe^{15+}p$	$4d^3$	$^2P_{1/2}$ - $^4P_{1/2}$	3.123792(52)	396.9028(66)	392.8	233.2
$Xe^{15+}p$	$4d^3$	$^4P_{3/2}$ - $^4F_{5/2}$	2.06849(17)	599.395(50)	548.0	10.3
$Xe^{15+}p$	$4d^3$	$^2H_{11/2}$ - $^2H_{9/2}$	1.988448(64)	623.522(20)	615.4	30.3
Xe^{16+}	$4d^2$	$^1G_4$ - $^3F_4$	3.14220(18)	394.577(22)	383.2	69.5
Xe^{16+}	$4d^2$	$^3P_2$ - $^1D_2$	3.0230061(48)	410.13545(65)	407.7	165.2
Xe^{16+}	$4d^2$	$^3P_2$ - $^3P_1$	2.5194098(20)	492.11604(39)	489.0	61.2
Xe^{16+}	$4d^2$	$^1D_2$ - $^3F_3$	2.17991(38)	568.8(1)	530.3	20.2
Xe^{16+}	$4d^2$	$^3F_4$ - $^3F_3$	1.7426542(51)	711.4675(21)	701.8	50.6
$Xe^{16+}A$	$4d^2$	$^3P_1$ - $^3P_0$	/	/	955.0	19.1
$Xe^{16+}A\,(E2)$	$4d^2$	$^3P_0$ - $^3F_2$	/	/	328.2	1.05

p: preliminary, A: AMBIT results only

Chapter 5

Analysis

FAC calculations were used to evaluate how discovered ground-state transitions shift in the presence of a hypothetical fifth force between electrons and neutrons. Though the ab-initio results of FAC were the least accurate compared to that from other codes, calculation of shifts within the level structure is of comparable accuracy to GRASP. This was confirmed by an inclusion of a Yukawa potential in both codes and cross-checking the results. As the minute fifth force shifts are below the numerical precision of FAC, the SM coefficients K and F, as well as the NP coefficient X (see chapter 2.3.1), were extracted and handled with higher numerical precision separately.

From Eq. 2.22, the relation between the energy levels and the atom mass can be seen as $\nu = C + K\frac{1}{m} + Fr^2$. To extract K, the terms C and Fr^2 must be removed. The MS can be toggled in FAC. The energy levels were then calculated twice, once with MS E_{MS} and once without MS $E_{\mathrm{no-MS}}$. By taking the difference in transition of interest ν within these level structures, the MS coefficient K was obtained with

$$K = (\nu_{\mathrm{MS}} - \nu_{\mathrm{no-MS}}) \cdot m. \qquad (5.1)$$

Here, m is mass of the atom used in the calculation. The resulting MS parameter K is in units of $\mathrm{eV} \cdot \mathrm{u}$.

Extracting the FS coefficient F required slightly more work. Firstly, the energy levels for five different atomic radii were calculated. These radii were scaled by $r = \sqrt{r_{\mathrm{RMS}}^2(1 + 2 \cdot n)}$ with $n \in [0, 1, 2, 3, 4]$ and r_{RMS} the root-mean-

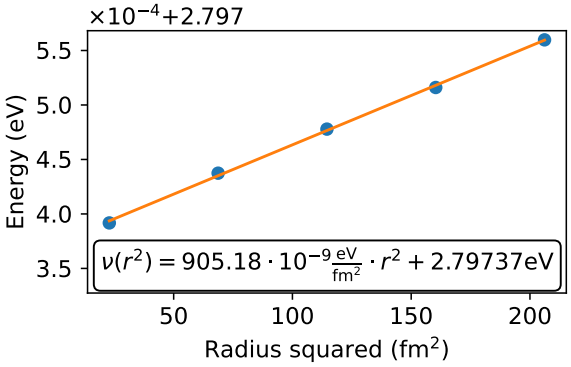

Figure 5.1: FS coefficient extraction from the slope of a linear fit on the energy over the squared radius. Example based on the measured Xe^{17+} transition.

square radius of the atom. Secondly, a linear regression was performed between r^2 and the transition energy $\nu(r)$:

$$\nu(r) = F \cdot r^2 + c_0. \tag{5.2}$$

Here, $c_0 = C + K\frac{1}{m}$ are the radius-independent parts. The slope is the F coefficient in units of eV/fm^2. This regression is depicted in Fig. 5.1 on the example of Xe^{17+}.

Lastly, the fifth force-shift coefficients $X(m_\Phi)$ were extracted. For this extraction, a Yukawa-potential $V_{\text{Yuk.}}(m_\Phi)$ (see chapter 2.3 and in particular Eq. 2.21.) was added to the existing atomic potential. The force range changes with m_Φ and thus required a recalculation of the energy levels for each m_Φ. A realistic coupling parameter would cause very minute shifts, which are too small to be directly obtained. Instead, a coupling parameter of $y_e y_n = 0.01$ was used, which was big enough to overcome numerical limitations, but still small enough to not impose any significant level mixing. The extraction was performed using the difference between the transition energies ν with and without fifth force-shift, resulting in

$$X(m_\Phi) = \frac{100 \cdot \left(\nu(m_\Phi) - \nu_{\text{no-5th-force}}\right)}{N}. \tag{5.3}$$

The factor 100 is a result from the chosen coupling constant $y_e y_n = 0.01 \rightarrow 1/y_e y_n = 100$ for the calculations. To account for the number of neutrons present in the nucleus, the value was then divided by the neutron number N. Once the coefficient X was extracted, the coupling parameter was set to realistic values in separate calculations.

5.1 Isotope shifts and King plots

With the extracted electronic coefficients, the IS can be constructed with Eq. 2.27, as introduced in chapter 2.3. Modifying the IS with the mass parameter and plotting two transitions against each other for the different isotope-pairs resulted in the KP, see Eq. 2.28.

5.1.1 Calcium isotope shift

The calculated electronic coefficients for MS, FS, and for key mediator masses of the fifth force are listed in Tab. 5.1 for the calcium transitions listed in Tab. 4.2. To test the accuracy of the fifth force contributions from the FAC results, values obtained with the GRASP program are listed as well. They were calculated by Steven King at the Physikalisch-Technische Bundesanstalt (PTB) in Braunschweig (National Metrology Institute). The X coefficients were similar, confirming the principle of an added Yukawa potential in both programs. Towards heavier m_Φ, the relative

Table 5.1: NP electronic coefficients X(m_Φ) in eV calculated with FAC and RATIP/-GRASP for different mediator masses m_Φ. Their respective SM electronic sensitivity coefficients K and F were calculated only with FAC.

	$X(m_\Phi)$ (eV)								SM coefficients	
m_Φ =	$10^3 \frac{\text{eV}}{\text{c}^2}$		$10^4 \frac{\text{eV}}{\text{c}^2}$		$10^5 \frac{\text{eV}}{\text{c}^2}$		$10^6 \frac{\text{eV}}{\text{c}^2}$		K (eV·u)	F $\left(\frac{\text{eV}}{\text{fm}^2}\right)$
Trans.	FAC	GRASP	FAC	GRASP	FAC	GRASP	FAC	GRASP	$\times 10^{-3}$	$\times 10^{-9}$
Ca^{11+}	9.85	9.81	8.82	8.80	1.54	1.67	0.0163	0.0252	-2.85	-104
Ca^{12+}	8.36	8.33	7.51	7.51	1.33	1.45	0.0139	0.0221	-2.43	-123
Ca_a^{14+}	6.71	6.06	6.07	5.51	1.07	1.07	0.0065	0.0126	-1.83	-21
Ca_b^{14+}	4.89	4.88	4.45	4.40	0.96	0.80	0.0203	0.0087	-1.90	-196
Ca^{15+}	11.4	11.2	10.4	10.2	2.47	2.44	0.0605	0.0573	-4.96	-577
Ca^{16+}	8.69	8.56	7.90	7.78	1.52	1.51	0.0177	0.0177	-2.76	-134
Ca^+	-32.0	-35.3	9.37	14.8	2.52	4.52	0.119	0.223	-3.13	-1310
Ca_b^+	-31.9	/	9.36	/	2.51	/	0.119	/	-3.15	-1310

differences between the programs increased as the fifth force effect weakened, and thus extraction of X coefficient became increasingly limited by numerical precision. The largest deviation was between the results in Ca^+, possibly due to its transition between different configurations.

This is visualized in Fig 5.2 (a) which shows the NP IS for different mediator masses for a single isotope-pair. A comparison of the FAC and GRASP results make it apparent that the Ca^+ transition is most sensitive to a fifth force but exhibits the strongest deviations between both programs. In contrast, the HCIs are easier to compute theoretically due to the reduced number of electrons and subsequent fewer electron-electron interactions. Moreover, the electronic levels of the transitions are within the same configuration ($2p^x$), and therefore have better precision than transitions between configurations.

From the calculated IS, a KP was constructed. Fig. 5.2 (b) shows such a KP for two of the found transitions. The points are the four isotope-pairs based on the five stable even isotopes in calcium. This KP is specific for one selected mediator mass $m_\Phi = 10^5\,\text{eV/c}^2$, and needs to be reconstructed in the analysis for every m_Φ. The inset plots present a closeup of the different points, showing their deviation from the orange King-linearity. This effect scales with the coupling parameter $y_e y_n$, which, in this example, was set to a realistic value $y_e y_n = 10^{-13}$, as shown in Fig. 2.4.

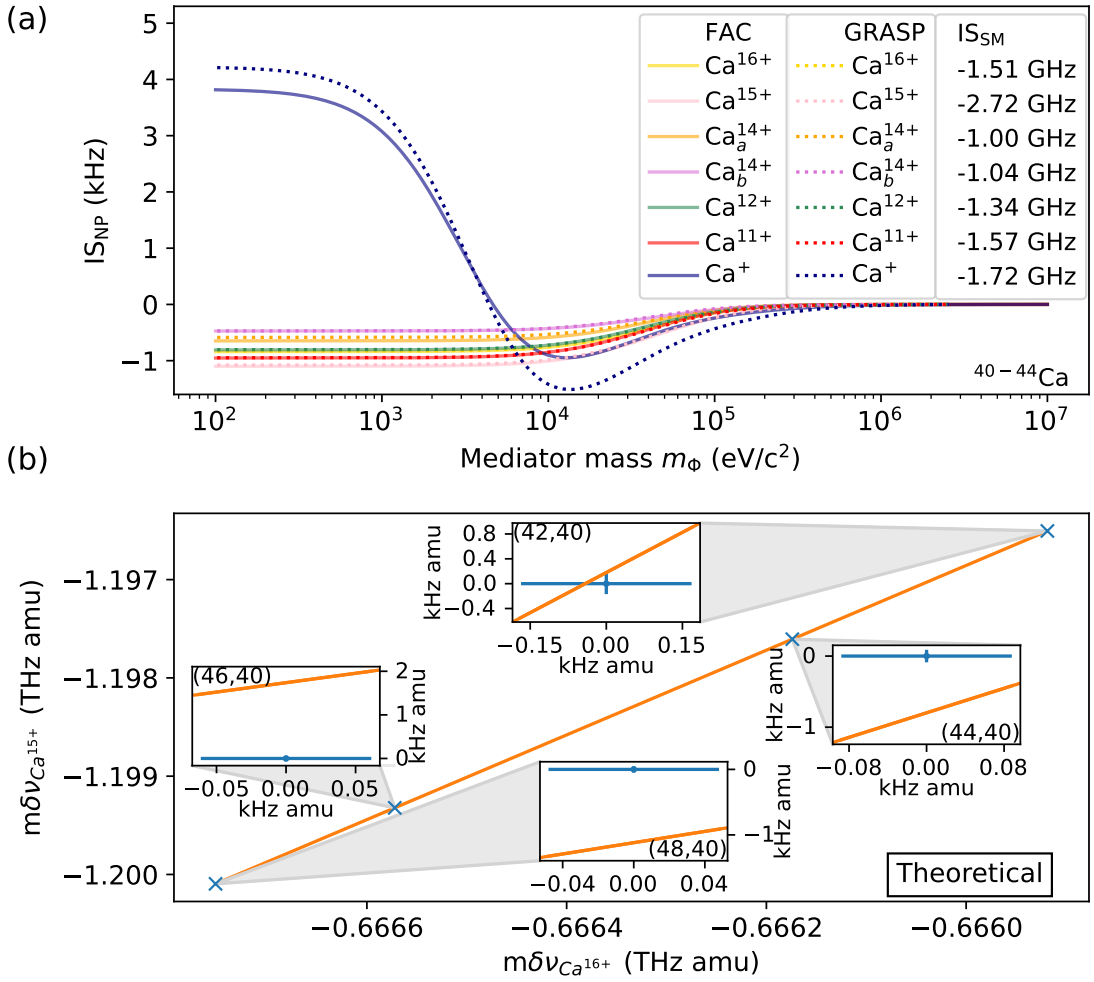

Figure 5.2: IS and KP for the measured calcium transitions and a fixed coupling strength of $y_e y_n = 10^{-13}$. (a) Theoretical IS caused by a NP mediator in the $(40, 44)$ isotope pair. Ca^+ has been added as comparison. IS of first-order SM included in the third column of the legend. Calculated with FAC and GRASP/RATIP. (b) Example KP based on IS of two Ca transitions at a fixed $m_\Phi = 10^5\,\mathrm{eV/c^2}$.

5.1.2 Xenon isotope shift

Repeating the same process in xenon, FAC calculations resulted in X values for different m_Φ, as well as the SM coefficients K and F. These are tabulated in Tab. 5.2.

Compared to that of calcium (Tab. 5.1) the X coefficients are smaller by about a factor of two, which can be explained by the electronic wavefunction and its overlap with the nucleus, which is greater for the $2p$ shell in Ca than for the $4d$ shell in Xe. This reinforces the concept that, wavefunctions closer to the nucleus exhibit a stronger shift by a fifth force, thus making the search potentially be easier. This topic will be discussed further in chapter 7.1. Calculated NP IS for the Xe isotope-pair $(132, 124)$ for a coupling strength of $y_e y_n = 10^{-13}$ is shown in Fig. 5.3 (a). Similar to the HCI transitions in Ca, the found transitions showed an overall common shift as they are in the same shell. The KP can be generated from this IS using mass parameters of $m_\Phi = 10^5\,\mathrm{eV/c^2}$, as shown in Fig. 5.3 (b). The insets show a close-up of the positions of the six isotope-pairs relative to the linear line.

It should be noted here that these X coefficients or the $\mathrm{IS_{NP}}$ only partially represent the estimation of the sensitivity to a fifth force. The actual sensitivity stems from the NL in the KP, which includes the FS coefficient F, and the NP X coefficient of both transitions in the NL term (see chapter 2.3 and in particular Eq. 2.28 and Fig. 2.6). This combination of effects makes a quick assessment difficult.

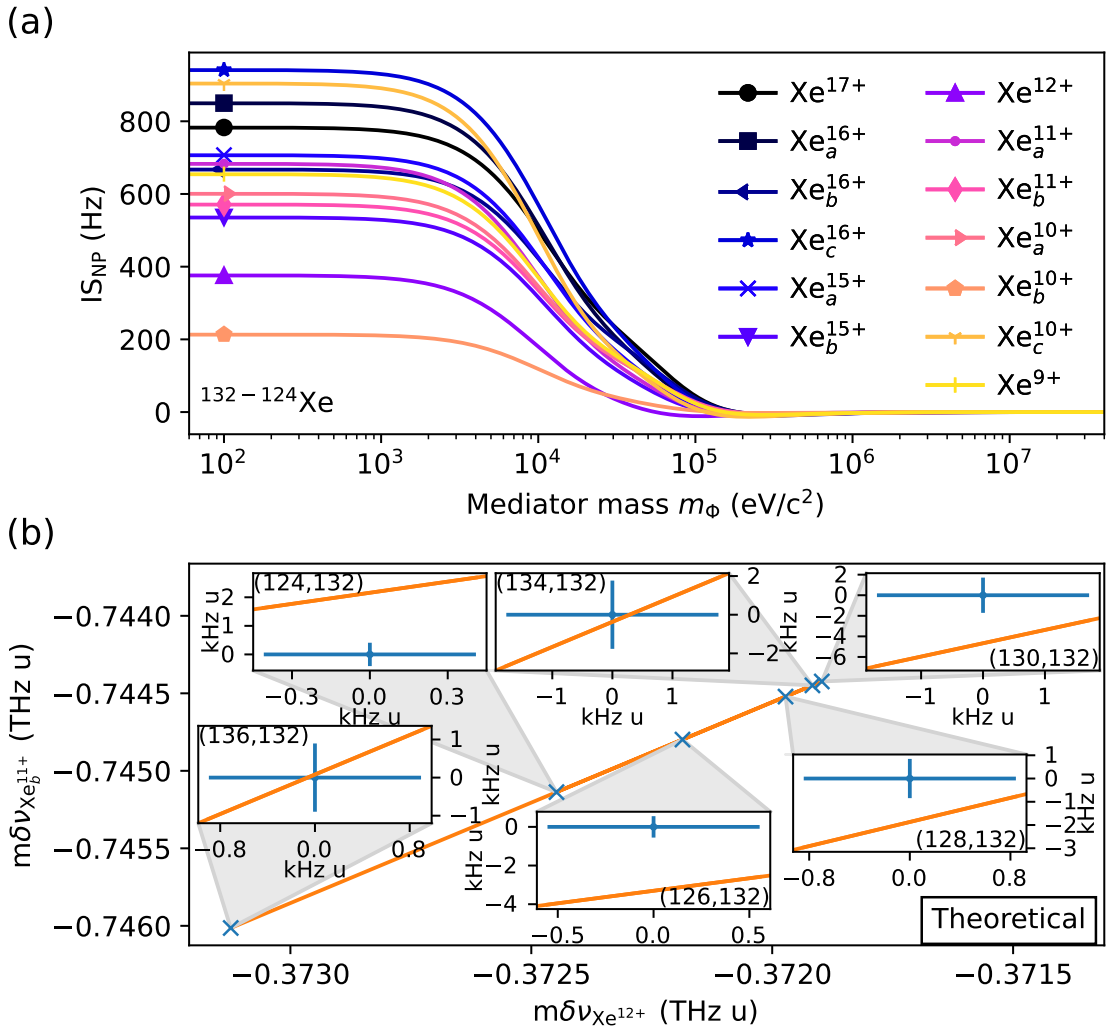

Figure 5.3: Results of NP IS from FAC for a coupling strength of $y_e y_n = 10^{-13}$. (a) Isotope shift by a NP mediator for the xenon transitions. (b) Example KP based on $m_\Phi = 10^5\,\mathrm{eV/c^2}$ and an assumed measurement uncertainty of $\Delta\nu = 100\,\mathrm{mHz}$.

Table 5.2: NP electronic coefficients X(m_Φ) in eV for different mediator masses m_Φ. Their respective SM electronic sensitivity coefficients K and F were used for the IS calculations. All of these values have been calculated with FAC.

	$X(m_\Phi)$ (eV)				SM coefficients	
Trans. \ m_Φ	$10^3\frac{\text{eV}}{\text{c}^2}$	$10^4\frac{\text{eV}}{\text{c}^2}$	$10^5\frac{\text{eV}}{\text{c}^2}$	$10^6\frac{\text{eV}}{\text{c}^2}$	K (eV·u)	F $\left(\frac{\text{eV}}{\text{fm}^2}\right)$
Xe^{9+}	3.34	1.92	0.122	-0.0123	-3.32×10^{-3}	785×10^{-9}
Xe_a^{10+}	3.06	1.79	0.124	-0.0113	-3.16×10^{-3}	624×10^{-9}
Xe_b^{10+}	1.09	0.612	0.0198	-0.0043	1.15×10^{-3}	264×10^{-9}
Xe_c^{10+}	4.61	2.51	0.0483	-0.0168	-4.70×10^{-3}	973×10^{-9}
Xe_a^{11+}	3.48	1.93	0.0616	-0.0118	-2.22×10^{-3}	723×10^{-9}
Xe_b^{11+}	2.91	1.74	0.143	-0.0093	-3.06×10^{-3}	552×10^{-9}
Xe^{12+}	1.91	0.927	-0.0586	-0.0067	-1.52×10^{-3}	426×10^{-9}
Xe_a^{15+}	3.61	2.20	0.0958	-0.0132	-0.931×10^{-3}	842×10^{-9}
Xe_b^{15+}	2.73	1.64	0.0437	-0.0099	0.119×10^{-3}	632×10^{-9}
Xe_a^{16+}	4.34	2.66	0.133	-0.0156	-7.65×10^{-3}	964×10^{-9}
Xe_b^{16+}	3.414	2.185	0.200	-0.0121	-3.72×10^{-3}	757×10^{-9}
Xe_c^{16+}	4.81	2.95	0.150	-0.0172	-9.01×10^{-3}	1066×10^{-9}
Xe^{17+}	4.01	2.58	0.230	-0.0144	-4.76×10^{-3}	905×10^{-9}

5.2 Exclusion plots

The evaluation of KPs has been prepared in chapter 2.3, where the NL by the fifth force is quantified by the area it spans over the isotope-pairs. This area is contrasted against its uncertainty, which is set by the measurement and isotope mass uncertainties. As discussed in the previous chapter, the IS of the fifth force changes with different mediator masses m_Φ, which set the range of the force. A new KP was made for each m_Φ, as shown in Fig. 5.2 (b) and Fig. 5.3 (b). The ratio of spanned area to its uncertainty is the resolvability R (see chapter 2.3.2), which must be $R = 1$ to find the limit of uncertainty, i.e. when the error bars of the isotope-pairs reach the King-linearity line. This $R = 1$ was achieved by adjusting the coupling strength $y_e y_n$ of the fifth force until this criteria was met. This procedure was repeated for every mediator mass m_Φ in the range of $1\,\text{eV/c}^2$ to $10^7\,\text{eV/c}^2$. The resulting $y_e y_n(m_\Phi)$ can be plotted as an exclusion plot, similar to the one previously seen in Fig. 2.4.

Different parings of transitions for the KP analysis result in their own sensitivity line. As these lines are the lower limit ($R = 1$), they exclude the parameter space above them.

5.2.1 Calcium exclusion plot

The exclusion plot for calcium is shown in Fig. 5.4. The dashed lines represent the sensitivities from classical KPs, where isotopes mass uncertainties and higher SM orders were omitted. The most recent IS study in calcium was performed by Ref. [40]. They measured two Ca^+ 3d-4s transitions of 732 nm and 729 nm with an uncertainty of 20 Hz. This exclusion line is shown in Fig. 5.4 as an annotated yellow dashed line. If the same pair would be measured again with the predicted uncertainty of 100 mHz by the QLS method, the sensitivity would increase by a factor of 20 Hz/100 mHz = 200, shown as the orange dashed line.

The KP analysis of the transitions listed in Tab. 5.1 resulted in a large variety of sensitivity lines, the highest of which was achieved with Ca^{15+} paired with Ca_a^{14+}, shown as red dashed line, and the pairing of Ca^{15+} with Ca^+, shown as green dashed line. Both of these are two orders of magnitude more sensitive than the Ca^+-only pair with the same measurement uncertainty. This low sensitivity of the Ca^+-only pair is related to the high similarity of the electronic coefficients of the two Ca^+ transitions, as seen in Tab. 5.1. If included in Fig. 5.2 (a), these two Ca^+ transitions would be indistinguishable in the presented format. Although the shifts are strong, no NL would be caused if the shift is equal in both axes of the KP.

All these lines exhibit peaks at certain m_Φ. These peaks are caused by the coefficients X at these m_Φ, where the exception $X_2 - \frac{F_2}{F_1} X_1 = 0$ is fulfilled, which results in no NLs, as mentioned in chapter 2.3.2. However, this single point-happenstance can be overcome by a KP of different transitions, which exhibit this singularity at a different m_Φ.

As mentioned in chapter 2.3.4, a QMS of 3 Hz is expected in calcium [103]. This will cause also an NL in the KP and effectively make it more difficult to extract the fifth force contribution. Thus, the sensitivity will reduced, because the fifth force must exhibit a stronger coupling to overcome it, which is shown in Fig. 5.4 as a brown dash-dotted line. For the Ca_a^{14+}, Ca^{15+} transition pair, this would require the fifth force to be an order of magnitude stronger, thus lowering the sensitivity accordingly.

Using the GKP and combining three transitions of Ca^{15+}, Ca^{14+} and Ca^+ resulted in a GKP that spans a plane including the QMS. A fifth force would cause a deviation from that plane, thus restoring the sensitivity. This is shown as a solid blue line, which almost reaches force strengths down to $y_e y_n = 10^{-14}$.

Overall, in calcium measurements, the sensitivity can be improved from the previous Ca IS study from Ref. [40] by five orders of magnitude using more sensitive transitions and taking full advantage of the low predicted uncertainty of the QLS method. A QMS can be compensated for, and, due to the low mass of Ca, the next higher-order would be at much lower energies.

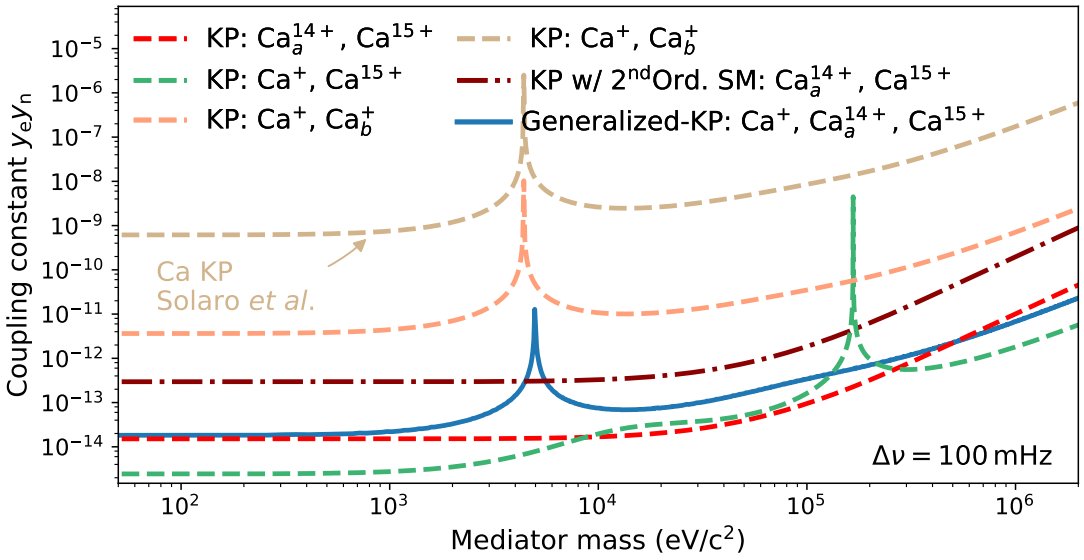

Figure 5.4: Exclusion plot in a few transitions-pairs with the best possible sensitivity. Added the Ca^+ transition pair used in Solaro et al. [40]. The Ca_b^+ is the 732 nm transition, while without subscript it is the 729 nm transition.

5.2.2 Xenon exclusion plot

The expected IS was slightly lower in Xe than in Ca, as discussed in chapter 5.1.2, however, Xe not only has more neutrons in the nucleus for the electron to couple to, but also has seven stable and even isotopes. The latter can be used to compensate for effects of up to three different higher-orders of the SM.

An exclusion plot for Xe transitions is depicted in Fig 5.5. As in the previous section, the latest calcium IS study from Ref. [40] was added as reference as a dark-yellow dashed line, and scaled down for a 100 mHz measurement uncertainty. A number of transition-pairs achieved similar sensitivities within classical KP without any higher-order SM contributions and neglected isotope mass uncertainties. One of those lines is shown as a dashed line at around $y_e y_n = 10^{-14}$. Considering the current Xe isotope masses, as shown in Tab. 1.2 [72], the sensitivity was reduced by three orders of magnitude (not shown). Higher-order SM shifts were introduced in chapter 2.3.4, in which it was discussed how QFS effects scale with nuclear charge. Hence a visible QFS NL is expected for elements with masses similar to that of Xe. However, currently no calculations of such an QFS can be found for Xe. To estimate the strength of this effect based on other elements, a QFS of ≈ 1 kHz [103] may occur. Such an effect would lead to the loss of another order of magnitude of sensitivity, shown in Fig 5.5 as the yellow dash-dotted line.

To overcome both the mass uncertainty and the QFS shift, a NmGKP was applied (see chapter 2.3.5). Here, four transitions are used together to substitute each of the nuclear parameters. This formed a 3D volume from which deviations were caused

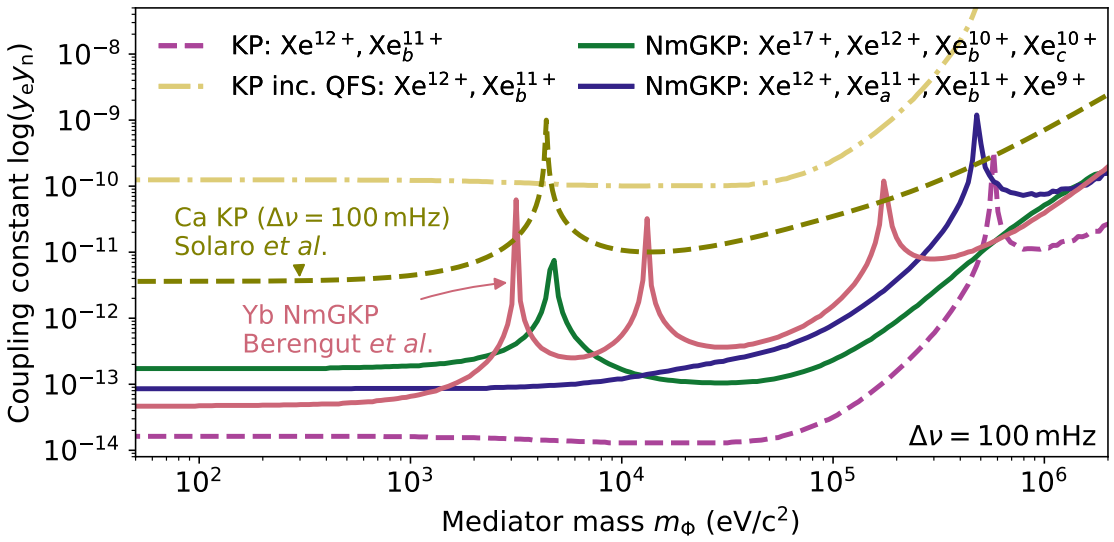

Figure 5.5: Exclusion plot in a few example transitions. Added the Ca^+ transition pair used in Solaro et al. [40] and ytterbium from Berengut et al. [39].

by the fifth force. Two of the most sensitive pairs are shown as a solid green and a solid blue line. While the green line is less sensitive at low mediator masses, its main sensitivity can be found between $m_\Phi = 10^5$ eV and 10^6 eV.

Other higher-order SM effects are not as prominent. For example, from Ref. [103], an approximation for the QMS scales the effect with $(K\mu)^2$, which would lead to a QMS of about two orders smaller for Xe compared to Ca. The main contributor of this reduction is the $\mu = m_A^{-1} - m_{A_r}^{-1}$ mass parameter.

Ytterbium has been used as the model element to find fifth forces, thus it is important that Xe's sensitivity is comparable to Yb's sensitivity. To compare the same results, the proposed NmGKP in Ref. [39] with four transitions is plotted as a annotated solid red line. The magnitude of the overall sensitivity is similar between these NmGKPs, proving the validity of Xe as a candidate for the search of a fifth force. Moreover, Xe has the advantage of having seven stable even isotopes, while Yb only has five. Recent KP analysis of Yb revealed a shift by nuclear deformation [41, 101], which limits the search with Yb if an additional higher SM order becomes visible.

Overall, Xe shows more promise than Yb to detect a fifth force because of its less deformed nuclei and higher number of isotopes.

5.3 Comparison of exclusion plots

Comparing the sensitivities between calcium and xenon shows that calcium is slightly more sensitive to a fifth force than xenon. Calcium is preferred over Xe also because its lighter nucleus will exhibit smaller higher-order SM shifts. However, current

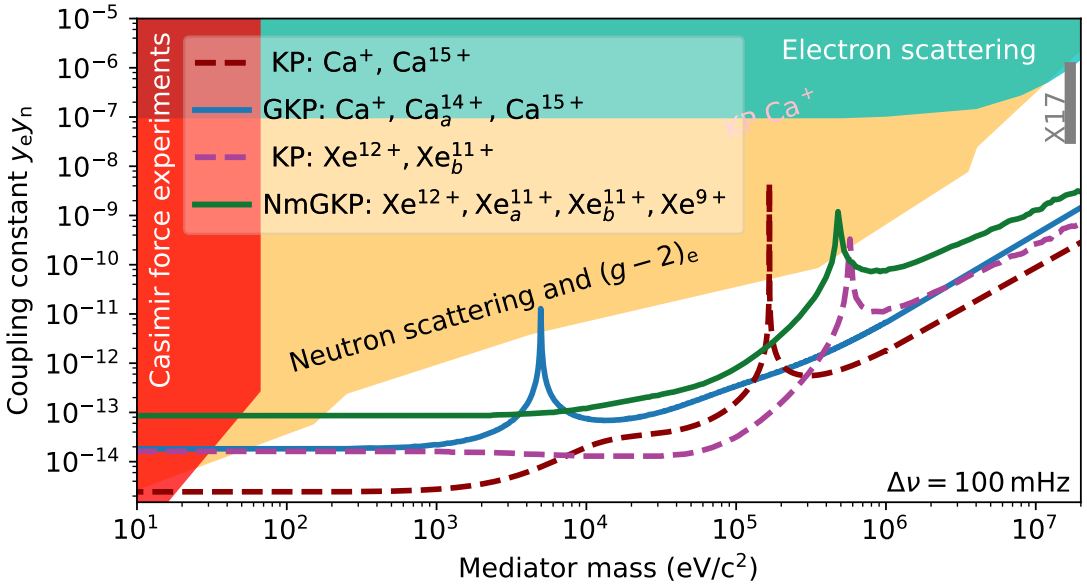

Figure 5.6: Exclusion plot with the pairs from Ca and Xe that have the highest sensitivity to a fifth force. The KPs are dashed lines, while the GKP are solid lines. Show here are also the excluded areas from other experiments, as discussed in chapter 2.2. Furthermore, the excluded area from the Ca^+ KP analysis from Ref. [40] is shown.

prediction includes a 3 Hz QMS [103], which must be compensated for by the only free isotope-pair calcium has. If unexpected higher-order effects are also visible in the given measurement uncertainty, or the uncertainty is reduced even further with new methods, then the limit of calcium is reached.

As stated, Xe with its number of available isotopes can compensate for up to three higher SM order shifts. This makes Xe a favored candidate as well. As shown, a QFS of 1 kHz and the isotope mass uncertainties can be overcome with pairings of the measured transitions.

Fig. 5.6 shows both the Ca and Xe results from their KP and GKP. The latest KP analysis in Ca from Ref [40] is shown as an excluded area, showing that it lies completely within the areas excluded by electron and neutron scattering experiments. With the current projected uncertainty of 100 mHz and the newly found transitions, the KP can probe the unrestricted NP parameter space. If the X17 anomaly is truly a NP boson, it would become visible in any of the predicted KP or GKP analyses.

Chapter 6

Summary

Dark matter is the collective ambiguous term for the numerous inexplicable phenomena in our universe, such as the rotational curve of galaxies, the neutrino masses, etc. It is evident that the current Standard Model (SM) of particle physics fails to provide an adequate explanation for dark matter, and therefore new efforts are put forth to establish a new physics model beyond the SM. A hypothetical fifth force has been proposed as key to substantiating this model and therefore understanding dark matter.

Such a fifth force is generally expressed by a Yukawa potential. Its main parameters are its coupling to existing particles and its interaction range. The latter is typically expressed as a mediator mass, where a larger mass poses a stronger limitation on coupling distance than a lighter mass. In the search for a fifth force, research efforts focus on the highly precise measurements of the atomic range of forces, as light masses are excluded by Casimir effect experiments and heavier masses are often indistinguishable from nuclear forces. It is particularly insightful to examine the fifth force interactions between electrons and neutrons as the electronic energy levels then vary between isotopes, and thus the fifth force can be observed as an isotope shift. However, SM isotope shifts, i.e. change of nuclear radius and mass, have to be compensated for. To do so, one can use the generalized King plot [37, 39], which can detect the fifth force as a deviation from a hyperplane spanned by multiple transitions and isotopes. This method also accounts for SM shifts that would disguise the fifth force contribution. Recent applications of this method were unfruitful as analysis was restricted by a range of factors, including poorly chosen transitions [40], deformed nuclei, and limited isotopes [41, 101]. Therefore, it is necessary to consider alternative elements as well as a broader selection of transitions in order to achieve higher sensitivity.

To this end, two candidates, calcium and xenon, were investigated, with the aim of laying the groundwork for the search for a fifth force with the generalized King plot method. Highly charged Ca and Xe were measured with fluorescence

spectroscopy and their ground-state transitions identified. These are necessary in the use of highly precise quantum logic spectroscopy (QLS) [66], which already achieves 100 mHz measurement precision [63] in highly charged ions (HCIs). It is planned to use this method to analyze future measured isotope shifts in collaboration with e.g. the PTB in Braunschweig.

The first element measured was calcium ($Z = 20$), which has five stable isotopes without nuclear spin. Calcium is a light element and thus has weaker nuclear effects that could hinder the discovery of a fifth force in the King plot. The highest expected contribution of a second-order SM shift is the quadratic mass-shift for Ca^+ of about 3 Hz, which would be within the predicted measurement uncertainty of 100 mHz. Other effects, like quadratic field-shift and nuclear polarizability, are lower than 10 mHz [103]. The latest King plot analysis of measured isotope shifts was performed with a 20 Hz measurement uncertainty [40], where no deviations in the King plot occurred. It was later revealed that the chosen transitions did not convey a good sensitivity to a fifth force [F1] due to their high similarity. Measurements included four M1 ground-state transitions in Ca. A theoretical analysis was conducted to reveal the best transitions for high sensitivity with a King plot. The result concluded that the best sensitivity can be achieved by combining ground-state transitions in Ca^+, Ca^{14+}, and Ca^{15+}. Compared to the previous Ca King-plot analysis, this predicts an improvement by four orders of magnitude, which also compensates for the effect of the quadratic mass-shift. Currently, QLS measurements of these transitions for the four available Ca isotopes are underway at the PTB in Braunschweig.

The second element measured was xenon ($Z = 54$), which has seven stable, even isotopes. As no optical ground-state transitions were listed in the NIST database [45], a more in-depth investigation was required. Similar to the Ca measurement, in-EBIT optical fluorescence spectroscopy was performed, however, this also included a scan of charge states Xe^{9+} through Xe^{33+}, where ground-state transitions were only found in seven of these charge states. The measurement resulted in thirteen ground-state transitions, where one is an ultra-narrow electric quadrupole (E2) transition. This transition has a natural linewidth of 0.3 mHz and is thus a potential atomic clock candidate [F2]. Higher-order SM isotope shift contributions are expected to be stronger in xenon than in calcium. As no calculations were previously performed for Xe, these shifts were approximated based on other elements [103]. Thus, a quadratic field-shift of 1 kHz was included in the analysis. Compared to Yb, Xe displays less nuclear deformation and consequently fewer prominent effects on isotope shifts. If nuclear deformation effects remain substantial in the isotope shift, the large number of Xe isotopes would allow for their compensation. The theoretical King plot analysis on Xe yielded a similar sensitivity to a fifth force compared to predictions in Yb. The

results showed that high sensitivity, small nuclear deformation, and an abundance of isotopes make Xe a promising candidate to consider for the search of a fifth force.

Altogether, the discovered ground-state transitions in Ca and Xe would improve the current limit of the parameter space of a fifth force by multiple orders of magnitude. The expected measurement uncertainty of at least 100 mHz by QLS predicts a substantial improvement compared to previous isotope shift measurements of at least four orders of magnitude. This level of sensitivity also covers an observed anomaly, called the X17. While the King plot analysis can be impeded by less known isotope masses and higher-order SM effects, these challenges can be overcome in the generalized King plot with the number of found transitions and available isotopes in these elements. This shows that measuring these isotope shifts and performing KP analysis can bring us a step closer to finding proof of a hypothetical fifth force and subsequently an New Physics model beyond the SM.

Chapter 7

Outlook

While this thesis focuses on the ground-state transitions of highly charged Ca and Xe, the implications of these findings extend across other related areas. This chapter will detail how endeavors of searching for a fifth force can also advance our understanding in metrology and nuclear physics.

7.1 Calcium and Xenon EUV

The theme of this work was on optical ground-state transitions, however, these are typically only found in lower charge states in HCIs. Probing higher charge states would expose the innermost electrons, which, due to their proximity to the nucleus, would experience a stronger effect by a fifth force. Furthermore, none of the observed transitions in this work were in s-orbitals. Because such orbitals have a wavefunction with a greater overlap with the nucleus, they experience a stronger effect, compared to their p-orbital counterparts.

In calcium, two of such EUV transitions are shown in Fig. 7.1 with their fifth force $\mathrm{IS}_{\mathrm{NP}}$ for the ^{40}Ca, ^{44}Ca pair. It includes the optical transitions from this work as reference. In the EUV range, M1 and E1 dipole transitions exhibit very high transition rates due to the λ^{-3} scaling, thus resulting in very broad natural line widths. To achieve a comparable 100 mHz uncertainty in the QLS, only E2 transitions are considered. The transition rate for the shown Ca^{12+} and Ca^{16+} EUV ground-level transitions are between 30ms to nearly 1s. Both of them are transitioning between a S_0 and a P_2 state. The stronger effect shown by the Ca^{16+} EUV transition is a direct result of the electron's proximity to the nucleus.

For xenon, the NP electronic coefficient X for some EUV transition in Xe^{34+}, Xe^{42+} and Xe^{46+} is shown in Fig. 7.2. Some of the optical transitions from this work are shown for reference. As in calcium, the fifth force has a stronger influence on the EUV transitions, e.g. about a magnitude stronger in Xe^{34+} compared to the Xe^{16+}. Surprisingly, Xe^{46+}, which was expected to be much stronger in its sensitivity, was

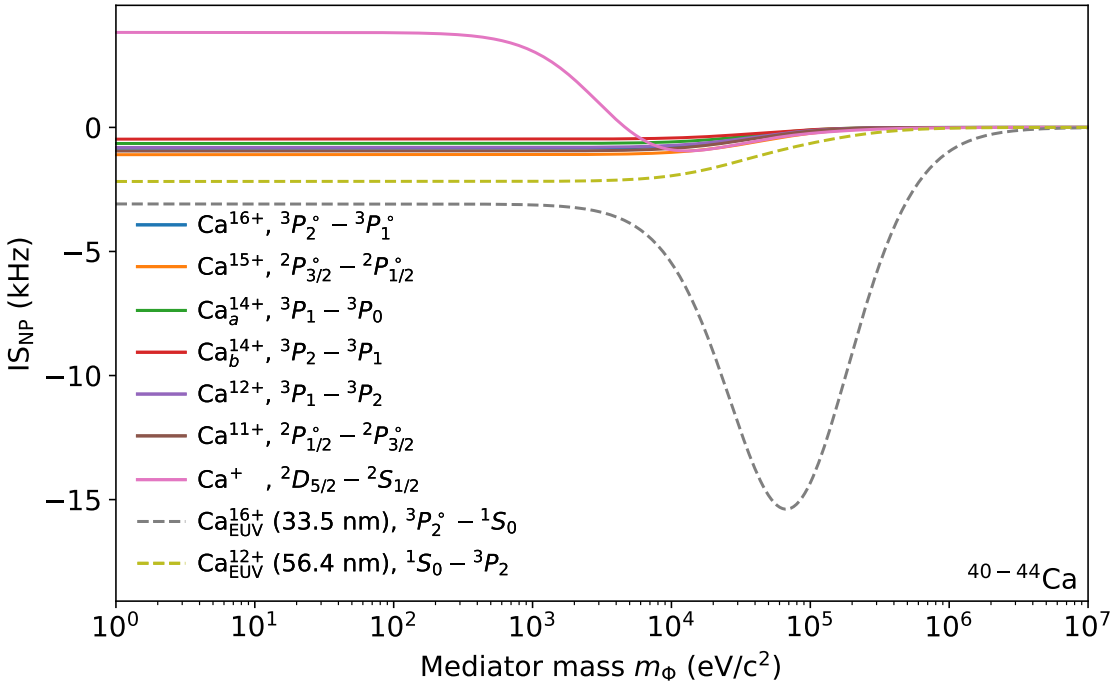

Figure 7.1: Comparison of predicted IS in the isotope pair of ^{40}Ca and ^{44}Ca between the optical and EUV transitions in calcium. Ca^{16+} transition shows a potentially strong sensitivity at 10^5eV/c^2.

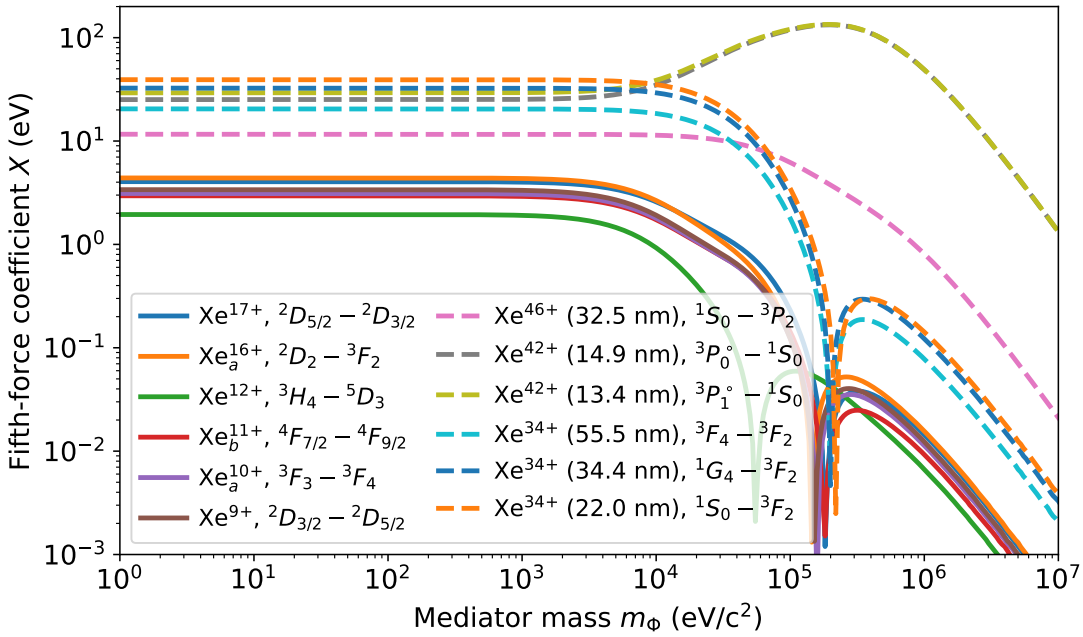

Figure 7.2: Comparison of the IS parameter $X(m_\Phi)$ of the fifth force between optical transitions investigated in this paper and prospective EUV transitions in Xe^{34+}, Xe^{42+} and Xe^{46+}. The shift is about an order of magnitude stronger in these EUV transitions than it is in the optical ones due to the higher charge state and therefore their closer proximity to the nucleus.

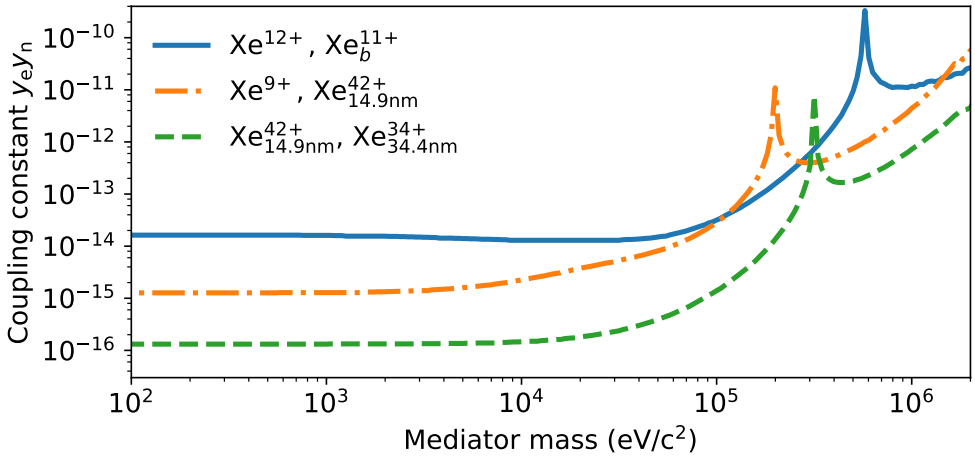

Figure 7.3: Exclusion plot for the most sensitive combinations of transitions in classical KPs with an assumed measurement uncertainty of 100 mHz. By going to higher charge states the electron is closer to the nucleus and therefore experiences a stronger shift by the fifth force. The sensitivity can thus be increased by multiple magnitudes. Solid lines are optical-only pairs, the dash-dotted line is optical-EUV pair and the dashed lines are EUV-only pairs.

not as strong as the other EUV transitions investigated, thus fortifying the need to perform these calculations and analyses prior measurements. An exclusion plot by classical KP analysis is shown in Fig. 7.3, which includes the most sensitive pairs from optical-optical, EUV-optical and EUV-EUV transition pairings. In the EUV-only pair, the resulting sensitivity was improved by two orders of magnitude, compared to the optical-only pair. While this seemed to be a direct result of the NP X coefficient, it should be stressed that the NL results from $X_2 - X_1 \cdot F_2/F_1$ from Eq. 2.28 and not from X alone. Several other EUV-pairs did not show such sensitivity.

While this prediction is worth pursuing, the major issue is the EUV range, which poses its own set of difficulties. EUV frequency combs offer a laser source [139, 140] for QLS, however, in the current state of acusto-optic modulator (AOM), the EUV light cannot be sufficiently adjusted to generate the red sideband pulses required for QLS. An expensive alternative to an AOM is to use multiple EUV frequency combs, which could be tuned to the energy of the red sideband pulse.

In the end it also comes down to how well the system can be controlled, states prepared and read out. For this a lot of work is required until it can be fully utilized. However, once this is overcome, the KP analysis would result in much higher sensitivity, compared to optical transitions.

7.2 Tin as King plot candidate

As introduced, Sn has as many stable even isotopes as Xe, and it has the advantage of the magical number of $Z = 50$. As shown in Fig. 2.8, no deformation was expected across its even isotopes. Sn has already been investigated in its level structure in Refs. [141, 142], however, no further analysis was conducted. The ground-level transitions of interest are summarized in Tab. 7.1 for reference. In this table, the same 4d-shell configurations have been measured as in the xenon measurement. A comparison of the ${}^2D_{5/2} - {}^2D_{3/2}$ transition in Sn^{13+} and Xe^{17+}, shows a wavelength shift from 758.8 nm in tin to 436.2 nm in xenon. This is a good example to see how the transitions shift with Q (see chapter 2.1.1). A shift by Q^2 is expected for energy levels, and thus for $17^2/13^2 = 1.7$ the Xe^{17+} 436.2 nm wavelength leads to an expected tin wavelength of 745.9 nm. This deviates from the measurement by 2% due to unaccounted QED shifts in this estimation, yet the tendency still holds true.

The IS by a fifth force IS_{NP} was calculated for Sn, and the resulting shift for different mediator masses is shown in Fig. 7.4. Compared to that of Xe in Fig. 5.3, the Sn shift strengths were slightly smaller due to the reduced number of neutrons. A direct comparison of the $4d^1$ transitions between Xe and Sn shows a difference in the shift by about 400 Hz for light mediator masses m_Φ. The comparable transitions in $4d^2$ through $4d^7$ show a similar deviation. The strongest shifts in Sn are by transitions that were not observed in Xe. This is because these Xe transitions lie in the far-UV spectrum, and thus beyond the scope of the conducted measurement. The SM K and F coefficients for MS and FS, as well as some key fifth force X coefficients, are summarized in Tab. 7.2. The comparison of the $4d^1$ transition between Sn^{13+} and Xe^{17+} shows that the NP X coefficient was reduced by nearly a factor of two, as was shown in the IS plot. This follows the same Q^2 scaling as in the wavelength, which is a factor $13^2/17^2 = 0.58$ from Xe to Sn.

Table 7.1: Summary of ground-state transitions in highly charged Sn ions [141, 142]: Measured energies and vacuum wavelengths λ_{vac}. Transition probabilities gA_{ki} were calculated with the COWAN code [120] and the calculated wavelengths $\lambda_{\text{CALC.}}$ were calculated with CI+MBPT.

			Observation	calculations		
Ion	Transition		λ_{vac} (nm)	$\lambda_{\text{calc.}}$(nm)	gA_{ki}(s^{-1})	Ref.
Sn^{7+}	$4d^7$	$^2G_{9/2}$ - $^4F_{9/2}$	441.9	444.0	262	[142]
Sn_a^{8+}	$4d^6$	$^3F_4$ - $^5D_4$	293.3	295.2	226	[142]
Sn_b^{8+}	$4d^6$	$^3F_3$ - $^5D_4$	315.0	315.4	60	[142]
Sn_c^{8+}	$4d^6$	$^3H_4$ - $^5D_4$	404.6	405.7	239	[142]
Sn_a^{9+}	$4d^5$	$^4G_{5/2}$ - $^6S_{5/2}$	261.0	262.9	304	[142]
Sn_b^{9+}	$4d^5$	$^4G_{5/2}$ - $^6S_{5/2}$	296.0	299.6	149	[142]
Sn_a^{11+}	$4d^3$	$^2D_{3/2}$ - $^4F_{3/2}$	275.6	276	102	[141]
Sn_b^{11+}	$4d^3$	$^4P_{3/2}$ - $^4F_{3/2}$	467.5	468	55	[141]
Sn^{12+}	$4d^2$	$^1D_2$ - $^3F_2$	402.6	402	117	[141]
Sn^{13+}	$4d^1$	$^2D_{5/2}$ - $^2D_{3/2}$	758.8	757	150	[141]

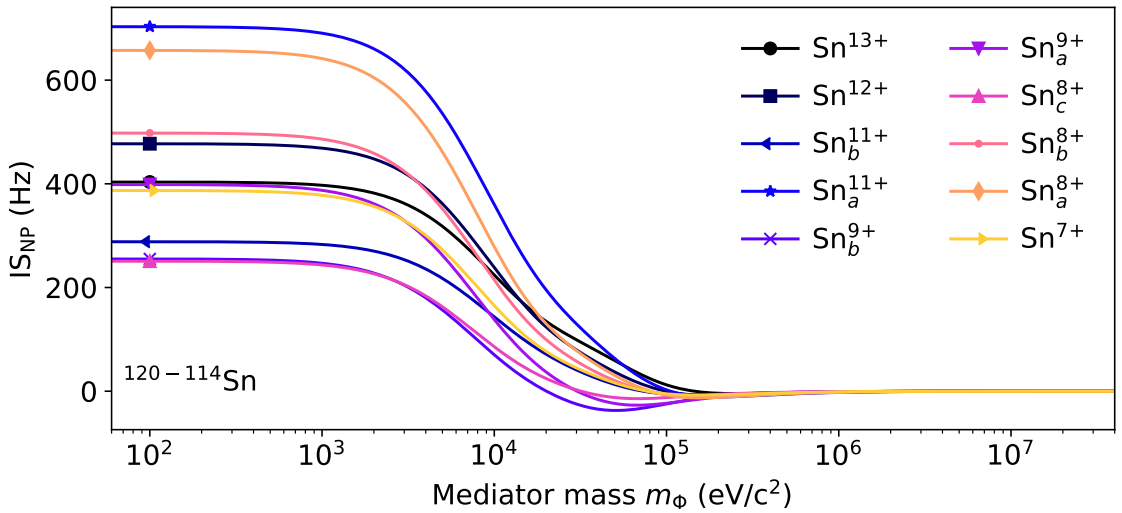

Figure 7.4: IS between ^{114}Sn and ^{120}Sn for the various previously measured Sn ground-state transitions from Refs. [141, 142]. The shifts are generally comparable in strength to those calculated in Xe, but the same transitions have a reduced shift.

Table 7.2: NP electronic coefficients X(m_Φ) in eV for different mediator masses m_Φ. The SM electronic coefficients K and F have been included as well. All of these values have been calculated with FAC.

	$X(m_\Phi)$ (eV)				SM coefficients	
Trans. \ m_Φ	$10^3\frac{\text{eV}}{\text{c}^2}$	$10^4\frac{\text{eV}}{\text{c}^2}$	$10^5\frac{\text{eV}}{\text{c}^2}$	$10^6\frac{\text{eV}}{\text{c}^2}$	K (eV·u)	F $\left(\frac{\text{eV}}{\text{fm}^2}\right)$
Sn^{7+}	2.61	1.14	-0.0354	-0.0087	-0.886×10^{-3}	465×10^{-9}
Sn_a^{8+}	4.42	1.92	-0.0526	-0.0140	-4.88×10^{-3}	772×10^{-9}
Sn_b^{8+}	3.35	1.47	-0.0428	-0.0113	-1.03×10^{-3}	628×10^{-9}
Sn_c^{8+}	1.68	0.590	-0.0856	-0.0056	-0.669×10^{-3}	299×10^{-9}
Sn_a^{9+}	2.67	0.953	-0.160	-0.0097	0.779×10^{-3}	531×10^{-9}
Sn_b^{9+}	1.70	0.484	-0.169	-0.0066	1.46×10^{-3}	382×10^{-9}
Sn_a^{11+}	4.76	2.48	0.0172	-0.0163	-1.06×10^{-3}	810×10^{-9}
Sn_b^{11+}	1.95	0.987	-0.0378	-0.0071	1.52×10^{-3}	365×10^{-9}
Sn^{12+}	3.23	1.64	-0.0019	-0.0108	-5.72×10^{-3}	601×10^{-9}
Sn^{13+}	2.74	1.54	0.0840	-0.0091	-2.66×10^{-3}	456×10^{-9}

7.3 Unstable isotopes

In the scope of this work, as well as all other considerations for KP analyses to date, only stable isotopes are being investigated. However, in principle, it would be possible to measure IS and construct KPs with isotopes with a half-life of a few minutes. For example, Xe has three more isotopes, ^{120}Xe, ^{122}Xe and ^{138}Xe, with half-lives longer than 15 min. Tin, with its seven stable even isotopes, has potentially four additional isotopes, ^{108}Sn, ^{110}Sn, ^{126}Sn, and ^{128}Sn, with half-lives of over 10 min. The half-lives of these isotopes are listed in Tab. 7.3. Calcium, unfortunately, does not have such minute-long half-life isotopes.

Xe		Sn	
Isotope	Half-life	Isotope	Half-life
^{120}Xe	40(1) min	^{108}Sn	10.30(8) min
^{122}Xe	20.1(1) h	^{110}Sn	4.11(10) h
^{138}Xe	14.08(8) min	^{126}Sn	$2.30(14)\times10^5$ y
		^{128}Sn	59.07(14) min

Table 7.3: Unstable even isotopes for Xe and Sn with half-lifes above 10 min.

The practicality of measuring unstable isotopes will ultimately depend on how fast the isotopes and their ground-states can be prepared before it decays. While

this would require more effort and careful planning, it offers the benefit of being able to compensate for more SM effects in the GKP.

7.4 Further E2 clock transitions

Clock transitions have their own field in metrology. The SI second has been defined by a hyperfine Cs transition [58], however, current atomic clocks can achieve magnitudes of higher precision [60, 59]. This definition of the second is thus a limiting factor when data is presented in SI seconds. Therefore it is expected that a different clock will redefine the SI unit. Notably, HCI clock candidates are sought after for this redefinition as they offer several advantages, e.g. stability, as discussed in chapter 2.1.1.

In this work, an ultra-narrow E2 transition was found in Xe^{10+}. Furthermore, Xe^{12+} and Xe^{16+} would also potentially offer such a transition, as AMBIT calculations showed (see Fig. 4.11, Tab. 4.5, and Tab. 4.6). The two Xe^{12+} E2 transitions may have similar lifetimes of $A_{ki} = 7 \times 10^{-4}\,\mathrm{s}^{-1}$ and $A_{ki} = 1 \times 10^{-4}\,\mathrm{s}^{-1}$ compared to the Xe^{10+} E2 transition with $A_{ki} = 2 \times 10^{-3}\,\mathrm{s}^{-1}$. However, Xe^{12+} contains a vast number of energy levels that require in-depth investigation and measurements to identify the transition wavelength.

In comparison, the E2 transition in Xe^{16+} with $A_{ki} = 1.05\,\mathrm{s}^{-1}$ is easier to find. It requires the measurement of a 955 nm M1 transition, which was out of the scope of our measurement setup. With an IR-camera instead of the current CCD detector, this may be measured without any significant foreseeable problems. It should also be noted that this investment can also benefit finding a similar E2 transition in Ge^{16+} [143], which has the same energy level structure. Here, a 1200 nm M1 transition has to be measured to obtain the E2 transition wavelength.

Ultimately, the investigation of Xe charge states led to a good set of ionic systems which can be utilized for future clocks. The found transitions would achieve even higher sensitivity to a fifth force than past measurements, and their prospective sensitivity in the EUV range can further propel this investigation of dark matter. As seen above, it is evident that the properties of isotopes and their shifts can be applied across multi-disciplinary fields and show much promise in advancing our understanding of our universe.

Acknowledgements

The completion of this thesis work would not have been possible without the immense support I received from everyone I worked with in the past four years. First and foremost, I would like to thank my PhD supervisor Prof. José Crespo for giving me this opportunity to dive into the realm of nuclear and atomic physics and to discover my strengths and research interests.

Secondly, I would like to extend my gratitude to the former and current members of the Crespo lab. I am particularly grateful to Dr. Hendrik Bekker, who initially set up the spectrometer before I started. I was fortunate to build on the preparations he lay down with the experiment as well as the basis of the scripts. I would also like to thank Michael Karl Rosner for teaching me the ways of the HD-EBIT as well as inspiring me with our many fruitful discussions. Naturally, I am indebted to him, Mark Botz, Lennart Guth, and Nick Lackmann for proofreading this thesis.

Thirdly, I am deeply thankful for the invaluable help and advice from our collaborators, Prof. Ming Feng Gu (University of California Berkeley) and Prof. Julian Berengut (University of New South Wales), on FAC and AMBIT analyses.

Last but most definitely not least, I would to thank my parents, Dagmar and Sönke Rehbehn, and my amazing partner and best friend, Lucy Zhao, for their unwavering support and unconditional love throughout my PhD.

Bibliography

First author publications

[F1] Nils-Holger Rehbehn et al. "Sensitivity to new physics of isotope-shift studies using the coronal lines of highly charged calcium ions". In: *Phys. Rev. A* 103 (4 Apr. 2021), p. L040801. DOI: 10.1103/PhysRevA.103.L040801.

[F2] Nils-Holger Rehbehn et al. "Narrow and ultra-narrow transitions in highly charged Xe ions as probes of fifth forces". In: *Submitted* (July 2023).

Co-author publications

[C1] Michael K. Rosner, Nils-Holger Rehbehn, and José R. Crespo López-Urrutia. "Experimental and theoretical Ritz-Rydberg analysis of the level structure of highly charged ions of lead and bismuth by optical spectroscopy". In: *in preparation* (2023).

Bibliography

[1] Lillian Hoddeson et al. *The rise of the standard model: A history of particle physics from 1964 to 1979*. Cambridge University Press, 1997.

[2] F. Abe et al. "Observation of Top Quark Production in $\overline{p}p$ Collisions with the Collider Detector at Fermilab". In: *Phys. Rev. Lett.* 74 (14 Apr. 1995), pp. 2626–2631. DOI: 10.1103/PhysRevLett.74.2626.

[3] K. Kodama et al. "Observation of tau neutrino interactions". In: *Physics Letters B* 504.3 (2001), pp. 218–224. ISSN: 0370-2693. DOI: 10.1016/S0370-2693(01)00307-0.

[4] Peter W. Higgs. "Broken Symmetries and the Masses of Gauge Bosons". In: *Phys. Rev. Lett.* 13 (16 Oct. 1964), pp. 508–509. DOI: 10.1103/PhysRevLett.13.508.

[5] G. Aad et al. "Observation of a new particle in the search for the Standard Model Higgs boson with the ATLAS detector at the LHC". In: *Physics Letters B* 716.1 (2012), pp. 1–29. ISSN: 0370-2693. DOI: 10.1016/j.physletb.2012.08.020.

[6] S. Chatrchyan et al. “Observation of a new boson at a mass of 125 GeV with the CMS experiment at the LHC”. In: *Physics Letters B* 716.1 (2012), pp. 30–61. ISSN: 0370-2693. DOI: 10.1016/j.physletb.2012.08.021.

[7] Wikimedia Commons, MissMJ, and Cush. *Standard Model of Elementary Particles*. File: Standard Model of Elementary Particles.svg. 2019. URL: https://en.wikipedia.org/wiki/File:Standard_Model_of_Elementary_Particles.svg.

[8] F Zwicky. “Die Rotverschiebung von extragalaktischen Nebeln”. In: *Helv. Phys. Acta* 6 (1933), p. 110.

[9] Sandra M Faber and JS Gallagher. “Masses and mass-to-light ratios of galaxies”. In: *Annual review of astronomy and astrophysics* 17.1 (1979), pp. 135–187.

[10] Y. Fukuda et al. “Evidence for Oscillation of Atmospheric Neutrinos”. In: *Phys. Rev. Lett.* 81 (8 Aug. 1998), pp. 1562–1567. DOI: 10.1103/PhysRevLett.81.1562.

[11] Hitoshi Murayama. “The origin of neutrino mass”. In: *Physics World* 15.5 (May 2002), p. 35. DOI: 10.1088/2058-7058/15/5/36. URL: https://dx.doi.org/10.1088/2058-7058/15/5/36.

[12] Christian Weinheimer and Kai Zuber. “Neutrino masses”. In: *Annalen der Physik* 525.8-9 (2013), pp. 565–575. DOI: 10.1002/andp.201300063.

[13] Gianfranco Bertone and Dan Hooper. “History of dark matter”. In: *Rev. Mod. Phys.* 90 (4 Oct. 2018), p. 045002. DOI: 10.1103/RevModPhys.90.045002.

[14] Yonit Hochberg et al. “New approaches to dark matter detection”. In: *Nature Reviews Physics* 4.10 (Oct. 2022), pp. 637–641. ISSN: 2522-5820. DOI: 10.1038/s42254-022-00509-4.

[15] The ATLAS Collaboration et al. “The ATLAS Experiment at the CERN Large Hadron Collider”. In: *Journal of Instrumentation* 3.08 (Aug. 2008), S08003. DOI: 10.1088/1748-0221/3/08/S08003.

[16] Biplob Bhattacherjee, Shigeki Matsumoto, and Rhitaja Sengupta. “Long-lived light mediators from Higgs boson decay at HL-LHC and FCC-hh, and a proposal of dedicated long-lived particle detectors for FCC-hh”. In: *Phys. Rev. D* 106 (9 Nov. 2022), p. 095018. DOI: 10.1103/PhysRevD.106.095018.

[17] E. Aprile et al. “The XENON1T dark matter experiment”. In: *The European Physical Journal C* 77.12 (Dec. 2017), p. 881. ISSN: 1434-6052. DOI: 10.1140/epjc/s10052-017-5326-3.

[18] E. Aprile et al. “Search for New Physics in Electronic Recoil Data from XENONnT”. In: *Phys. Rev. Lett.* 129 (16 Oct. 2022), p. 161805. DOI: 10.1103/PhysRevLett.129.161805.

[19] Max Aker et al. “First operation of the KATRIN experiment with tritium”. In: *The European Physical Journal C* 80.3 (Mar. 2020), p. 264. ISSN: 1434-6052. DOI: 10.1140/epjc/s10052-020-7718-z.

[20] M. Aker et al. “Direct neutrino-mass measurement with sub-electronvolt sensitivity”. In: *Nature Physics* 18.2 (Feb. 2022), pp. 160–166. ISSN: 1745-2481. DOI: 10.1038/s41567-021-01463-1.

[21] A. S. Barabash. "Experiment double beta decay: Historical review of 75 years of research". In: *Physics of Atomic Nuclei* 74.4 (Apr. 2011), pp. 603–613. ISSN: 1562-692X. DOI: 10.1134/S1063778811030070.

[22] M Auger et al. "The EXO-200 detector, part I: detector design and construction". In: *Journal of Instrumentation* 7.05 (2012), P05010.

[23] J. B. Albert et al. "Improved measurement of the $2\nu\beta\beta$ half-life of ^{136}Xe with the EXO-200 detector". In: *Phys. Rev. C* 89 (1 Jan. 2014), p. 015502. DOI: 10.1103/PhysRevC.89.015502.

[24] J. B. Albert et al. "Search for Neutrinoless Double-Beta Decay with the Upgraded EXO-200 Detector". In: *Phys. Rev. Lett.* 120 (7 Feb. 2018), p. 072701. DOI: 10.1103/PhysRevLett.120.072701.

[25] P. A. M. DIRAC. "The Cosmological Constants". In: *Nature* 139.3512 (Feb. 1937), pp. 323–323. ISSN: 1476-4687. DOI: 10.1038/139323a0.

[26] Jacob D. Bekenstein. "Fine-structure constant: Is it really a constant?" In: *Phys. Rev. D* 25 (6 Mar. 1982), pp. 1527–1539. DOI: 10.1103/PhysRevD.25.1527.

[27] John K. Webb et al. "Search for Time Variation of the Fine Structure Constant". In: *Phys. Rev. Lett.* 82 (5 Feb. 1999), pp. 884–887. DOI: 10.1103/PhysRevLett.82.884.

[28] V. A. Dzuba, V. V. Flambaum, and J. K. Webb. "Calculations of the relativistic effects in many-electron atoms and space-time variation of fundamental constants". In: *Phys. Rev. A* 59 (1 Jan. 1999), pp. 230–237. DOI: 10.1103/PhysRevA.59.230.

[29] Joerg Jaeckel and Sabyasachi Roy. "Spectroscopy as a test of Coulomb's law: A probe of the hidden sector". In: *Phys. Rev. D* 82 (12 Dec. 2010), p. 125020. DOI: 10.1103/PhysRevD.82.125020.

[30] Jonathan L. Feng et al. "Protophobic Fifth-Force Interpretation of the Observed Anomaly in ^{8}Be Nuclear Transitions". In: *Phys. Rev. Lett.* 117 (7 Aug. 2016), p. 071803. DOI: 10.1103/PhysRevLett.117.071803.

[31] Jonathan L. Feng et al. "Particle physics models for the 17 MeV anomaly in beryllium nuclear decays". In: *Phys. Rev. D* 95 (3 Feb. 2017), p. 035017. DOI: 10.1103/PhysRevD.95.035017.

[32] A. J. Krasznahorkay et al. "New anomaly observed in ^{12}C supports the existence and the vector character of the hypothetical X17 boson". In: *Phys. Rev. C* 106 (6 Dec. 2022), p. L061601. DOI: 10.1103/PhysRevC.106.L061601.

[33] Hooman Davoudiasl, Hye-Sung Lee, and William J. Marciano. "Muon Anomaly and Dark Parity Violation". In: *Phys. Rev. Lett.* 109 (3 July 2012), p. 031802. DOI: 10.1103/PhysRevLett.109.031802.

[34] Pavel Cejnar, Jan Jolie, and Richard F. Casten. "Quantum phase transitions in the shapes of atomic nuclei". In: *Rev. Mod. Phys.* 82 (3 Aug. 2010), pp. 2155–2212. DOI: 10.1103/RevModPhys.82.2155.

[35] V. A. Dzuba, V. V. Flambaum, and M. G. Kozlov. "Combination of the many-body perturbation theory with the configuration-interaction method". In: *Phys. Rev. A* 54 (5 Nov. 1996), pp. 3948–3959. DOI: 10.1103/PhysRevA.54.3948.

[36] W. H. King. "Comments on the Article "Peculiarities of the Isotope Shift in the Samarium Spectrum"". In: *J. Opt. Soc. Am.* 53.5 (May 1963), pp. 638–639. DOI: 10.1364/JOSA.53.000638.

[37] Kyoko Mikami, Minoru Tanaka, and Yasuhiro Yamamoto. "Probing new intra-atomic force with isotope shifts". In: *The European Physical Journal C* 77.12 (Dec. 2017), p. 896. ISSN: 1434-6052. DOI: 10.1140/epjc/s10052-017-5467-4.

[38] Claudia Frugiuele et al. "Constraining new physics models with isotope shift spectroscopy". In: *Phys. Rev. D* 96 (1 July 2017), p. 015011. DOI: 10.1103/PhysRevD.96.015011.

[39] Julian C. Berengut et al. "Generalized King linearity and new physics searches with isotope shifts". In: *Phys. Rev. Research* 2 (4 Dec. 2020), p. 043444. DOI: 10.1103/PhysRevResearch.2.043444.

[40] Cyrille Solaro et al. "Improved Isotope-Shift-Based Bounds on Bosons beyond the Standard Model through Measurements of the $^2D_{3/2} - {}^2D_{5/2}$ Interval in Ca^+". In: *Phys. Rev. Lett.* 125 (12 Sept. 2020), p. 123003. DOI: 10.1103/PhysRevLett.125.123003.

[41] Ian Counts et al. "Evidence for Nonlinear Isotope Shift in Yb^+ Search for New Boson". In: *Phys. Rev. Lett.* 125 (12 Sept. 2020), p. 123002. DOI: 10.1103/PhysRevLett.125.123002.

[42] Koki Ono et al. "Observation of Nonlinearity of Generalized King Plot in the Search for New Boson". In: *Phys. Rev. X* 12 (2 May 2022), p. 021033. DOI: 10.1103/PhysRevX.12.021033.

[43] Hirokazu Miyake et al. "Isotope-shift spectroscopy of the $^1S_0 \rightarrow {}^3P_1$ and $^1S_0 \rightarrow {}^3P_0$ transitions in strontium". In: *Phys. Rev. Research* 1 (3 Nov. 2019), p. 033113. DOI: 10.1103/PhysRevResearch.1.033113.

[44] B Ohayon et al. "Isotope shifts in cadmium as a sensitive probe for physics beyond the standard model". In: *New Journal of Physics* 24.12 (Dec. 2022), p. 123040. DOI: 10.1088/1367-2630/acacbb.

[45] Alexander Kramida et al. *NIST Atomic Spectra Database (ver. 5.7)*. Accessed: 2019-07-27. 2020. URL: https://www.nist.gov/pml/atomic-spectra-database.

[46] Morton A. Levine et al. "The Electron Beam Ion Trap: A New Instrument for Atomic Physics Measurements". en. In: *Physica Scripta* 1988.T22 (1988), p. 157. ISSN: 1402-4896. DOI: 10.1088/0031-8949/1988/T22/024. (Visited on 01/11/2017).

[47] M. A. Levine et al. "The use of an electron beam ion trap in the study of highly charged ions". In: *Nuclear Instruments and Methods in Physics Research Section B: Beam Interactions with Materials and Atoms* 43.3 (Sept. 1989), pp. 431–440. ISSN: 0168-583X. DOI: 10.1016/0168-583X(89)90386-8.

[48] M. G. Kozlov et al. “Highly charged ions: Optical clocks and applications in fundamental physics”. In: *Rev. Mod. Phys.* 90 (4 Dec. 2018), p. 045005. DOI: 10.1103/RevModPhys.90.045005.

[49] P. Micke et al. “The Heidelberg compact electron beam ion traps”. In: *Review of Scientific Instruments* 89.6 (June 2018), p. 063109. ISSN: 0034-6748. DOI: 10.1063/1.5026961.

[50] Matteo Barbarino. “A brief history of nuclear fusion”. In: *Nature Physics* 16.9 (Sept. 2020), pp. 890–893. ISSN: 1745-2481. DOI: 10.1038/s41567-020-0940-7.

[51] R. Betti. “A milestone in fusion research is reached”. In: *Nature Reviews Physics* 5.1 (Jan. 2023), pp. 6–8. ISSN: 2522-5820. DOI: 10.1038/s42254-022-00547-y.

[52] P Helander et al. “Stellarator and tokamak plasmas: a comparison”. In: *Plasma Physics and Controlled Fusion* 54.12 (Nov. 2012), p. 124009. DOI: 10.1088/0741-3335/54/12/124009.

[53] Allen H. Boozer. “Stellarator design”. In: *Journal of Plasma Physics* 81.6 (2015), p. 515810606. DOI: 10.1017/S0022377815001373.

[54] S Ratynskaia, L Vignitchouk, and P Tolias. “Modelling of dust generation, transport and remobilization in full-metal fusion reactors”. In: *Plasma Physics and Controlled Fusion* 64.4 (Feb. 2022), p. 044004. DOI: 10.1088/1361-6587/ac4b94.

[55] P Beiersdorfer. “Highly charged ions in magnetic fusion plasmas: research opportunities and diagnostic necessities”. In: *Journal of Physics B: Atomic, Molecular and Optical Physics* 48.14 (May 2015), p. 144017. DOI: 10.1088/0953-4075/48/14/144017.

[56] Steffen Kühn et al. “New Measurement Resolves Key Astrophysical Fe XVII Oscillator Strength Problem”. In: *Phys. Rev. Lett.* 129 (24 Dec. 2022), p. 245001. DOI: 10.1103/PhysRevLett.129.245001.

[57] Th. Udem, R. Holzwarth, and T. W. Hänsch. “Optical frequency metrology”. In: *Nature* 416.6877 (Mar. 2002), pp. 233–237. ISSN: 1476-4687. DOI: 10.1038/416233a.

[58] Barry N Taylor. “The current SI seen from the perspective of the proposed new SI”. In: *Journal of Research of the National Institute of Standards and Technology* 116.6 (2011), p. 797.

[59] B. J. Bloom et al. “An optical lattice clock with accuracy and stability at the 10^{-18} level”. In: *Nature* 506.7486 (Feb. 2014), pp. 71–75. ISSN: 1476-4687. DOI: 10.1038/nature12941.

[60] S. M. Brewer et al. “$^{27}Al^{+}$ Quantum-Logic Clock with a Systematic Uncertainty below 10^{-18}”. In: *Phys. Rev. Lett.* 123 (3 July 2019), p. 033201. DOI: 10.1103/PhysRevLett.123.033201.

[61] Barontini, G. et al. “Measuring the stability of fundamental constants with a network of clocks”. In: *EPJ Quantum Technol.* 9.1 (2022), p. 12. DOI: 10.1140/epjqt/s40507-022-00130-5.

[62] I Martinson. "The spectroscopy of highly ionised atoms". In: *Reports on Progress in Physics* 52.2 (Feb. 1989), p. 157. DOI: 10.1088/0034-4885/52/2/002.

[63] P. Micke et al. "Coherent laser spectroscopy of highly charged ions using quantum logic". In: *Nature* 578.7793 (Feb. 2020), pp. 60–65. ISSN: 1476-4687. DOI: 10.1038/s41586-020-1959-8.

[64] Steven A. King et al. "An optical atomic clock based on a highly charged ion". In: *Nature* 611.7934 (Nov. 2022), pp. 43–47. ISSN: 1476-4687. DOI: 10.1038/s41586-022-05245-4.

[65] D. J. Wineland et al. "Quantum computers and atomic clocks". In: *Frequency Standards and Metrology*, pp. 361–368. DOI: 10.1142/9789812777713_0040.

[66] P. O. Schmidt et al. "Spectroscopy Using Quantum Logic". In: *Science* 309.5735 (2005), pp. 749–752. ISSN: 0036-8075. DOI: 10.1126/science.1114375.

[67] Steven A. King et al. "Algorithmic Ground-State Cooling of Weakly Coupled Oscillators Using Quantum Logic". In: *Phys. Rev. X* 11 (4 Dec. 2021), p. 041049. DOI: 10.1103/PhysRevX.11.041049.

[68] Peter Micke. "Quantum Logic Spectroscopy of Highly Charged Ions". PhD Thesis. Gottfried Wilhelm Leibniz Universität, Hannover, 2020. URL: https://hdl.handle.net/21.11116/0000-0009-4A6B-D.

[69] P. D. Cottle and K. W. Kemper. "Persistence of the $N = 28$ shell closure in neutron-rich nuclei". In: *Phys. Rev. C* 58 (6 Dec. 1998), pp. 3761–3762. DOI: 10.1103/PhysRevC.58.3761.

[70] T. Iida et al. "The CANDLES experiment for the study of Ca-48 double beta decay". In: *Nuclear and Particle Physics Proceedings* 273-275 (2016). 37th International Conference on High Energy Physics (ICHEP), pp. 2633–2635. ISSN: 2405-6014. DOI: 10.1016/j.nuclphysbps.2015.10.013.

[71] Commission on Isotopic Abundances and Atomic Weights (CIAAW). *Calcium*. Accessed: 2023-07-24. 2015. URL: https://ciaaw.org/calcium.htm.

[72] John R. de Laeter et al. In: *Pure and Applied Chemistry* 75.6 (2003), pp. 683–800. DOI: 10.1351/pac200375060683.

[73] I. Angeli and K.P. Marinova. "Table of experimental nuclear ground state charge radii: An update". In: *Atomic Data and Nuclear Data Tables* 99.1 (2013), pp. 69–95. ISSN: 0092-640X. DOI: 10.1016/j.adt.2011.12.006.

[74] Jens Dilling et al. "Penning-Trap Mass Measurements in Atomic and Nuclear Physics". In: *Annual Review of Nuclear and Particle Science* 68.1 (2018), pp. 45–74. DOI: 10.1146/annurev-nucl-102711-094939.

[75] I. Angeli and K.P. Marinova. "Table of experimental nuclear ground state charge radii: An update". In: *Atomic Data and Nuclear Data Tables* 99.1 (2013), pp. 69–95. ISSN: 0092-640X. DOI: 10.1016/j.adt.2011.12.006.

[76] Commission on Isotopic Abundances and Atomic Weights (CIAAW). *Xenon*. Accessed: 2023-07-24. 2015. URL: https://ciaaw.org/xenon.htm.

[77] Hermann Haken and Hans Christoph Wolf. *Atom-und Quantenphysik: Einführung in die experimentellen und theoretischen Grundlagen*. Springer Berlin Heidelberg, 2013. DOI: 10.1007/978-3-642-98110-4.

[78] Wolfgang Demtröder. *Experimentalphysik 3: Atome, Moleküle und Festkörper*. Springer Berlin Heidelberg, 2016. ISBN: 978-3-662-49094-5. DOI: 10.1007/978-3-662-49094-5.

[79] J. D. Gillaspy. "Highly charged ions". In: *Journal of Physics B: Atomic, Molecular and Optical Physics* 34.19 (2001), R93. ISSN: 0953-4075. DOI: 10.1088/0953-4075/34/19/201. (Visited on 01/15/2017).

[80] J. C. Berengut et al. "Highly charged ions with $E1$, $M1$, and $E2$ transitions within laser range". In: *Phys. Rev. A* 86 (2 Aug. 2012), p. 022517. DOI: 10.1103/PhysRevA.86.022517.

[81] Jeremy Tatum. *Stellar Atmospheres*. LibreTexts, 2022. URL: https://phys.libretexts.org/Bookshelves/Astronomy__Cosmology/Stellar_Atmospheres_(Tatum)/09%3A_Oscillator_Strengths_and_Related_Topics/9.05%3A_Line_Strength.

[82] Wolfgang Demtröder. *Experimentalphysik 2: Elektrizität und Optik*. Springer Berlin Heidelberg, 2013. ISBN: 978-3-662-06967-7. DOI: 10.1007/978-3-662-06967-7.

[83] Walter Weizel. *Lehrbuch der Theoretischen Physik: Zweiter Band: Struktur der Materie*. Springer-Verlag, 1958.

[84] Alan Corney. *Atomic and Laser Spectroscopy*. Oxford University Press, Oct. 2006. ISBN: 9780199211456. DOI: 10.1093/acprof:oso/9780199211456.001.0001.

[85] E.V. Kahl and J.C. Berengut. "ambit: A programme for high-precision relativistic atomic structure calculations". In: *Computer Physics Communications* 238 (2019), pp. 232–243. ISSN: 0010-4655. DOI: 10.1016/j.cpc.2018.12.014.

[86] M F Gu. "The flexible atomic code". In: *Canadian Journal of Physics* 86.5 (2008), pp. 675–689. DOI: 10.1139/p07-197.

[87] Karl-Heinz Gericke. *Molecular Spectroscopy, TU Braunschweig*. Accessed: 2023-07-30. 2023. URL: http://www.pci.tu-bs.de/aggericke/PC4e/Kap_III/Linienbreite.htm.

[88] Thorlabs. *UV-Enhanced Aluminum Mirrors*. (accessed: 2023-08-27). 2023. URL: https://www.thorlabs.de/newgrouppage9.cfm?objectgroup_id=12393.

[89] D A Varshalovich, A N Moskalev, and V K Khersonskii. *Quantum Theory of Angular Momentum*. World Scientific, 1988. DOI: 10.1142/0270.

[90] M. Bordag, U. Mohideen, and V.M. Mostepanenko. "New developments in the Casimir effect". In: *Physics Reports* 353.1 (2001), pp. 1–205. ISSN: 0370-1573. DOI: 10.1016/S0370-1573(01)00015-1.

[91] Stephen L. Adler, Roger F. Dashen, and S. B. Treiman. "Comments on proposed explanations for the muonic-atom x-ray discrepancy". In: *Phys. Rev. D* 10 (11 Dec. 1974), pp. 3728–3735. DOI: 10.1103/PhysRevD.10.3728.

[92] D. Hanneke, S. Fogwell Hoogerheide, and G. Gabrielse. "Cavity control of a single-electron quantum cyclotron: Measuring the electron magnetic moment". In: *Phys. Rev. A* 83 (5 May 2011), p. 052122. DOI: 10.1103/PhysRevA.83.052122.

[93] Céline Bœhm and Joseph Silk. "A new test for dark matter particles of low mass". In: *Physics Letters B* 661.4 (2008), pp. 287–289. ISSN: 0370-2693. DOI: 10.1016/j.physletb.2008.02.019.

[94] R. Barbieri and T.E.O. Ericson. "Evidence against the existence of a low mass scalar boson from neutron-nucleus scattering". In: *Physics Letters B* 57.3 (1975), pp. 270–272. ISSN: 0370-2693. DOI: 10.1016/0370-2693(75)90073-8.

[95] Helmut Leeb and Jörg Schmiedmayer. "Constraint on hypothetical light interacting bosons from low-energy neutron experiments". In: *Phys. Rev. Lett.* 68 (10 Mar. 1992), pp. 1472–1475. DOI: 10.1103/PhysRevLett.68.1472.

[96] Yu. N. Pokotilovski. "Constraints on new interactions from neutron scattering experiments". In: *Physics of Atomic Nuclei* 69.6 (June 2006), pp. 924–931. ISSN: 1562-692X. DOI: 10.1134/S1063778806060020.

[97] V. V. Nesvizhevsky, G. Pignol, and K. V. Protasov. "Neutron scattering and extra-short-range interactions". In: *Phys. Rev. D* 77 (3 Feb. 2008), p. 034020. DOI: 10.1103/PhysRevD.77.034020.

[98] William Holland King. *Isotope shifts in atomic spectra*. Springer Science & Business Media, 2013.

[99] C W P Palmer. "Reformulation of the theory of the mass shift". In: *Journal of Physics B: Atomic and Molecular Physics* 20.22 (Nov. 1987), p. 5987. DOI: 10.1088/0022-3700/20/22/011.

[100] Saleh O. Allehabi et al. "Using isotope shift for testing nuclear theory: The case of nobelium isotopes". In: *Phys. Rev. C* 102 (2 Aug. 2020), p. 024326. DOI: 10.1103/PhysRevC.102.024326.

[101] Saleh O. Allehabi et al. "Nuclear deformation as a source of the nonlinearity of the King plot in the Yb^+ ion". In: *Phys. Rev. A* 103 (3 Mar. 2021), p. L030801. DOI: 10.1103/PhysRevA.103.L030801.

[102] V. A. Yerokhin et al. "Nonlinear isotope-shift effects in Be-like, B-like, and C-like argon". In: *Phys. Rev. A* 101 (1 Jan. 2020), p. 012502. DOI: 10.1103/PhysRevA.101.012502.

[103] V. V. Flambaum, A. J. Geddes, and A. V. Viatkina. "Isotope shift, nonlinearity of King plots, and the search for new particles". In: *Phys. Rev. A* 97 (3 Mar. 2018), p. 032510. DOI: 10.1103/PhysRevA.97.032510.

[104] Shuichiro Ebata and Takashi Nakatsukasa. "Octupole deformation in the nuclear chart based on the 3D Skyrme Hartree–Fock plus BCS model". In: *Physica Scripta* 92.6 (May 2017), p. 064005. DOI: 10.1088/1402-4896/aa6c4c.

[105] N. L. Figueroa et al. "Precision Determination of Isotope Shifts in Ytterbium and Implications for New Physics". In: *Phys. Rev. Lett.* 128 (7 Feb. 2022), p. 073001. DOI: 10.1103/PhysRevLett.128.073001.

[106] H.J. Wollersheim. *Nuclear deformation and quadrupole moment, Simon Fraser University*. Accessed: 2023-08-01. 2011. URL: https://web-docs.gsi.de/~wolle/TELEKOLLEG/KERN/LECTURE/Fraser/L3.pdf.

[107] V. V. Flambaum et al. "Nuclear polarization effects in atoms and ions". In: *Phys. Rev. A* 103 (3 Mar. 2021), p. 032811. DOI: 10.1103/PhysRevA.103.032811.

[108] P. Munro-Laylim, V. A. Dzuba, and V. V. Flambaum. *Nuclear polarisation and relativistic effects contributions to King plot non-linearity*. 2021. arXiv: 2112.14313 [physics.atom-ph].

[109] Julian C. Berengut et al. "Probing New Long-Range Interactions by Isotope Shift Spectroscopy". In: *Phys. Rev. Lett.* 120 (9 Feb. 2018), p. 091801. DOI: 10.1103/PhysRevLett.120.091801.

[110] Henri Van Regemorter. "Rate of Collisional Excitation in Stellar Atmospheres." In: *Astrophysical Journal, vol. 136, p. 906* 136 (1962), p. 906.

[111] Wolfgang Lotz. "An empirical formula for the electron-impact ionization cross-section". In: *Zeitschrift für Physik* 206.2 (Apr. 1967), pp. 205–211. ISSN: 0044-3328. DOI: 10.1007/BF01325928.

[112] Sasha W. Epp. "Röntgen-Laserspektroskopie hochgeladener Ionen in einer EBIT am Freie-Elektronen-Laser FLASH". PhD Thesis. Ruprecht-Karls-Universität, Heidelberg, 2007. URL: http://www.ub.uni-heidelberg.de/archiv/7493.

[113] Erwin G Loewen. "Diffraction gratings, ruled and holographic". In: *Applied optics and optical engineering* 9 (2012), pp. 33–71.

[114] Thorlabs. *Reflective Holographic Gratings*. (accessed: 2023-09-03). 2023. URL: https://www.thorlabs.com/newgrouppage9.cfm?objectgroup_id=25.

[115] G. Breit. "Dirac's Equation and the Spin-Spin Interactions of Two Electrons". In: *Phys. Rev.* 39 (4 Feb. 1932), pp. 616–624. DOI: 10.1103/PhysRev.39.616.

[116] Joseph B Mann. *Atomic structure calculations. I. Hartree–Fock energy results for the elements hydrogen to lawrencium*. Tech. rep. Los Alamos National Lab.(LANL), Los Alamos, NM (United States), 1967.

[117] S. Fritzsche. "The Ratip program for relativistic calculations of atomic transition, ionization and recombination properties". In: *Computer Physics Communications* 183.7 (2012), pp. 1525–1559. ISSN: 0010-4655. DOI: 10.1016/j.cpc.2012.02.016.

[118] José R. Crespo López-Urrutia and Zoltán Harman. "Emission and Laser Spectroscopy of Trapped Highly Charged Ions in Electron Beam Ion Traps". In: *Fundamental Physics in Particle Traps*. Ed. by Wolfgang Quint and Manuel Vogel. Berlin, Heidelberg: Springer Berlin Heidelberg, 2014, pp. 315–373. ISBN: 978-3-642-45201-7. DOI: 10.1007/978-3-642-45201-7_10.

[119] Hendrik Bekker. "Optical and EUV spectroscopy of highly charged ions near the 4 f –5s level crossing." PhD Thesis. Ruprecht-Karls-Universität, Heidelberg, 2016. URL: https://hdl.handle.net/11858/00-001M-0000-002A-6CA5-5.

[120] Robert D Cowan. *The theory of atomic structure and spectra*. 3. Univ of California Press, 1981.

[121] Bertha Swirles. "The relativistic self-consistent field". In: *Proceedings of the Royal Society of London. Series A-Mathematical and Physical Sciences* 152.877 (1935), pp. 625–649.

[122] Irina L. Rusakova, Yurii Yu. Rusakov, and Leonid B. Krivdin. "Theoretical grounds of relativistic methods for calculation of spin – spin coupling constants in nuclear magnetic resonance spectra". In: *Russian Chemical Reviews* 85.4 (Apr. 2016), p. 356. DOI: 10.1070/RCR4561.

[123] J. R. Crespo López-Urrutia et al. "The Freiburg Electron Beam Ion Trap/-Source Project FreEBIT". In: *Physica Scripta* T80.B (1999), p. 502. DOI: 10.1238/physica.topical.080a00502.

[124] MPI für Kernphysik, Press release. *Helium recycling process successfully established*. (accessed: 2023-08-13). 2023. URL: https://www.mpi-hd.mpg.de/mpi/en/public-relations/news/news-item/default-980d19a127.

[125] Gabriel Herrmann. "Optical Theory of Thermal Velocity Effects in Cylindrical Electron Beams". In: *Journal of Applied Physics* 29.2 (June 2004), pp. 127–136. ISSN: 0021-8979. DOI: 10.1063/1.1723053.

[126] Alexander Windberger. "Identification of optical transitions in complex highly charged ions for applications in metrology and tests of fundamental constants." PhD Thesis. Ruprecht-Karls-Universität, Heidelberg, 2015. URL: https://hdl.handle.net/11858/00-001M-0000-0027-7978-8.

[127] McPherson Inc. *Datasheet for Model 2062 Czerny-Turner Monochromator*. (accessed: 2023-06-16). 2023. URL: https://www.mcphersoninc.com/pdf/2062.pdf.

[128] McPherson Inc. *Datasheet for Andor Newton CCD*. (accessed: 2023-06-17). 2023. URL: https://andor.oxinst.com/assets/uploads/products/andor/documents/andor-newton-ccd-specifications.pdf.

[129] J. F. Ziegler. "Terrestrial cosmic rays". In: *IBM Journal of Research and Development* 40.1 (1996), pp. 19–39. DOI: 10.1147/rd.401.0019.

[130] Albert J. P. Theuwissen. "Influence of Terrestrial Cosmic Rays on the Reliability of CCD Image Sensors—Part 1: Experiments at Room Temperature". In: *IEEE Transactions on Electron Devices* 54.12 (2007), pp. 3260–3266. DOI: 10.1109/TED.2007.908906.

[131] R. E. Marrs, S. R. Elliott, and D. A. Knapp. "Production and Trapping of Hydrogenlike and Bare Uranium Ions in an Electron Beam Ion Trap". In: *Phys. Rev. Lett.* 72 (26 June 1994), pp. 4082–4085. DOI: 10.1103/PhysRevLett.72.4082.

[132] E. D. Marquardt, J. P. Le, and Ray Radebaugh. "Cryogenic Material Properties Database". In: *Cryocoolers 11*. Ed. by R. G. Ross. Boston, MA: Springer US, 2002, pp. 681–687. ISBN: 978-0-306-47112-4. DOI: 10.1007/0-306-47112-4_84.

[133] Paul T Boggs and Janet E Rogers. "Orthogonal distance regression". In: *Contemporary mathematics* 112 (1990), pp. 183–194.

[134] Edson R. Peck and Kaye Reeder. "Dispersion of Air*". In: *J. Opt. Soc. Am.* 62.8 (Aug. 1972), pp. 958–962. DOI: 10.1364/JOSA.62.000958.

[135] S. Sturm et al. "g-factor measurement of hydrogenlike $^{28}Si^{13+}$ as a challenge to QED calculations". In: *Phys. Rev. A* 87 (3 Mar. 2013), p. 030501. DOI: 10.1103/PhysRevA.87.030501.

[136] European Machine Vision Association et al. "Standard for characterization of image sensors and cameras". In: *EMVA Standard* 1288 (2010). URL: https://www.emva.org/wp-content/uploads/EMVA1288-3.0.pdf.

[137] John T. Jefferies, Frank Q. Orrall, and J. B. Zirker. "The spectrum of the inner corona observed during the total solar eclipse of 30 May 1965". In: *Solar Physics* 16.1 (Jan. 1971), pp. 103–110. ISSN: 1573-093X. DOI: 10.1007/BF00154505.

[138] Strem Chemicals Ins. *Bis-Calcium, CAS 118448-18-3*. (accessed: 2023-07-07). 2023. URL: https://www.strem.com/catalog/v/20-1000/.

[139] Janko Nauta et al. "Towards precision measurements on highly charged ions using a high harmonic generation frequency comb". In: *Nucl. Instrum. Methods Phys. Res. B* 408 (2017). Proceedings of the 18th International Conference on the Physics of Highly Charged Ions (HCI-2016), Kielce, Poland, 11-16 September 2016, pp. 285–288. ISSN: 0168-583X. DOI: 10.1016/j.nimb.2017.04.077.

[140] J. Nauta et al. "XUV frequency comb production with an astigmatism-compensated enhancement cavity". In: *Opt. Express* 29.2 (Jan. 2021), pp. 2624–2636. DOI: 10.1364/OE.414987.

[141] A. Windberger et al. "Analysis of the fine structure of Sn^{11+} – –Sn^{14+} ions by optical spectroscopy in an electron-beam ion trap". In: *Phys. Rev. A* 94 (1 July 2016), p. 012506. DOI: 10.1103/PhysRevA.94.012506.

[142] F. Torretti et al. "Optical spectroscopy of complex open-4d-shell ions Sn^{7+} – –Sn^{10+}". In: *Phys. Rev. A* 95 (4 Apr. 2017), p. 042503. DOI: 10.1103/PhysRevA.95.042503.

[143] Saleh O. Allehabi et al. "High-accuracy optical clocks based on group-16-like highly charged ions". In: *Phys. Rev. A* 106 (4 Oct. 2022), p. 043101. DOI: 10.1103/PhysRevA.106.043101.

[144] J. R. Crespo López-Urrutia et al. "Visible Spectrum of Highly Charged Ions: the Forbidden Optical Lines of Kr, Xe, and Ba Ions in the Ar I to Ni I Isoelectronic Sequence". In: *Physica Scripta* T80.B (1999), p. 448. DOI: 10.1238/physica.topical.080a00448.

[145] C. A. Morgan et al. "Observation of Visible and uv Magnetic Dipole Transitions in Highly Charged Xenon and Barium". In: *Phys. Rev. Lett.* 74 (10 Mar. 1995), pp. 1716–1719. DOI: 10.1103/PhysRevLett.74.1716.

Appendix A

Xenon non-ground-state transitions

During this work, a number of Xe transitions were observed, which were irrelevant for the perspective QLS measurement and its search for a fifth force. The following tables contain over 120 xenon transitions, ranging from Xe^{7+} to Xe^{33+}. The energy scan, shown in Fig. A.1, ranged from cathode voltages of 350 V to 2500 V. For the lower range, please refer to Fig. 4.9.

Charge states below Xe^{9+} have to be taken cautiously, as these transitions were only visible by their 'tail', i.e. where their production in the EBIT ended. This complicated their charge state identification, as transitions in Xe^{7+} could as well be weaker Xe^{8+} transitions. While most transitions listed the the tables below were only measured within the energy scan, a few transitions were investigated with greater accuracy to obtain their Zeeman structure and acquire a better identification. Only successful identifications are shown. Occasionally, transitions were inferred from the NIST database [45], in particular their energy level database, which revealed transitions not listed in the transition database. While all transitions should be seen as preliminary identifications, some are noted with a '?' to indicate that they did not convincingly fall into the designated charge state groups. This may be due to their weak intensity, or due to the intermixing of two transitions of two neighboring charge states. In the tables below, relative intensities were taken from the pixel intensity of that line from the energy scan. It should be noted that the listed intensity does not account for any influences of the optical setup for the set wavelength.

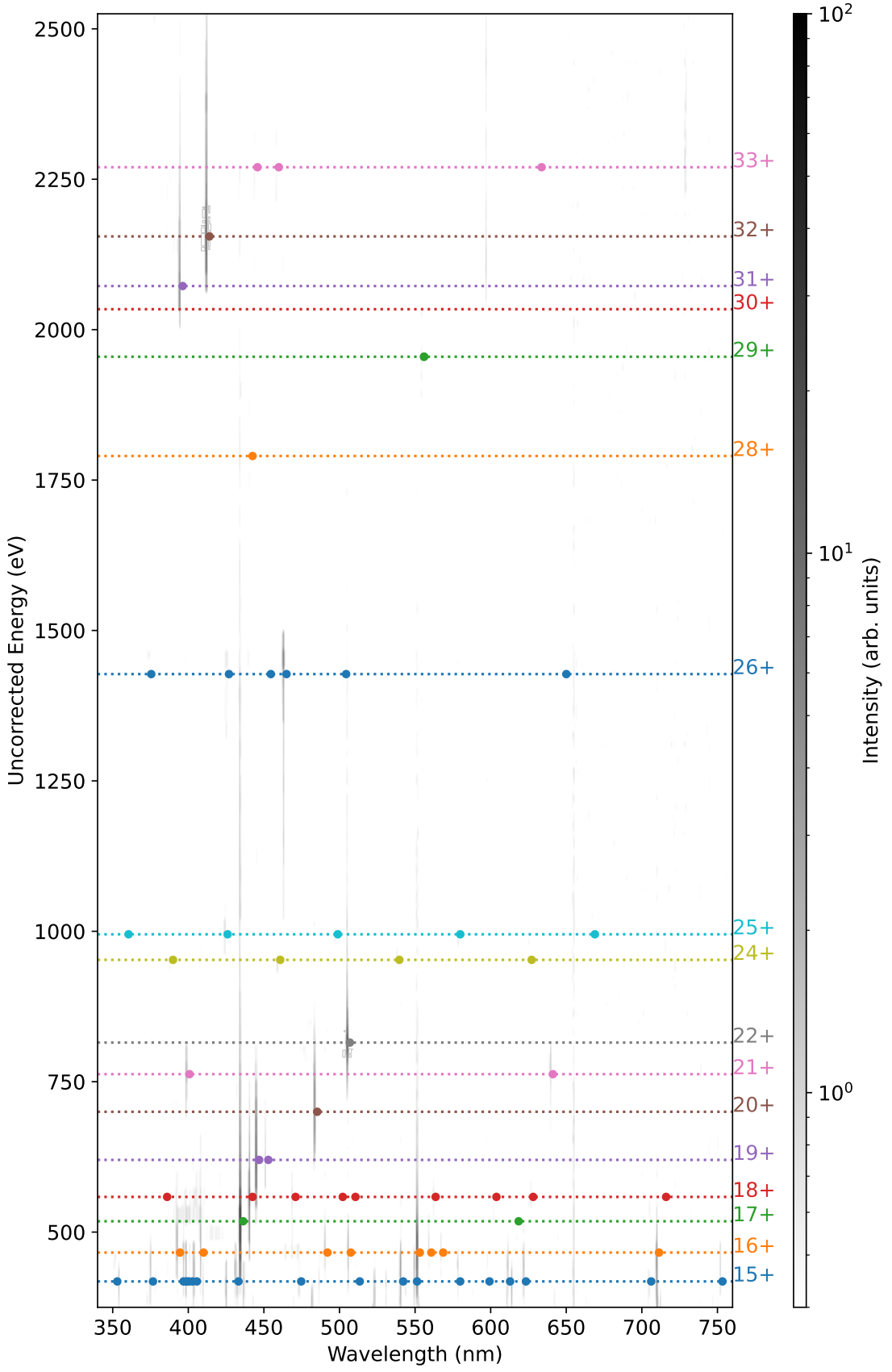

Figure A.1: Energy scan up to 2500 V. A focus on the lower energies can be found in Fig. 4.9

Table A.1: Summary of observed non-ground-state transitions in Xe. Wavelength λ_{air} is reported as measured in air. Relative intensities stem from the energy scan. Identified transitions have wavelengths λ_{FAC} by FAC and LS-notation. Some transitions were inferred from the energy levels in NIST [45].

	observation		FAC	
Ion	λ_{air} (nm)	rel. Int.	λ_{FAC} (nm)	Transition
7+?	335.17(6)	1.3		
7+?	364.70(4)	1.3		
7+?	641.16(2)	0.54		
7+?	640.95(2)	4.1		
7+?	756.17(11)	3.6		
8+	296.9232(31)	3.3		
8+	373.03(4)	2.2		
8+	430.8(3)	0.9		
8+	432.9(5)	1.6		
8+	493.6853(23)	1	490.01	$4d^9\,5s^1\ {}^1\mathrm{D}_2$-$^3\mathrm{D}_3$ (NIST: 499.6 nm)
8+?	534.34(1)	2.6	547.12	$4d^9\,4f^1\ {}^1\mathrm{H}_5$-$^3\mathrm{H}_6$
8+	581.9103(46)	1.9		
8+	605.3105(47)	2.6	605.01	$4d^9\,5s^1\ {}^1\mathrm{D}_2$-$^3\mathrm{D}_2$ (NIST: 604.6 nm)
8+	606.2233(26)	4		
8+	606.55894(58)	17.9		
8+	728.6(10)	1.7		
8+	764.06(9)	3	806.82	$4d^9\,5s^1\ {}^3\mathrm{D}_1$-$^3\mathrm{D}_2$ (NIST: 763.8 nm)
9+	491.3(3)	1.3	480.02	$4d^8\,4f^1\ {}^2\mathrm{I}_{13/2}$-$^4\mathrm{I}_{15/2}$
9+?	363.78(4)	1.19		

Table A.2: Continuation of summary of Xe transitions.

	observation		FAC	
Ion	λ_{air} (nm)	rel. Int.	λ_{FAC} (nm)	Transition
13+?	361.7(3)	0.64		
13+?	656.32(4)	1.9		
13+?	788.24(6)	0.95		
13+	269.9364(20)	1.8	247.49	$4d^5\ {}^2\mathrm{H}_{9/2}$-$^4\mathrm{G}_{9/2}$
13+	276.631(78)	0.5		
13+	277.0174(36)	1.14		
13+	278.4954(32)	1.14		
13+	306.2171(27)	1.5	326.46	$4d^5\ {}^2\mathrm{G}_{9/2}$-$^4\mathrm{G}_{11/2}$
13+	348.2309(14)	0.8		
13+	374.1864(23)	1.7	363.53	$4d^5\ {}^4\mathrm{F}_{7/2}$-$^4\mathrm{G}_{9/2}$
13+	375.78(4)	0.9	368.23	$4d^5\ {}^2\mathrm{I}_{13/2}$-$^4\mathrm{G}_{11/2}$
13+	396.7(5)	4.3		
13+	427.9(3)	1.2		
13+	444.75(12)	6.3		
13+	471.55(5)	4.9		
13+	477.9(4)	4.7		
13+	483.649(57)	23.1	465.29	$4d^5\ {}^2\mathrm{I}_{11/2}$-$^4\mathrm{G}_{11/2}$
13+	500.6(3)	2.8		
13+?	524.9314(90)	2.6		
13+	541.47(6)	2.7		
13+	543.69(8)	1.2		
13+	577.22(9)	1.6		
13+	578.95(8)	2.5		
13+	580.8(1)	0.94		
13+	589.41(7)	2.4		
13+	627.78(3)	1.8		
13+	643.6515(32)	3.9		
13+?	651.6(5)	0.63		
13+	680.74(7)	0.45		
13+	688.43(4)	0.78		
13+	699.17(6)	0.6		

Table A.3: Continuation of summary of Xe transitions.

	observation		FAC	
Ion	λ_{air} (nm)	rel. Int.	λ_{FAC} (nm)	Transition
14+?	270.929(67)	1.1		
14+	294.9764(30)	1.1	299.29	$4d^4\ {}^3\text{P}_0$-${}^5\text{D}_1$
14+	355.8924(28)	1.8		
14+	380.1956(49)	2.1		
14+	388.6(7)	1.7		
14+	411.94(9)	8		
14+	416.8(4)	0.9		
14+	418.8(3)	1.6		
14+	427.0(2)	18.9		
14+	434.6464(31)	15.8		
14+	438.79(15)	11.3		
14+	466.29(7)	3		
14+	475.1512(39)	1.3		
14+	488.0513(64)	5.9		
14+	532.45(7)	8.4	532.65	$4d^4\ {}^3\text{H}_4$-${}^5\text{D}_4$
14+	543.23(6)	2.2		
14+	545.48(4)	6.4		
14+	615.44(2)	15.8	620.29	$4d^4\ {}^3\text{D}_1$-${}^3\text{P}_2$
14+	714.075(9)	3.9	702.58	$4d^4\ {}^3\text{P}_1$-${}^3\text{P}_0$
14+	716.85(4)	0.9		
17+?	516.56(16)	1.4	484.09	$4p^5\,4d^2\ {}^2\text{G}_{9/2}$-${}^4\text{G}_{7/2}$
17+	618.51(4)	1.6	673.88	$4p^5\,4d^2\ {}^2\text{G}_{9/2}$-${}^2\text{F}_{7/2}$
18+	716.04(4)	0.75		
18+	502.16(24)	1.5		
18+	309.300(3)	1.2		
18+?	257.25(25)	1.5		
18+	603.82(4)	5.7		
18+	442.348(26)	74.2		
18+	563.6(1)	7.2		
18+	386.0(7)	1.5		
18+	470.95(9)	1.8		
18+	510.57(19)	2.2		
18+	628.11(2)	7.1		
19+?	313.253(6)	1.5		
19+	446.7839(16)	42.3	425.35	$4p^4\,4d^1\ {}^4\text{F}_{9/2}$-${}^4\text{D}_{7/2}$
19+	452.94(1)	4.3	387.12	$4p^4\,4d^1\ {}^2\text{F}_{7/2}$-${}^4\text{D}_{7/2}$
20+	485.2405(55)	10.8	504.64	$4s^1\,4p^5\,4d^1\ {}^5\text{D}_4$-${}^5\text{D}_3$

Table A.4: Continuation of summary of Xe transitions.

	observation		FAC	
Ion	λ_{air} (nm)	rel. Int.	λ_{FAC} (nm)	Transition
21+	320.59079(91)	1.12	309.68	$4s^1\,4p^4\ {}^4\text{F}_{9/2}$-$^4\text{F}_{7/2}$
21+	400.82(8)	3.1	357.97	$4p^3\ {}^2\text{D}_{5/2}$-$^2\text{D}_{3/2}$
22+	506.80653(15)	26.7	446.72	$4p^2\ {}^1\text{D}_2$-$^3\text{P}_1$
24+	389.9(5)	0.7		
24+	460.81(6)	0.76		
24+	539.6(5)	1.3		
24+	627.047(22)	0.58		
25+	360.5(5)	0.7		
25+	426.00(7)	1.2		
25+	498.9(5)	0.7		
25+	579.91(8)	0.52		
25+	668.94(9)	0.43		
26+	375.5(5)	0.7		
26+	426.9(5)	0.9		
26+	454.6(5)	0.8		
26+	464.891(30)	6.4		
26+	504.4(5)	0.4		
26+	650.05(5)	0.64		
28+	442.5(5)	0.2	352.94	$3d^8\ {}^3\text{P}_1$-$^3\text{P}_2$
29+	555.9(5)	0.4		
29+	556.00(4)	0.8		
29+	284.6(6)	2.8		
30+	262.0(5)	0.8	264.71	$3d^6\ {}^5\text{D}_3$-$^5\text{D}_2$
30+	301.7639(23)	2.6	288.89	$3d^6\ {}^3\text{G}_5$-$^3\text{H}_4$
31+	396.2096(16)	10.4	418.99	$3d^5\ {}^4\text{G}_{9/2}$-$^4\text{G}_{7/2}$ (396.2(2) nm [144, 145])
31+?	598.61(4)	1.3	558.77	$3d^5\ {}^4\text{G}_{9/2}$-$^4\text{G}_{11/2}$ (598.4(10) nm [144])
32+	413.8997(35)	21.9	397.38	$3d^4\ {}^5\text{D}_3$-$^5\text{D}_2$ (413.9(2) nm [144, 145])
32+?	689.96(9)	0.37		
32+	730.23(3)	1.4	690.01	$3d^4\ {}^3\text{H}_6$-$^3\text{H}_5$
33+			720.60	$3d^3\ {}^2\text{G}_{9/2}$-$^4\text{F}_{7/2}$
33+	445.7001(23)	0.76	421.31	$3d^3\ {}^4\text{P}_{1/2}$-$^4\text{P}_{3/2}$ (445.6(5) nm [144])
33+	459.9(5)	0.75		
33+	633.71(5)	0.65	649.86	$3d^3\ {}^2\text{F}_{7/2}$-$^2\text{F}_{5/2}$ (632.7(15) nm [144])

Appendix B

FAC: Calcium calculation

B1 Sample calculation and CRM

To calculate the energy levels and transitions, an easy and fast way is to use FAC [86]. Using FAC, the CRM can be made use of, which will result in an output of the brightest lines in comparison with each other, and may help in the identification process. Below is an example code of how to run FAC in the case of Ca^{14+}, where comments in green describe the code where applicable:

```
from pfac.fac import *

z=20 # Calcium
k=6 # 6 electrons in atom: Ca 14+
En=1000 # eV Energy for CRM

a = ATOMICSYMBOL[z]
SetAtom(a, z)
SetBreit(8,1)
SetSE(8,140)

pref='%s%02d'%(a,k) # name for output

if k <= 2: #set config with 2 or less electrons in the system
  Config('g0', '1s2','1s1 2*%d'%(k-1))
elif k <= 10: #Config for 3 to 10 electrons
  # fill the n=2 shells 2s, 2p and any combination of electrons
    between them. Also consider the excitation of 1s electrons.
  Config('g0', '1s2 2*%d'%(k-2),'1s1 2*%d'%(k-1))
elif k <= 18: # 11 to 18 electrons
  Config('g0', '1s2 2*8 3[s,p]%d'%(k-10))
else:
  Config('g0', '1s2 2*8 3[s,p]8 4*%d'%(k-18), '1s2 2*8 3[s,p]8 3d%d
    '%(k-18),'1s2 2*8 3[s,p]8 5*%d'%(k-18),'1s2 2*8 3[s,p]8 6*%d'%(k
    -18))
```

```
23
24 OptimizeRadial('g0') # optimize for the ground levels
25 Structure(pref+'b.en', ['g0']) # calculate the electronic levels
26
27 MemENTable(pref+'b.en') # write to binary file
28 PrintTable(pref+'b.en',pref+'a.en') # write binary to ASCII file
29
30 # calulate transition and save as ASCII
31 TransitionTable(pref+'.tr.b',['g0'],['g0'],0)
32 PrintTable(pref+'.tr.b', pref+'.tr', 1)
33
34
35 ### CRM calculations
36 CETable(pref+'b.ce', ['g0'],['g0'])
37 PrintTable(pref+'b.ce', pref+'.ce')
38
39 AddIon(k, 1.0, pref+'b')
40
41 SetBlocks(-1, pref+'b') # 1: if <0 only transition within 17+ are
      connected, 2: data file (default extension automatically added)
42
43 SetEleDist(1, En, 3, En-10, En+10) #entries: 1) gaussian electron
      energy distribution, 2) electron beam energy in eV, 3) energy
      spread in eV, 4) and 5) Emin and Emax
44 SetTRRates(0)# photon excitation rate coefficients. 0 means: take
      spontaneous decay into acount only.
45 SetCERates(1) # collisional transition rates.1: Calculates, both,
      collisional excitation and de- excitation. 0: only excitation
46
47 SetEleDensity(5e-4) #electron density in units of 1e10 cm^-3
48
49 InitBlocks()
50 SetIteration(1e-6, 0.5, 2048)
51
52 LevelPopulation()
53 SpecTable(pref+'b.sp', 0)
54
55 PrintTable(pref+'b.sp', pref+'.sp')
56
57 t = 0 # transition, e.g., 302 for 3->2 line, 303 for 3->3 line. 0
      includes all lines
58 emin = 1 # eV; emin, emax is the range of allowed transitions
59 emax = 13 # eV
60 eps = 1e-10 # intensity threshold rate
61 PlotSpec(pref+'b.sp', pref+'.pl', k, t, emin, emax, 0.001 ,eps) #
      synthetic spectrum with gaussian lines [eps] width eV
```

```
SelectLines(pref+'b.sp', pref+'.ln', k, 0, emin, emax) # save the
    CRM results
```

B2 Extraction of electronic coefficients for isotope shifts

As described in chapter 5, a way to obtain the electronic constants is to run multiple calculations with different parameters for the MS or the FS and lastly the NP fifth force contribution. The relevant code follows below:

```
import os
from multiprocessing import Pool
import sys
from pfac import fac
from math import sqrt

np = 4 #number of processors to run in parallel
z = int(sys.argv[1]) # Nuclear charge Z
k0 = int(sys.argv[2]) # number of electrons for charge state
k1 = k0

# mediator-mass 'b', logarithmic spacing from 1 to 10^10 eV/c^2
nb = 501 #total number of points
db = 10.0/(nb-1)
bs = [10**(db*i) for i in range(nb)] #mass parameters

# Parameter of field-shift coefficient calculation
rn = fac.NucleusRadius(1.0*z)
rn2 = rn*rn
fr = 2.0 # radius scaling factor
nr = 4 # number of points for field-shift parameter calculation
ib0 = 2+nr

def ploop(i0):
  for i in range(i0,nb+2+nr,np): # split process over processors
    for k in range(k0,k1+1):
      if i == 0: #run without NP force
        c = 'python d.py --z=%d --k=%d --a=0.0 --p=r0
            --nms=3 --sms=3 --r=%g'%(z,k,rn)
      elif i == 1: # run without mass-shift
        c = 'python d.py --z=%d --k=%d --a=0.0 --p=m0
            --nms=0 --sms=0 --r=%g'%(z,k,rn)
      elif i < ib0: # run with different nuclear radii
        ir = i-1
        c = 'python d.py --z=%d --k=%d --a=0.0 --p=r%d
```

```
            --nms=3 --sms=3 --r=%g'%(z,k,ir,sqrt(rn2*(1+ir*fr)))
    else: # run with NP fifth force, force strength set with 'a'
      c = 'python d.py --z=%d --k=%d --a=0.01 --b=%g --p=b%02d
            --nms=3 --sms=3 --r=%g'%(z,k,bs[i-ib0],i-ib0,rn)
    print(c)
    os.system(c) # run the code string
p = Pool(processes=np)
p.map(ploop, range(np))
```

This calls 'd.py', which runs the FAC calculation:

```
from pfac.fac import *
from optparse import OptionParser

ap = OptionParser()
ap.add_option('--z', dest='z', type='int',
              default=20, help='atomic number')
ap.add_option('--k', dest='k', type='int',
              default=4, help='number of electrons')
ap.add_option('--m', dest='m', type='float',
              default=-1.0, help='mass')
ap.add_option('--r', dest='r', type='float',
              default=-1.0, help='radius')
ap.add_option('--a', dest='a', type='float',
              default=0.0, help='yukawa strength')
ap.add_option('--b', dest='b', type='float',
              default=1e5, help='yukawa range in mass unit')
ap.add_option('--p', dest='p', type='string',
              default='', help='output file prefix')
ap.add_option('--nms', dest='nms', type='int',
              default=3, help='NMS option')
ap.add_option('--sms', dest='sms', type='int',
              default=3, help='SMS option')

opts,args = ap.parse_args()

a = ATOMICSYMBOL[opts.z]
SetAtom(a, opts.z, opts.m, opts.r)

pref='%s%02d%s'%(a,opts.k,opts.p)

if abs(opts.a) > 0:
    SetExtraPotential(100, [opts.a, opts.b])

#include normal- and/or special-mass-shift
SetMS(opts.nms, opts.sms) # set points: 3 enable; 0 disable

k = opts.k
```

```
if k == 1:
    Config('g0', '1s1', '2*1')
elif k == 2:
    Config('g0', '1s2', '1s1 2*1')
elif k < 10:
    Config('g0', '1s2 2*%d'%(k-2))
elif k == 10:
    Config('g0', '1s2 2*8', '1s2 2*7 3*1')
elif k <= 14:
    Config('g0', '1s2 2*8 3*%d'%(k-10))
elif k < 18:
    Config('g0', '1s2 2*8 3[s,p]%d'%(k-10),
                 '1s2 2*8 3[s,p]%d 3d1'%(k-11))
elif k == 18: # example on 18 electron system
    Config('g0', '1s2 2*8 3[s,p]8',
                 '1s2 2*8 3[s,p]7 3d1',
                 '1s2 2*8 3[s,p]7 4*1')
else:
    print('config not set')

OptimizeRadial('g0')
Structure(pref+'b.en', ['g0'])

MemENTable(pref+'b.en') # save energy file
PrintTable(pref+'b.en', pref+'a.en')
```

These will then save several files to the hard drive. Their prefixes allow the identification of each, which will be used to obtain the coefficients:

```
from pfac.rfac import *
from pfac import fac
import numpy as np
from scipy import optimize

# calcium (z=20) transitions of interest for 16+ to 11+ and 1+
zs =  [20,20,20,20,20,20,20,20,20,20] # nuclear charge
ks =  [4 ,5 ,6 ,6 ,8 ,9 ,19,19,19,19] # electrons left in atom
i0s = [2 ,0 ,0 ,1 ,0 ,0 ,1 ,2 ,0 ,0 ] # index lower energy level
i1s = [3 ,1 ,1 ,2 ,1 ,1 ,3 ,4 ,1 ,2 ] # index upper energy level
fr = 2.0

res=open('coefficient_results.txt','w') # save results in a single
    file
res.write('#z\tk\ti0\ti1\tbs[i]\tde\n')
for ik in range(len(ks)):
  z = zs[ik] # nuclear charge
  a = fac.ATOMICSYMBOL[z]
  k = ks[ik] # electrons left in atom
```

```
  i0 = i0s[ik] # index of upper level index
  i1 = i1s[ik] # index of lower level index
  p = '%s%02d'%(a,k) # prefix
  r0 = FLEV(p+'r0a.en') # load levels with SM but no NP shifts
  m0 = FLEV(p+'m0a.en') # load levels without MS
  rs = np.zeros(5)
  re = np.zeros(5)
  rs[0] = fac.NucleusRadius(z*1.0)
  re[0] = (r0.e[i1]-r0.e[i0])
  rn = rs[0]
  rn2 = rn*rn
  for i in range(4):
    ir = i+1
    r1 = FLEV(p+'r%da.en'%ir) # load levels with different radii
    rs[ir] = rn2*(1+ir*fr)
    rs[ir] = rs[ir].sqrt()
    re[ir] = r1.e[i1]-r1.e[i0] # transition of different radii
  #calculate the MS K coefficient 'de0' by subtracting FS-only (m0)
    from all SM parts (r0):
  de0 = ((r0.e[i1]-r0.e[i0])-(m0.e[i1]-m0.e[i0]))*fac.ATOMICMASS[z]
  ar = np.zeros((5,2))
  ar[:,0] = 1.0
  for i in range(len(ar[:,1])):
    ar[i,1] = rs[i]*rs[i] # radius squared
  x = optimize.lsq_linear(ar, re) # run a fit through the data
  de1 = x.x[1] # slope of fit is the FS F coefficient 'de1'
  print( '%2d %2d %d %d'%(z,k,i0,i1) )
  # save the total energy, and MS and FS coefficient:
  res.write('%2d\t%2d\t%d\t%d\t%15.8E\t%15.18E\n'
            %(z,k,i0,i1,0.0,(m0.e[i1]-m0.e[i0])-de1*(rn*rn)) )
  res.write('%2d\t%2d\t%d\t%d\t%15.8E\t%15.18E\n'
            %(z,k,i0,i1,0.0,de0) )
  res.write('%2d\t%2d\t%d\t%d\t%15.8E\t%15.18E\n'
            %(z,k,i0,i1,0.0,de1) )

  nb = 501 # number of mediator masses
  db = 10.0/(nb-1)
  bs = [10**(db*i) for i in range(nb)]
  for i in range(nb):
    f = p+'b%02da.en'%i
    r = FLEV(f) # load levels with different NP mediator masses
    # subtract SM shifts (r0) from the NP calculation (r), counter
   the force strength a=0.01 by multiplying by 100 and devide by
   the number of neutrons:
    de = 100.0*( (r.e[i1]-r.e[i0])-(r0.e[i1]-r0.e[i0]) )
         /(fac.ATOMICMASS[z]-z)
    res.write('%2d\t%2d\t%d\t%d\t%15.8E\t%15.18E\n'
```

```
63                 %(z,k,i0,i1,bs[i],de) ) # save the extracted NP X
64 res.close()
```

Using this saved file `coefficient_results.txt`, the shift coefficients can be used to accurately calculate IS and the KPs without being limited by the FAC numerical precision. Precision of the extracted NP coefficient X may be improved by increasing the strength parameter a in the calculation. However, an NP shift of too big proportions would lead to a mixing of levels, which would cause other problems. Furthermore, even a smaller NP shift may cause a change in the energy level indexing in FAC, thus requiring additional code to track the levels of interest. This could be done, for example, by tracking the configuration name in the energy level file of FAC.

Appendix C

FAC: Acquisition of LS-notation

One issue with FAC is that the results do not include g-factor, nor a LS-notation for the levels. The latter can be resolved with the help of GRASP2K's module `jj2lsj`, which generates the LS-notation for each level and its percentage of level mixing. To achieve this, the following command needs to be added after `Structure` command:

```
BasisTable(pref,10)
```

with `pref` being the filename and `10` the setting to write GRASP2K-compatible files `pref\_*.c` and `pref\_*.cm`, which are the basis wavefunctions and mixing coefficients from FAC.

C1 Bug fixes

However, to make this work, several bug fixes need to be added to a few of GRAPS2K's subroutines.

1, jj2lsj_code.f90, asf2ls subroutine, from https://github.com/flexible-atomic-code/fac/blob/master/doc/misc/jj2ls.md:

```
wb = zero
do LS_number = 1, asf_set_LS%csf_set_LS%nocsf
   if ((asf_set_LS%csf_set_LS%csf(LS_number)%parity == "+" &
      .and.  ISPAR(iw1+NCFMIN-1) == 1)  .or.
    &
      (asf_set_LS%csf_set_LS%csf(LS_number)%parity  == "-" &
      .and.  ISPAR(iw1+NCFMIN-1) == -1)) then
```

2, jj2lsj_code.f90, etLS_job_count() subroutine, from https://github.com/flexible-atomic-code/fac/blob/master/doc/misc/jj2ls.md:

```
if(all_occupation(isubc).eq.0) then
   if(isubc.gt.1) then
      Li(isubc)  = 0;          L_i(isubc) = L_i(isubc-1)
      Si(isubc)  = 0;          S_i(isubc) = S_i(isubc-1)
```

```
   else
      Li(isubc)  = 0;          L_i(isubc) = 0
      Si(isubc)  = 0;          S_i(isubc) = 0
   endif
   if(isubc .lt. asf_set_LS%csf_set_LS%nwshells) then
      call setLS_job_count(isubc + 1, rez)
   else
      if(ittk(S_i(isubc),L_i(isubc),J).eq.1)          &
           call setLS_action(action_type, rez) !rez=rez+1
   end if
else
```

3, jj2lsj_code.f90, packlsCSF subroutine:

```
integer dimension(40) :: Q
character(len=3), dimension(79) :: COUPLE
character(len=3), dimension(40) :: ELC
character(len=164), INTEND(OUT) :: string_CSF
IF(counter>40) THEN
write(57,'(1X,I3,1X,A4,5X,A1,8X,F16.9,5X,F7.3,A164)')
write(57,'(7X,F12.8,3X,F11.8,3X,A164)')
write(58,'(I6,F16.9,2X,A164)')
```

4. jj2lsj_code.f90, jj2lsj subroutine:

```
character(len=164), dimension(1:Vector_number) :: string_CSF
character(len=164) :: string_CSF_ONE
```

5. packLS.f90, PACKLS subroutine:

```
character(len=164), INTEND(OUT) :: STR
```

C2 Running GRASP

After this is implemented, GRASP2K should be compiled as usual. To finally run it, type in the prompt

```
jj2lsj
pref_000
```

followed by two 'y' to start the conversion. This creates new files with the name `pref_000.lsj.lbl`, which look like the below (shortened to fit the page):

```
 Pos    J    Parity       Energy Total       Comp. of ASF
    5   1/2      +         -13317.508997086      100.000%
          0.80447931     0.64718696        1s(2).2s(2).2p(6).3s(2).3p
   (6).3d(3)4P3_4P
         -0.59398067     0.35281304        1s(2).2s(2).2p(6).3s(2).3p
   (6).3d(3)2P3_2P
   10   1/2      +         -13316.894530031      100.000%
```

```
6          0.80447931    0.64718696        1s(2).2s(2).2p(6).3s(2).3p
   (6).3d(3)2P3_2P
7          0.59398067    0.35281304        1s(2).2s(2).2p(6).3s(2).3p
   (6).3d(3)4P3_4P
8
9     0  3/2     +         -13318.048952326      100.000%
10         -0.82234187    0.67624616        1s(2).2s(2).2p(6).3s(2).3p
   (6).3d(3)4F3_4F
11         -0.38421856    0.14762390        1s(2).2s(2).2p(6).3s(2).3p
   (6).3d(3)2D3_2D
12         0.32405466    0.10501142        1s(2).2s(2).2p(6).3s(2).3p
   (6).3d(3)2D1_2D
13         0.22439609    0.05035361        1s(2).2s(2).2p(6).3s(2).3p
   (6).3d(3)2P3_2P
14         -0.14410035    0.02076491        1s(2).2s(2).2p(6).3s(2).3p
   (6).3d(3)4P3_4P
15    3  3/2     +         -13317.431248056      100.000%
16         0.65040196    0.42302271        1s(2).2s(2).2p(6).3s(2).3p
   (6).3d(3)4P3_4P
17         -0.57097370    0.32601096        1s(2).2s(2).2p(6).3s(2).3p
   (6).3d(3)2P3_2P
18         -0.42844991    0.18356932        1s(2).2s(2).2p(6).3s(2).3p
   (6).3d(3)4F3_4F
19         0.19940692    0.03976312        1s(2).2s(2).2p(6).3s(2).3p
   (6).3d(3)2D3_2D
20         -0.16623443    0.02763388        1s(2).2s(2).2p(6).3s(2).3p
   (6).3d(3)2D1_2D
```

Here, the `Pos` is the index of the level from FAC `.en`-file, which is followed by the total angular momentum J, Parity, Energy and Composition. The next line will contain the parity mixing and the energy level mixing, where a 1 is 100%. After that, the LS-notation of that energy-level is displayed in order of filling and the total angular momentum until this point is displayed in parentheses. The key information lies behind the '_' where the S and L of the level is displayed. From this information not only the strength of the level mixing can be seen, but the LS-notation yields an estimation for the g-factor from the Dirac formula of the g-factor.

Appendix D

AMBiT: Xenon calculations

Another way to calculate the energy levels and their transition rates is via AMBiT [85]. Its input file is relatively short and does not require the definition of any particular configurations. If done correctly, AMBiT can result in much more precise ab-intio results. An input file can now look like this:

```
ID = XeXVII

Z = 54

-s123

[Lattice]
NumPoints = 1000
StartPoint = 1.0e-6
EndPoint = 20.0

[HF]
--breit
N = 38
Configuration = '1s2 2s2 2p6 3s2 3p6 3d10 4s2 4p6: 4d0.8 4d+1.2'

[Basis]
--bspline-basis
BSpline/N=40
BSpline/K=9
ValenceBasis = 8spdf

[CI]
LeadingConfigurations = '4d2'
ElectronExcitations = 2
EvenParityTwoJ = '0,2,4, 6,8,10,12'
// OddParityTwoJ = '0, 2, 4, 6, 8, 10, 12'
NumSolutions = 4
```

```
29
30 [MBPT]
31 Basis = 30spdfgh
32
33 [Transitions]
34 M1/AllBelow = -0.5
35 E2/AllBelow = -0.5
```

In this configuration, note the relativistic nomenclature `4d0.8 4d+1.2`, where the degeneracy of the d-shell is 4:6, thus splitting the 2 electrons into 0.8:1.2, i.e. moving the 4d+ electrons back into the core. The `NumSolutions` refer to how many levels should be included per configuration, which should be equal to the highest number of levels per total angular momentum in the ground configuration.

Finally, the transitions can be calculated, where -0.5 refers to atomic units. The results in the output file will indicate the indices as `2e` or `1o` for $J = 1$ of even-, or $J = 0.5$ of odd-parity levels. Then the M1 and E2 transitions are separated and given as line strength. Such can be recalculated to A_{ki} values with Eq. 2.13 through Eq. 2.15.